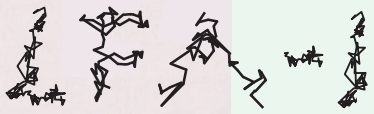

dynamics

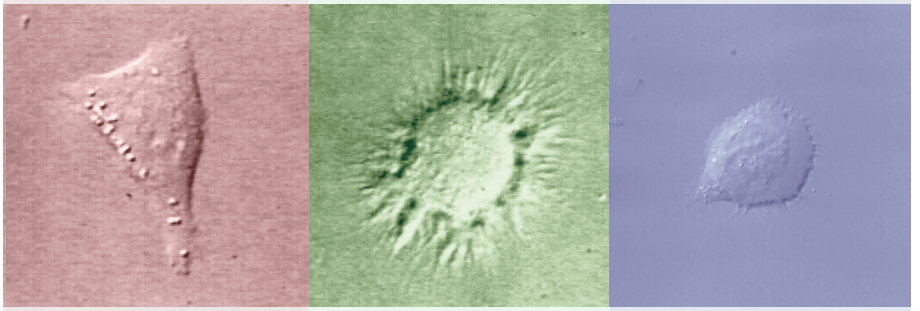

on the membrane of leukocytes

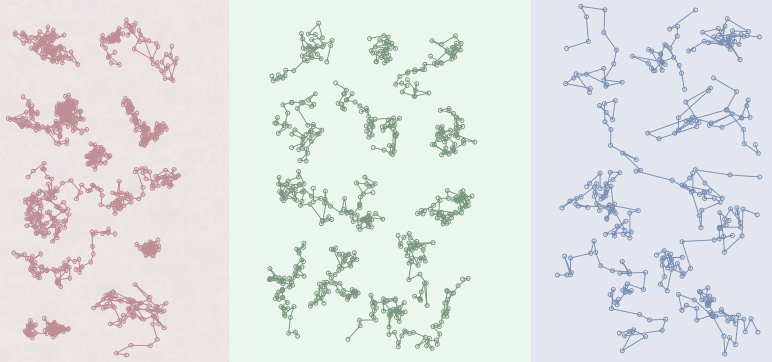

A single dye tracing study

Gert-Jan Bakker

LFA-1 DYNAMICS ON THE MEMBRANE OF LEUKOCYTES: A SINGLE DYE TRACING STUDY

G.J. Bakker

Thesis committee members:

Prof. dr.	G. van der Steenhoven	University of Twente (chairman)
Prof. dr.	M.F. García-Parajó	IBEC, Barcelona, Spain (promotor)
Prof. dr.	N.F. van Hulst	University of Twente (promotor)
Dr.	A. Cambi	Radboud University (assistant promotor)
Prof. dr.	G.J. Schuetz	Johannes Kepler Universität Linz, Austria
Prof. dr.	W. Kolanus	University of Bonn, Germany
Prof. dr.	J. Herek	University of Twente
Prof. dr.	V. Subramaniam	University of Twente

This work is part of the research programme of the 'Stichting voor Fundamenteel Onderzoek der Materie (FOM)', which is financially supported by the 'Nederlandse Organisatie voor Wetenschappelijk Onderzoek (NWO)'.

The research described in this thesis was carried out at the BioNanophotonics group, IBEC-Institute for Bioengineering of Catalonia and CIBER-bbn, Baldiri Reixac 15-21, 08028 Barcelona, Spain and at the Optical Sciences group, MESA$^+$ Institute for Nanotechnology and Faculty of Science and Technology, University of Twente. P.O. Box 217, 7500 AE Enschede, The Netherlands.

G.J. Bakker
LFA-1 dynamics on the membrane of leukocytes: a single dye tracing study
Ph.D. Thesis, University of Twente, Enschede, The Netherlands.

ISBN 978-90-365-3209-9
doi: 10.3990/1.9789036532099

This thesis can be downloaded from http://dx.doi.org/10.3990/1.9789036532099
Author's email: g.bakker@ncmls.ru.nl

LFA-1 DYNAMICS ON THE MEMBRANE OF LEUKOCYTES: A SINGLE DYE TRACING STUDY

PROEFSCHRIFT

ter verkrijging van
de graad van doctor aan de Universiteit Twente,
op gezag van de rector magnificus,
prof.dr. H. Brinksma,
volgens besluit van het College voor Promoties
in het openbaar te verdedigen
op vrijdag 8 juli 2011 om 12.45 uur

door

Gerrit Jan Bakker
geboren op 16 juni 1976
te Alkmaar

This dissertation has been approved by:

prof. dr. M.F. García-Parajó (promotor)
prof. dr. N.F. van Hulst (promotor)
dr. A. Cambi (assistant promotor)

"Ha, ha, it's just for the fun of science!"

— A scientist from Denmark (1999).

Table of Contents

1 Introduction **1**

1.1 LFA-1 in the immune system 2
1.2 LFA-1 mediated adhesion regulation 3
1.3 Spatio-temporal regulation of LFA-1 on the plasma membrane 5
1.4 Single molecule detection techniques for biological studies . . . 7
1.5 Probing dynamics within a single cell 8
1.6 Single Particle Tracking 8
1.7 Single Dye Tracing 9
1.8 Automated single particle tracking 11
1.9 Analysis of trajectories 11
1.10 Aim of this thesis 13
1.11 Thesis overview 14

2 Tracing Nanoclusters on Living Cells **17**

2.1 Introduction 18
2.2 Materials and Methods 19
2.2.1 Sample preparation 19
2.2.2 High-speed dual color EPI-TIRF microscopy with single molecule detection sensitivity 20
2.2.3 Single nanocluster tracing on living cells 24
2.2.4 Data Analysis 25
2.3 Results 26
2.3.1 Characterization of intensifier gain 26
2.3.2 General setup performance 27
2.3.3 Dual-color performance 29
2.3.4 Accuracy 30
2.3.5 Imaging and tracing individual fluorescent nanoclusters 34
2.3.6 Analysis of nanocluster trajectories 34
2.4 Discussion 39
2.5 Conclusion 40

3 LFA-1 Nanocluster Mobility on THP-1 Monocytes **41**
3.1 Introduction . . . 42
3.2 Materials and Methods . . . 43
3.3 Results . . . 48
3.3.1 Optimization of direct antibody labeling on monocytes. 48
3.3.2 Single Dye Tracing of individual LFA-1 nanoclusters . . 49
3.3.3 Effect of the substrate on the mobility of LFA-1 nanoclusters . . . 49
3.3.4 LFA-1 nanoclusters are primarily mobile on resting monocytes . . . 51
3.3.5 Extended LFA-1 reveals a distinctive diffusion profile . . 53
3.3.6 A fraction of the extended LFA-1 nanoclusters is anchored to the actin cytoskeleton . . . 56
3.3.7 Transient confinement in L16 epitope subpopulation. . . 57
3.3.8 ICAM-1 functionalized surfaces alter LFA-1 mobility on ventral and dorsal side of the cell membrane. . . . 59
3.3.9 Induced microclustering of LFA-1 slows down its lateral mobility on the membrane . . . 61
3.4 Discussion . . . 63
3.5 Conclusion . . . 69

4 Extracellular Ca^{2+} Links Integrin Nanocluster Conformation to Mobility **71**
4.1 Introduction . . . 72
4.2 Materials and Methods . . . 73
4.3 Results . . . 76
4.3.1 Expression of L16 and TS2/4 epitopes at different Ca^{2+} conditions . . . 76
4.3.2 Effect of extracellular Mg^{2+} on LFA-1 mobility . . . 77
4.3.3 LFA-1 mobility decreases dramatically upon reduction of extracellular Ca^{2+} . . . 79
4.3.4 LFA-1 binds to the actin cytoskeleton upon reduction of extracellular Ca^{2+} levels . . . 82
4.3.5 Extracellular Ca^{2+} enhances cell binding under low, but not under high shear flow conditions. . . . 84
4.4 Discussion . . . 87
4.5 Conclusion . . . 91

5 Comparison of Lateral Mobility and Spatial Organization of LFA-1 **93**
5.1 Introduction . . . 94
5.2 Materials and Methods . . . 95
5.3 Results . . . 97

5.3.1 LFA-1 trajectories on monocytes, imDC and T cells. . . 97
5.3.2 LFA-1 mobility as a function of DC maturation. 98
5.3.3 Diffusion constants of LFA-1 on imDCs increased twofold compared to monocytes. 100
5.3.4 Immature DCs show three LFA-1 mobility subpopulations 100
5.3.5 The diffusion constant of LFA-1 on imDCs is reduced compared to T cells 104
5.4 Discussion 105
5.5 Conclusions 110

6 General Discussion and Future Prospectives 111
6.1 Observation and analysis of protein mobility of membrane biomolecules 112
6.2 LFA-1 mobility on leukocytes 114
6.3 Extracellular Ca^{2+} links integrin nanocluster conformation to mobility 115
6.4 The relation between mobility, micro environment and spatial organization of LFA-1 117

Bibliography 118

Summary 137

Samenvatting 141

Acknowledgement / Dankwoord 145

Chapter 1

Introduction

Leukocytes have the ability to rapidly switch their adhesion in response to the cell's physiological environment. How these cells modulate their adhesiveness during the different stages of their life cycle, has been a central question in immunology. Adhesion regulation has its origin at the molecular scale, where processes are dynamic, heterogenous and tightly orchestrated. To unravel these unanswered questions it is therefore of utter importance to probe biological processes in a time-dependent manner on a molecular scale. With the development of Single Particle Tracking and ultimately Single Dye Tracing, it is now possible to follow the mobility of individual biomolecules on the plasma membrane of living cells. Observation of mobility of individual biomolecules does not only provide information about the local microenvironment of the probed biomolecules, but it also gives complementary insight into the processes at work at the nanolevel. The aim of this research has been to investigate the lateral mobility of one of the most important receptors involved in cell adhesion in the immune system: the integrin receptor LFA-1. By using single molecule techniques we have been able to deepen our understanding of LFA-1 mobility and its consequences for LFA-1 affinity and avidity regulation on THP-1 monocytes (monocytes) and immature dendritic cells (imDCs).

1.1 LFA-1 in the immune system

Leukocytes or white blood cells are highly specialized bone marrow derived cells, which play a pivoting role in the immune system of our body [1]. They can patrol through our body and are able to encounter, recognize and respond to pathogenic or foreign material like viruses, bacteria and cancerous cells. Besides interaction with pathogenic material, they interact with each other in order to pass information to initiate an immune response. These multiple tasks can have contradictive demands and leukocytes developed multiple strategies to cope with this situation. First, leukocytes developed into different groups of highly specialized cells, fulfilling specific tasks in the innate and/or adaptive immune system. Second, leukocytes like dendritic cells (DCs) are able to adapt to different stages in their life cycle by means of environment triggered differentiation. Furthermore, a specialized set of membrane proteins give leukocytes the ability to rapidly adapt to different tasks. One of the most abundant and very intriguing protein families is those of leukocyte specific integrins.

Integrins are receptors that support the cell's ability to adhere and migrate, by binding to specific extracellular matrix (ECM), cell-surface or soluble ligands. Like our hands and feet, integrins are very well articulated: they have the unique ability to modulate dynamically their adhesiveness through both affinity- and valency-based mechanisms [2, 3]. They are also able to transduce signals by means of ligand binding, interaction with cations [4] or transduction of applied forces [5] and thereby define cellular shape, mobility, and regulate cell cycle. Integrins form a superfamily of heterodimeric transmembrane proteins, consisting of an α and a β subunit. On humans, 18 α and 8 β subunits have been identified, forming 24 possible combinations, see figure 1.1. Integrins in the leukocyte specific subset are recognizable by the $\beta 2$ and the $\beta 7$ subunits [6]. They play critical roles for the immune system in leukocyte trafficking and migration, immunological synapse (IS) formation, costimulation, and phagocytosis. The $\beta 2$ integrin family counts four members, all recognizing one or more members of the intercellular adhesion molecule (ICAM) family [7].

Among these four members, lymphocyte function-associated antigen 1 (LFA-1; $\alpha L \beta 2$; CD11a/CD18) is the most abundant and widespread in expression. LFA-1 binds to its ligand ICAM-1 (CD54), and to less extend to ICAM-2 and ICAM-3 (CD102 and CD50) [8]. During the process of extravasation of lymphocytes LFA-1 supports rolling, plays a pivoting role in arrest and is necessary for crawling and transendothelial migration [9–11]. On monocytes, LFA-1 plays a similar role [12, 13]. Upon differentiation of monocytes towards immature DCs [14], LFA-1 functionality is downregulated [3], although recent findings suggest that LFA-1 does play a role during certain stages of the DC life cycle [15–18]. In addition, LFA-1 on lymphocytes acts as a co-receptor by binding to ICAM-1 on mature DCs during the immunological synapse [19, 3]. Finally,

LFA-1 engagement enhances transcriptional activation of numerous genes, involved in the control of cell differentiation and proliferation [20]. Absence or malfunctioning of $\beta 2$ molecules in the immune system leads to severe impairment of fundamental parts of the immune system, as has been verified by study of the natural occurring disease leukocyte adhesion deficiency-I (LAD-I) [21].

1.2 LFA-1 mediated adhesion regulation

On the onset of migration, stimulated leukocytes 'switch' from a non-adhesive to an adhesive state within seconds, inducing a transition from rolling to arrest on endothelial vascular cells at the site of inflammation. On the other hand, the stable bonds formed between antigen presenting cells and T or B cells can take more than an hour. Due to the variety of leukocyte specific adhesion mechanisms, in vitro and in vivo models and experimental techniques, LFA-1 mediated adhesion has been studied from many different perspectives for many years. So far, three not-mutually-exclusive mechanisms have been proposed for LFA-1 adhesion regulation. First, in the affinity based model individual LFA-1 molecules can undergo conformational changes, leading to modulation of affinity for its ligand [22–25, 4]. Each individual integrin in the pool of integrins on

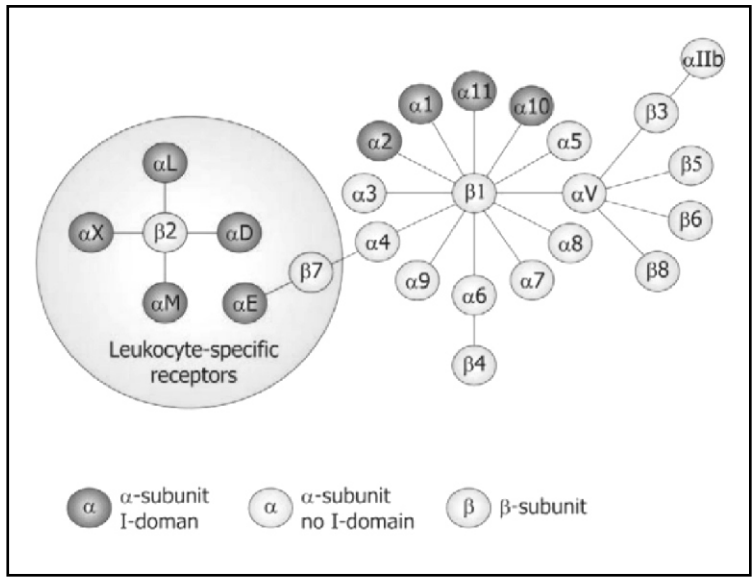

Figure 1.1. *The human integrin superfamily. Figure modified from Hynes, 2002 [6].*

the membrane, has a probability to be in a specific conformational state. These conformational state related probabilities can be modulated upon interaction with cations and integrin specific intra- or extracellular proteins, ultimately leading to modulation of the overall LFA-1 mediated binding strength.

Second, in the valency based model, adhesion is modulated by alteration of the number of bonds that can form at the contact site. The alteration of the number of bonds can happen as a secondary process when mobilized integrins in a high-affinity state gather at the binding site in a mass driven manner [26–29]. In this case, LFA-1 molecules form large micrometer-sized clusters. Alternatively, valency can manifest itself as an independent adhesion regulation mechanism [30, 31, 3].

Third, in the mobility based model, adhesion is regulated by the ability of the molecules to diffuse around on the cell membrane. Increasing integrin mobility will lead to an enhanced integrin-ligand encounter probability [32, 33]. Furthermore, it has been proposed that release of LFA-1 from cytoskeletal constraints and thereby enhancing its mobility is an important early step in adhesion activation [34]. In this scenario, all proposed adhesion regulation mechanisms can be coupled, since release from cytoskeletal restraints can be the onset of mass-driven recruitment of receptors, depending on the affinity state of the mobile LFA-1 molecules. Evidence is building up that affinity, valency and mobility based adhesion regulation mechanisms are interrelated and tightly orchestrated [35, 3, 28]. Indeed, a new model for adhesion regulation on T-cells has been proposed, where different cytoskeletal regulators recognize different conformational states of LFA-1, thereby coupling LFA-1 conformations (affinity) to LFA-1 mobility (mobile or immobile) and induced micrometer-sized clustering [28]. Affinity, valency and mobility might also be interrelated by association of LFA-1 to lipid rafts. A study on T-lymphocytes demonstrated that active LFA-1 was associated to lipid rafts, while inactive LFA-1 was excluded from lipid rafts by cytoskeletal constraints [36].

Mutagenesis studies [37–40, 26, 41], the use of conformation-specific monoclonal antibodies [24, 42, 43, 4], blocking peptides [44, 45], crystallography [22, 46, 47] and other protein structure studies like high-resolution EM (electron microscopy) [48] and NMR (nuclear magnetic resonance) [49] have underlined the relationship between conformational changes and affinity and have elucidated the mechanisms behind it on a sub-molecular level, leading to a long list of integrin affinity states [48, 39, 24, 50, 11, 4, 44]. Nevertheless, under physiological conditions there is generally spoken of three distinctive stable LFA-1 conformations, namely the bent, extended closed headpiece and extended open headpiece conformation (fig. 1.2). They respectively have a low, intermediate and high affinity for their ligand. LFA-1 contains two non-covalently associated, type I transmembrane (TM) glycoprotein α and β subunits with large extracellular domains, single spanning TM domains and short cytoplasmatic

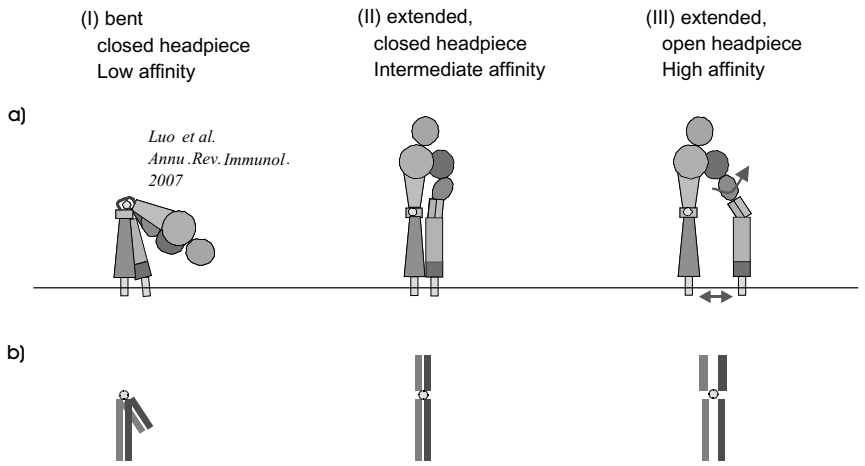

Figure 1.2. *Interpretation of LFA-1 in different molecular conformations. a)I: bent, low affinity; II: extended closed headpiece, intermediate affinity; III: extended open headpiece, high affinity. Notice separation between cytoplasmic tails. b) Simplified cartoons of LFA-1 conformational states.*

domains [51]. LFA-1 converts from the bent (I) to the extended (II) conformation by making a 'switchblade'-like motion [48]. Upon such a conformational rearrangement, both the LFA-1 affinity for its ligand and its TM domain separation increase. The highest affinity and TM domain separation can be found in the extended open headpiece conformation (III). The link between affinity and TM domain separation forms the basis of the bi-directional signalling properties of LFA-1 [52, 25, 37, 38].

1.3 Spatio-temporal regulation of LFA-1 on the plasma membrane

The bi-lipid cell membrane forms a barrier between the cell and its environment. Tight cooperation between intra- and extracellular environments is a necessary prerequisite of life and therefore the cell membrane is highly functional: cations, signals, molecules and forces cross the barrier. In addition, the outer cell membrane forms a scaffold for many biological processes. In the early 70's, the fluid mosaic model helped us on our way of understanding this multi-functional structure [53], though nowadays it is well known that the plasma membrane is highly organized and dynamic. Proteins and lipids are

spatially and temporally confined in nanometric-scale areas of the cell membrane [54, 55]. Until now, the cytoskeleton [56], lipid rafts [57, 58, 54], caveolae [59], tetraspanins [60], proteoglycans [61] and protein-protein interactions [62] have been identified as players in membrane organization.

High resolution microscopy techniques give a direct evidence for membrane organization at the nanolevel and support a highly dynamic picture of the cell membrane [63]. Though, a direct evidence for the existence of the spatial *and* temporal compartmentalized membrane is given by recently developed single molecule techniques [64–66]. Evidence for raft as well as actin meshwork based compartmentalization of the membrane was found by the groups of D. Marguet, K. Jacobson and Akihiro Kusumi using mainly SPT and FCS [67, 68, 65]. These and other recent single particle tracking/single dye tracing studies pinpoint the transient character of protein association with lipid rafts and other types of domains, having a direct impact on the biological function of these molecules [69, 70]. Besides providing a readout of transient interactions between biomolecules, spatio-temporal study of protein or lipid organization also gives information about the local micro-environment of these biomolecules. Many studies have attempted to unravel the mechanisms behind observed diffusion and tried to relate these to biological functionality [71–76].

LFA-1 is also organized and regulated at the nanoscale on the cell membrane, as has been observed with high resolution microscopy techniques [3, 77]. The functional role of found integrin micro- and nanodomain organization on the plasma membrane is still under investigation. Since the early days, the actin cytoskeleton has been known to play a role in regulation of integrin organization on the membrane [78, 34, 40]. Association of integrins to the actin cytoskeleton has been proposed as a docking mechanism during the immunological synapse [79, 3] and release of integrins has been proposed as a mechanism for redistribution by mass-driven transport to binding sites [27]. Furthermore, transient confinement by (transmembrane proteins attached to) the actin meshwork underneath the membrane [56] might help to bring integrins and specific nanoscale rafts together, to form so-called functional 'hotspots' on the cell membrane [77].

According to literature, the role of lipid rafts in regulation of integrin mediated adhesion is threefold: first, it is proposed that lipid rafts recruit signalling molecules together, enhancing signal transduction [58, 80, 81, 77] and possibly regulate integrin valency [82, 36, 83]. Second, lipid rafts play a role in vesicle mediated transport of integrins during leukocyte chemotaxis [84, 85]. Third, rafts might play a role in integrin tethering to the cytoskeleton. Indeed, it was observed that co-clustering of raft associated proteins coincided with actin polymerization [86, 87]. Furthermore, localization studies and density-gradient flotation experiments indicated that the possibly LFA-1 related tetraspanin CD82 localizes in raft microdomains linked to the actin cytoskeleton [88].

In summary, LFA-1 function on leukocytes is highly dynamic and versatile. Cells have the ability to rapidly adapt LFA-1 mediated adhesion strategies by modulation of the molecule's conformation and its spatial organization on the cell membrane. Leukocyte adhesion is tightly regulated at the nanometric scale and therefore high-resolution microscopy techniques play an important role in the investigation of the spatial distribution of LFA-1 and its interacting molecules. In the next section, optical microscopy techniques specially tailored to visualize membrane biomolecule organization and dynamics at high spatial and/or temporal resolution will be reviewed.

1.4 Single molecule detection techniques for biological studies

Biological processes have their origin at the molecular scale, where they are tightly orchestrated to keep cellular processes in balance with each other. Due to the heterogeneous and dynamic character of life at the single molecule level, many biological questions remain unanswered despite the extensive repertoire of molecular biology tools and standard microscopy techniques nowadays available [89–91]. To gain information at the molecular scale it is therefore utterly important to probe biological processes in a time-dependent manner at this scale.

The first single biomolecule sensitive equipment developed already 3 decades ago was the patch clamp technique, elucidating the behavior of a single ion channel [92]. In the 90's, fluorescence microscopy was taken to the single molecule detection sensitivity limit [93–95] and soon afterwards this new approach became feasible for biological applications [96]. The imaging of single quantum systems opened a wealth of new possibilities, like probing single molecule orientation [97, 98], single pair FRET (Förster Resonance Energy Transfer,) [99, 100], single molecule sensitive fluorescence lifetime imaging [93], stoichiometry of multimers [101, 102] and the use of quenching to probe proximity effects in the order of a few nm's [103]. To suppress background levels and to increase signal to noise ratio, TIRFM (Total Internal Reflection Fluorescence Microscopy) was combined with single molecule sensitivity to investigate the immediate vicinity of the cell membrane [104].

Single molecule detection sensitivity made it possible to localize individual fluorescent molecules with nanometer precision [105, 106], although the actual resolution was still limited by the wavelength of light to approximately $1.22\lambda/2NA$. The diffraction limit was first broken by NSOM (Near-field Scanning Optical Microscopy), making possible to map labeled biomolecules on a cell membrane with 100nm resolution [107]. Recently, by the use of small optical antennas, the evanescent field at the tip aperture edges could be locally

enhanced leading to resolutions of 20nm [108]. Novel techniques like STED (stimulated emission depletion) have been also developed to provide resolution to 20nm while maintaining single molecule detection sensitivity for a limited set of fluorescent probes [109, 110]. However, since both of these high resolution techniques are hard to implement and laborious on a routine basis, the search for alternative high resolution imaging techniques continued. Recently, two easy implementable "high resolution" techniques called (F)PALM (photo-activated localization microscopy) and STORM (stochastic optical reconstruction microscopy) have been developed [111–115], based on the use of photo-activatable fluorescent proteins or dyes [116]. Thus, in order to obtain nanometer optical resolution, scanning techniques and photo switchable dyes have been applied at the expense of imaging speed, which is currently the limiting factors in super resolution live imaging [117]. Alternative techniques are required to probe dynamic processes at the cellular and molecular level with high spatial precision.

1.5 Probing dynamics within a single cell

To probe dynamics of proteins on cells in the millisecond timescale, techniques have been developed to probe the diffusion behavior of proteins on living cells. FRAP (Fluorescence Recovery After Photobleaching) has been widely used by biologists for more than three decades to reveal diffusion of proteins in the cell membrane being able to separate and quantify mobile and immobile fractions [118]. However, highly heterogeneous mobility behavior and low densities of membrane proteins remained difficult to access due to averaging and limited spatial resolution of the technique [119, 120, 96]. FCS (Fluorescence Correlation Spectroscopy) based techniques can probe dynamics of and interactions between single (bio) molecule ensembles at a very wide dynamic range, ranging from processes like antibunching in the nanosecond range to diffusion processes in the second range [121]. FCS has been able to discriminate and characterize many types of mobility behavior. Recently a FCS method has been developed to detect and characterize transient confinement on the cell membrane [66]. Yet, FCS is not the preferred technique for probing mobility of relatively slow diffusing probes distributed at low densities. If in addition diffusion behavior is spatially heterogeneous, FCS becomes impractical since multiple areas should be measured per cell within a limited time.

1.6 Single Particle Tracking

In the early 80's SPT (Single Particle Tracking) was introduced [122]. SPT utilizes time lapse microscopy to monitor the dynamics of individual biomolecules

or clusters by labeling them with particles which can be imaged with high accuracy and specificity. Particles (Colloidal gold and μm-sized polystyrene beads) are usually tracked by contrast enhanced transmission microscopy [57, 123], but in some cases fluorescence microscopy has been applied [124, 120]. Also quantum dots have been applied successfully as probes for SPT [125, 126]. By exploiting the temperature dependent absorption properties of gold it became possible to track slowly moving membrane proteins connected to colloidal gold particles of sizes below 10nm [127]. High precision three-dimensional tracking became possible by using the feedback signal of an optical trap or a laser scanning system that followed a single bead [128–130].

SPT-based techniques are generally not limited by photobleaching of the particles and therefore have the ability to probe biomolecules with high temporal resolution (frame rates up to 40kHz [68]) and excellent localization accuracy in space (1-10nm). Due to these characteristics different modes of motion could be distinguished (directed, superdiffusive, normal, anomalous, corralled, and 'fixed' motion [119, 123, 131, 132]) and compartmentalization of the cell membrane could be studied [133, 134]. The most important cons of SPT are related to the probes used for tracking biomolecules. The labeled probes are relatively large compared to tracked tracked biomolecules. Crosslinking of biomolecules by (a-)specific binding to probes can cause serious artifacts, due to secondary effects like triggering of cellular processes and increased hindering of diffusion by the complex microstructure of biological membranes [135].

1.7 Single Dye Tracing

With the introduction of Single Dye Tracing (SDT) [136], the major drawbacks regarding the particle size in SPT have been solved. SDT follows the same principle as SPT, but instead of single particles, single fluorescent molecules are being used as a probe for biomolecules. Besides the size of the probe, SDT has several other advantages over SPT: first, individual autofluorescent proteins can be monitored by SDT and thus fluorescent labeling can be transfected in the cell's genome, providing tracking within living systems with the hope of least interference with the biological function and vitality of the cell. [137]. Second, by reaching single molecule detection sensitivity, SDT opened the door to a vast amount of new possibilities. Simultaneous tracking of position, dye emission and orientation [98, 138], determination of colocalization by position [139, 140, 138] and FRET [100] without steric hinderance, determination of stoichiometry of protein complexes [102], simultaneous imaging and spectroscopy of single molecules [141] and environment dependent activation of probes [142, 143] have been demonstrated. SDT has also been applied for three-dimensional (3D) tracking of probes in the nucleus and cytosol of individual cells [144–146].

SDT took off in 1996, when a methodology for visualization of motion of

individual molecules was published [147]: single Rhodamine dyes were imaged with a 5ms illumination time, resulting in a position accuracy of 30nm. During the years, SDT setup efficiencies were further optimized from $\sim 3\%$ up to maximum efficiencies of 12% [137]. Since nowadays the position accuracy is mainly limited by the number of photons received on the detector [148, 106], position accuracies can be optimized to the "one-nm" limit by increasing integration times in combination with the use of photostability enhancing chemicals for dyes (FIONA, Fluorescence Imaging with One-Nanometer Accuracy) [105, 149]. On the other hand, the upper limit for fast processes has been set at 22nm accuracy for an illumination time of 0.65ms and a frame rate of 1kHz [150].

High packing densities impair unambiguous identification and tracing of individual biomolecules [136]. Therefore, studying highly abundant biomolecules by SDT requires sublabeling, artificial reduction of expression levels in transfected cells [151], or locally pre-bleaching of the probed area (TOCCSL, [152]). A promising development is the improvement of the acquisition speed of novel high-resolution microscopy techniques like PALM. Recently, PALM-based tracking of clusters has been demonstrated, capable of tracking hundreds of trajectories simultaneously with an excitation time of 50ms per frame (spt-PALM, [153]).

The trajectory length and position accuracy are determined by the probes used in SDT to typically 10 to 100 frames and 20 to 50nm respectively [136, 135]. These limitations have their origin in the limited number of photons a probe can emit before photo-dissociation and in the autofluorescence of the cell at the probe's excitation wavelength. As a consequence, SDT is limited in its ability to probe the micro-environment of a single probed object, since for a given diffusion constant and environmental dimensions, the probe should be traced during a sufficiently long time, at a sufficiently high sampling rate and with a sufficiently short excitation time to catch its interaction with the surroundings [71, 154, 155]. To fulfill all these demands simultaneously, the probe should emit an unlikely number of photons before photo-dissociation. Different routes have been taken to address this physical limit in SDT. The photostability of probes has been prolonged by the use of reactive oxygen quenching agents and the development of stable red fluorescent fluorophores with a large stoke shift [149, 156]. The autofluorescent background has been reduced by development of red autofluorescent proteins [157]. Since the amount of emitted photons is still a limiting factor in SDT, analysis strategies have been developed to extract detailed mobility information out of datasets containing short trajectories.

1.8 Automated single particle tracking

The first tracking of individual receptors was performed by placing transparencies over a TV screen and tracing the particle positions in the time-lapse video recording. Yet, to elucidate the micro environment of probed biomolecules, a vast amount of trajectories needs to be analyzed with high accuracy and precision. With the development of computer and image processing technology, it became possible to automate most of the single particle tracking process. Single particle tracking algorithms extract trajectories of probed objects from image stacks with sub-micrometer precision. In the process of tracking, the precise localization of probes is critical. For localization of point sources, direct Gaussian fitting [119, 158] results in the best position accuracy and the signal to noise level of the images should exceed 4 [159]. In addition of position accuracy, the number of incorrectly linked particles should be minimized. New approaches improve this so-called "precision" of the algorithm by optimizing found trajectories in a spatio-temporal manner by minimizing the total trajectory length in an image stack [160, 161].

1.9 Analysis of trajectories

The diffusion behavior of traced biomolecules in the membrane has been modeled extensively [56, 73–75, 67, 162] and in many cases the observed mobility can be related to the interaction between the probed biomolecule and its environment. Generally, mobility has been classified with respect to random diffusion by means of calculation of the MSD (mean square displacement) over time lag curve [163, 123]. If an object exhibits random diffusion, its MSD curve can be fit with a linear function (see fig. 1.3). Non-random diffusion caused by interactions between membrane related biomolecules will induce a deviation from this linear relation. The different types of deviations from normal diffusion can be classified as anomalous or hindered diffusion, directed motion with diffusion and corralled or confined diffusion. The analytical forms of the curves of MSD versus time for these different modes of motion form the basis of various classification methods. The following analytical curves are used frequently

to classify the types of diffusion in a membrane [72, 123, 131]:

$$< r(t)^2 > = 4Dt \qquad \text{random diffusion} \qquad (1.1)$$

$$< r(t)^2 > = \Gamma t^{\alpha} \qquad \text{anomalous diffusion} \qquad (1.2)$$

$$< r(t)^2 > = 4Dt + (Vt)^2 \qquad \text{directed diffusion} \qquad (1.3)$$

$$< r(t)^2 > = \frac{L^2}{6} - \frac{16L^2}{\pi^4} \sum_{k=1(odd)}^{\infty} \frac{exp\{-(\frac{k\pi}{L})^2 \cdot D_{\mu} n\Delta t\}}{k^4} \qquad \text{corralled diffusion} \qquad (1.4)$$

Where $< r(t)^2 >$ is the mean square displacement, D is the diffusion constant and t the time of random walk. Anomalous subdiffusion before the crossover time can be described by a powerlaw in time, see formula 1.2, where Γ is the transport coefficient and α the time exponent [131, 73]. Parameter α gives a measure of the degree to which the motion is restricted by continuously changing traps with a wide spectrum of residence times[72, 131]. If a long time lag is chosen in relation to obstacle density (a time lag longer than the crossover time), the initial anomalous diffusion will be reflected as an additional offset at the origin of the MSD plot [150]. In some cases formula 1.2 is used to describe diffusion with a directionality; in those cases $\alpha > 1$ [131]. Though, in most cases diffusion with a directionality (velocity V) is described by formula 1.3. Confined diffusion can be described by the model function 1.4 [123]. Here, the object is trapped in a confinement zone with a compartment size of L^2, n is the number of time lags and Δt is the time for each frame. D_{μ} is the diffusion constant of the object at short time lags, when it is still unhindered by the confinement boundaries.

Different approaches have been taken to detect and classify modes of motion of probed biomolecules. Basically, modes of motion can be detected in the ensemble of many trajectories [158, 124, 164–166], they can be distinguished for each individual trajectory [123, 131, 132] or they can be detected within a single trajectory [133, 134, 154, 155, 167].

In case trajectories are obtained by SDT techniques, classification of individual trajectories is limited, since trajectory length and position accuracy are determined by photobleaching [136, 135]. Therefore, approaches have been developed to extract detailed information out of short trajectory datasets (trajectory length <20). To increase the dynamic range of SDT, data sets have been constructed including measurements at different frame rates [158, 124]. To deal with the heterogeneity of probed mobility, strategies have been developed to discriminate different types of mobility within an ensemble without the need to classify each trajectory individually [158, 124, 165, 166]. A successful strategy fits the cumulative probability distribution (CPD) of square radial displacements with a solution of Fick's second law, representing the sum

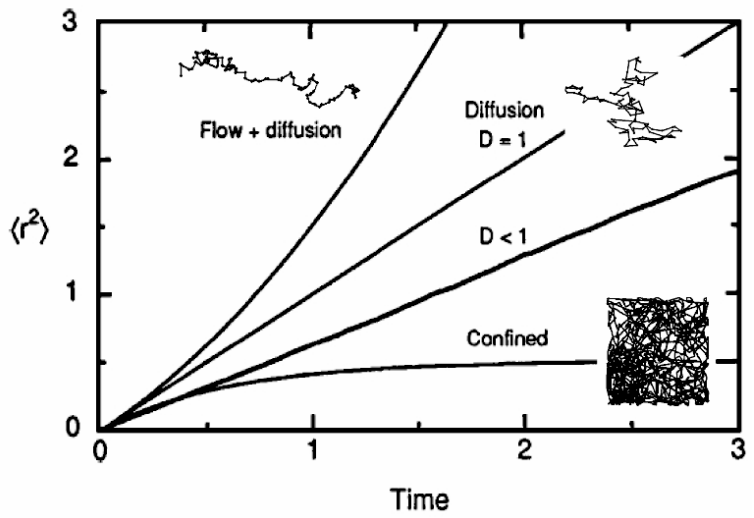

Figure 1.3. *Analytical forms of different types of diffusion [72]. The upper curve shows directed motion with diffusion, the straight line represents random diffusion, the next curve represents diffusion in the presence of obstacles (a form of anomalous diffusion) and the last curve represents confined diffusion. Insets: examples of representative trajectories are shown.*

of two randomly diffusing components [158]. Recently, a method has been developed to detect and characterize two diffusion components by particle image correlation spectroscopy (PICS), without the need to trace individual objects [164].

In case trajectories are obtained by SPT techniques, trajectory length is not a limiting factor and trajectories can be classified individually provided that the sampling rate is sufficiently high and exposure time is sufficiently short to reveal the environment's details [71, 154, 155]. Nevertheless, classification of individual trajectories can be impeded if individually probed biomolecules switch frequently between different modes of motion. Therefore, methods have been developed to detect multiple modes of motion within a single trajectory [133, 134, 154, 155, 167].

1.10 Aim of this thesis

Rapidly switching adhesion mechanisms are like 'the hand and the feet' of immune cells: they provide leukocytes with the ability to patrol, to collect and to pass information about pathogenic material throughout the body. How

leukocytes modulate their adhesiveness during the different stages of their life cycle, has been a central question in immunology. The integrin LFA-1 plays a crucial role in leukocyte arrest and migration through the vasculature and in binding to antigen presenting cells. Besides affinity and valency, LFA-1 mobility plays a role in regulation of LFA-1 mediated adhesion. Evidence is building up that affinity, valency and mobility are tightly interrelated to control LFA-1 mediated adhesion.

It has been demonstrated that on resting blood derived monocytes LFA-1 is distributed in active (extended conformation) and inactive (bent conformation) nanoclusters on the cell membrane [3]. Live imaging of monocyte - T cell conjugates showed that only active nanodomains were recruited to the binding site. Upon differentiation of monocytes into imDCs, membrane LFA-1 organization in active and inactive nanoclusters disperses and its affinity reduces while the expression level remains constant. These changes in the affinity and organization of LFA-1 have direct consequences for LFA-1 mediated binding capacity, which is strongly reduced on imDC compared to monocytes [3]. So far LFA-1 mobility on monocytes and immature DCs has not been monitored and/or related to affinity and distribution, and its potential consequences for cell adhesion have not been investigated yet.

The aim of this research has been to investigate the lateral mobility of the integrin receptor LFA-1. By using single molecule techniques, we have been able to deepen our understanding of LFA-1 mobility and its consequences for LFA-1 affinity and avidity regulation on monocytes and imDCs.

1.11 Thesis overview

First, we present an integral set of tools for single molecule sensitive detection, tracing and analysis of diffraction limited, heterogeneously distributed LFA-1 nanoclusters on the membrane of living monocytes (**Chapter 2**). Then, we inquire on the mobility of active and inactive LFA-1 nanoclusters on resting and ligated monocytes (**Chapter 3**). We show that on resting cells 95% of the LFA-1 is mobile and we distinguish immobile, slow mobile and fast mobile subpopulations, which differ in size and ensemble behavior for active and inactive nanoclusters respectively. When cells are adhered to ICAM-1 functionalized surfaces, active nanoclusters are recruited to the binding site. Furthermore, the mobility of LFA-1 is affected both at the regions of contact with ICAM-1 as well as on the ligand free regions, suggesting long range interactions within the cell. In **chapter 4**, we investigate LFA-1 mobility on monocytes under different extracellular cation conditions. Briefly, our results show that LFA-1 mobility is controlled by extracellular Ca^{2+} levels, affecting tethering of nanoclusters to the cytoskeleton and the balance between slow mobile and fast mobile nanocluster subpopulations. On the other hand, Mg^{2+} ions did not play

a major role in regulation of LFA-1 mobility. We investigate LFA-1 mediated adhesion in shear flow essays and show that under low shear flow conditions, mobility and affinity are both important factors for cell binding, while under higher shear flow conditions, affinity plays a more important role for LFA-1 mediated cell adhesion. Finally, differences in LFA-1 mobility between monocytes, imDCs and Jurkat T cells are investigated (**Chapter 5**). Observed differences in LFA-1 mobility have been assigned to differences in the spatial organization of LFA-1 and to a reduced activity of LFA-1 on imDCs and resting Jurkat T cells. To conclude, chapter 6 discusses the overall findings of this research and provides an outlook for future experiments.

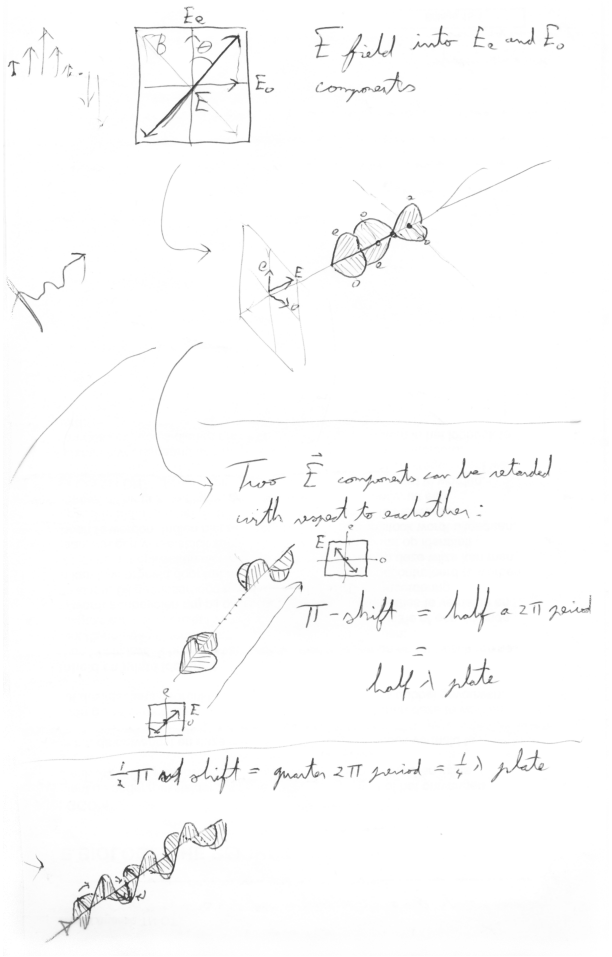
E_e
E_o
E
$\vec{E}$ field into E_e and E_o components
Two $\vec{E}$ components can be retarded with respect to each other:
π-shift = half a 2π period
=
half λ plate
$\frac{1}{2}\pi$ shift = quarter 2π period = $\frac{1}{4}\lambda$ plate

Chapter 2

Tracing Nanoclusters on Living Cells with Single Molecule Detection Sensitivity

In the last decade the focus of attention around single dye tracing (SDT) has changed from 'how' to 'what'. Until only a few years ago, SDT was mainly focussed on tracing single receptors, lipoproteins and other relatively simple systems. However, the last couple of years have witnessed an increase on the number and quality of papers regarding the study of complex systems using SDT. Here we present an integral set of tools for single molecule sensitive detection, tracking and analysis of diffraction limited LFA-1 (lymphocyte function-associated antigen 1) nanoclusters on the membrane of live monocytes. A combined EPI-TIR (Total Internal Reflection) fluorescence microscope with single molecule detection sensitivity has been implemented with a dual-color detection scheme, capable of imaging transmembrane receptor nanoclusters on the membrane of living cells with high speed and precision. Typical localization accuracies were 37nm for single fluorescent molecules (Atto647N) on glass and 47nm for single LFA-1 nanoclusters on fixed monocytes. Colloidal particle tracking algorithms have been successfully modified and implemented for semi-automatic tracking of individual LFA-1 nanoclusters that have a heterogeneous packing density and a wide range of mobility behavior. Furthermore, we have developed a robust software to distinguish subpopulations of different mobilities and estimate their respective size and ensemble behavior. The 'toolbox' presented in this chapter will be used throughout this thesis to investigate the dynamics of LFA-1 under different settings and cell systems.

2.1 Introduction

With the advent of single dye tracing (SDT, [147, 136]) and single particle tracking (SPT, [72]) approaches, the full dynamic character of living cell systems has come to reach. In particular, SDT can probe mobility of individual bio-molecules with nanometer precision while minimizing the chance of probe-induced artifacts with respect to SPT (Single Particle Tracking). Furthermore, since SDT is based on single fluorophores, including autofluorescent proteins, one can also exploit the specific spectroscopic properties of these quantum systems to obtain additional information on the nanoscale surroundings, i.e., inter- and/or intramolecular interactions, pH-changes, rotational mobility etc. [136]. During the last decades, SDT localization accuracy and image acquisition speed have been pushed to their limits and automated particle tracking algorithms are being continuously upgraded in terms of performance and complexity [168, 105, 150, 160, 161].

Despite these advantages, SDT has been mainly used so far to explore the dynamics of relatively simple systems such as single receptors. Only the last couple of years have witnessed an increase on the number and quality of papers regarding the study of complex systems using the technique [62, 70, 169]. This is mainly due to the limited number of photons obtained by fluorophores before photobleaching restricting the length and temporal scale under investigation. As a consequence, quantum dots are increasingly used nowadays to report on the mobility of receptors in more complex settings, such as their interaction with the cytoskeleton and/or other molecular organizers of the cell membrane [125, 126]. In here we will develop methods to thoroughly derive the different diffusion profiles of LFA-1 in its surrounding while taking the advantages of the SDT approach.

Yet, to study more complex systems by SDT, several challenges need to be overcome. First, trajectory length and localization accuracy are determined by the probes used in SDT to typically 10 to 100 frames and 20 to 50nm respectively [136, 135]. These limitations have their origin in the limited number of photons a probe can emit before photo-dissociation and in the autofluorescence of the cell at the probe's excitation wavelength. As a consequence, SDT is limited in its ability to probe the micro-environment of a single probed object, since for a given diffusion constant and environmental dimensions, the probe should be traced during a sufficiently long time and at a sufficiently high sampling rate to catch its interaction with the surroundings [71, 154, 155]. To circumvent the limitations of conventional dye probes, several approaches have been developed to extract detailed information out of short trajectory datasets (trajectory length <20). To increase the dynamic range of SDT, data sets have been constructed including measurements at different frame rates [158, 124]. To deal with the heterogeneity of probed mobility, strategies have been developed to discriminate subpopulations with different types of mobility without

the need to classify each trajectory individually [158, 124, 165, 166].

Second, SDT of complex systems is also challenged by the expression levels and distribution of lipids or proteins of interest on the cell membrane. This distribution can be very dense or heterogeneous and expression levels might vary on a cell-to-cell basis. Since SDT requires sub-labeling conditions, artificial reduction of expression levels in transfected cells [151], or local pre-bleaching of the probed area (TOCCSL) is commonly applied [152]. The former two techniques are not optimal for heterogeneous packing densities as only a small fraction of the cells will be suitable for analysis. In addition, TOCCSL is not adequate when an immobile fraction is present within the total population of probed molecules. It is therefore highly desirable to use an algorithm that is able to deal with the heterogeneity by selecting in an automated way specific areas of the membrane where labeling conditions are such that SDT can be performed in an optimum way.

Here we present an integral set of tools for single molecule sensitive detection, tracing and analysis of diffraction limited sized individual nanoclusters of transmembrane receptor proteins on the membrane of living cells. We first described the developed EPI-TIR fluorescence microscope and dedicated tracking/analysis software. We tested the overall performance of the setup, in particularly the localization accuracy and detection efficiency. Furthermore, we tested the algorithm to follow individual nanoclusters of the integrin receptor LFA-1 on live monocytes. By combining mean square displacement analysis of individual trajectories and cumulative probability distributions of the total dataset, we distinguished, quantified and characterized three distinctive diffusion modalities. The tools developed in here will be used in the next chapters to deepen our understanding on the diffusion of different LFA-1 conformations under different extracellular cation and ligation conditions.

2.2 Materials and Methods

2.2.1 Sample preparation

Antibody conjugates

The antibody conjugate NKI-L16-Atto647N was kindly provided by the Tumor Immunology Laboratory, (NCMLS, the Netherlands). Activation reporter mAb NKI-L16 (further referenced as L16) is reactive with the alpha subunit of integrin receptor LFA-1 [3]. L16 antibodies were labeled by conjugation of fluorophores to the thiol-groups. The labeling ratio of the L16 antibody-fluorophore conjugate was $\sim$ 1:0.8, as determined by analysis of absorption spectra of antibody solutions.

Cell lines and cell culture

THP-1 monocytes (referenced as monocytes) were cultured in RPMI medium without phenol red, with L-glutamine, 10% FBS and 1% antibioticantimycotic. Cells were maintained at a concentration between 200.000 and 1.000.000 cells/ml by re-suspension in fresh medium every other day. The day before the experiment, cells were placed at a concentration of 400.000 cells/ml.

Sample preparation

Glasses were coated with PLL (Poly-L-Lysine, Sigma-Aldrich, P1524) by 1 hour incubation in PBS with $50\mu g/ml$ PLL. Chambered cover glasses were coated with Fibronectin (Sigma-Aldrich, F2006) by 30 minute incubation with $20\mu g/ml$ Fibronectin dissolved in PBS and rinsed once with RPMI medium. THP-1 cells were re-suspended in RPMI and plated at a concentration of $1.25 \cdot 10^5$ cells/ml. After 15 minutes of incubation, unbound cells were removed. Samples were blocked by a 15 minute incubation with 1% Human Serum in RPMI. After blocking, samples were rinsed twice with RPMI and incubated with L16-Atto647N antibody conjugates in RPMI medium at a concentration of 0.2 $\mu g/ml$ for approx. 4min. After labeling, samples were rinsed twice and finally RPMI without phenol red was used as imaging medium. Fixed samples were prepared in a similar manner but were fixed right after the last rinsing step. Samples were kept in fixative (2% PFA in PBS, filtered) overnight and measurements were also done in fixative. Antibody on glass samples were prepared by incubation of an 0.01 $\mu g/ml$ antibody solution on glasses coated with PLL. Rinsed glasses were measured in RPMI. Microscope slides were cleaned with detergent and water, rinsed thoroughly with MilliQ water and cleaned in ethanol (absolute, extra pure) before being air-dried and UV-cleaned. Alternatively, sterile 8-well LabtekII chambered cover glasses were used. All incubation steps were performed at 37 °C.

2.2.2 High-speed dual color EPI-TIRF microscopy with single molecule detection sensitivity

The experiments were performed using a home-made combined EPI-TIR fluorescence (TIRF) microscope. The setup was built around an Olympus IX71 microscope with an Olympus 60x TIRFM objective (PLAPO 60x0TIRFM NA 1.45) and an Intensified CCD camera (Princeton Instruments, I-Pentamax, version 5, genIV photo cathode), see figure 2.1. The setup can work in EPI fluorescence or TIRF mode, single or dual color mode using an AOTF-based (Acousto-Optical Tunable Filter) gated excitation scheme.

Through-the-objective-TIR excitation was chosen because of its simplicity and the possibility of switching from EPI to TIR mode during a measurement

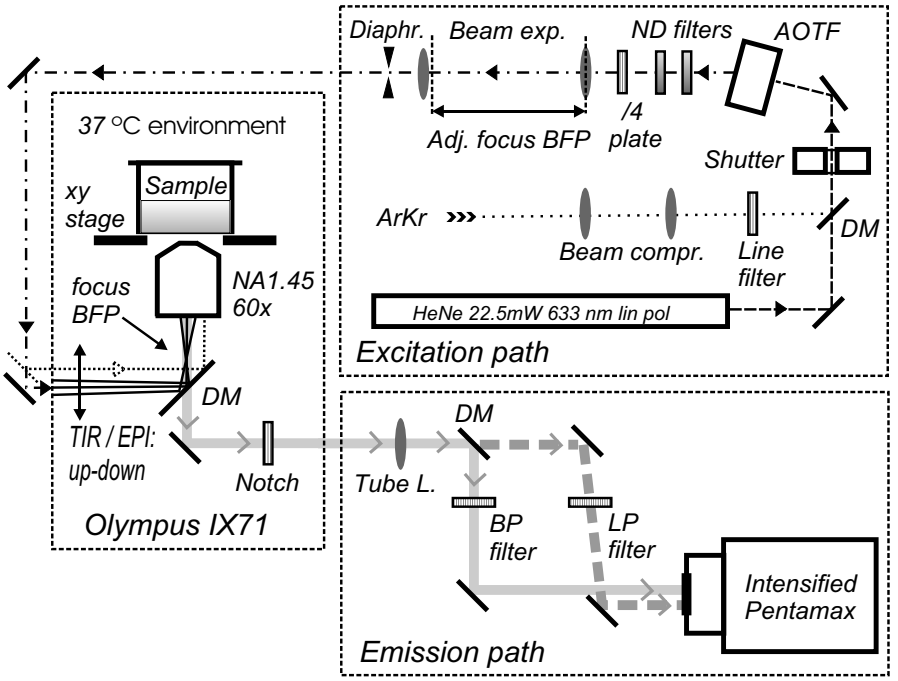

Figure 2.1. *Schematics of the dual-color excitation/detection EPI-TIRF microscopy setup. The actual microscope, excitation and detection paths are highlighted by dash lines to easier visualization of the set up.*

[170]. A two-color detection scheme has been implemented with emission separation and filtering after the final lens before the camera to minimize chromatic aberration and emission light losses.

Excitation path

For excitation, the 514-nm line of an Ar^+Kr^+ laser (Spectra Physics, Model 2060) and the 633-nm line of a HeNe laser (JDSU, Model 1145p, 22.5mW) were used. After beam compression and line filtering (Semrock, LL01-514), the Ar^+Kr^+ laser line was combined with the HeNe laser line using a dichroic mirror (Semrock, FF593). The overlapping beams were led through a mechanical shutter (Vincent Associates, LS2) to an AOTF (A.A, AA.AOTF.nC) for beam selection, timing and attenuation. A broadband $\lambda/4$-plate (Newport, 10RP44-1) and a carousel of neutral density filters provided circular polarized excitation

light with varying intensity. The selected laser line was steered through a 10 or 5 times beam expander which focused the beam at the BFP (Back Focal Plane) of the objective. A diaphragm was placed after the second lens of the beam expander blocking half of the power. This configuration resulted in a relatively flat clipped Gaussian excitation profile with a diameter of 26 or 13 μm. The maximum average power density was 1 or 4 kW/cm^2 for the HeNe excitation and 2 or 6.5 kW/cm^2 for the 514-nm excitation line.

Emission path

The fluorescence emission collected by the TIRF objective was separated from the excitation by a dichroic mirror (Omega Optical, 436-510DBDR XF2065) and a 16-nm broad and 6 OD deep notch filter centered around 514.5 nm (Semrock, NF01-514U25). The emission light passed a tube lens outside the microscope (Newport, PAC096, f=500mm) before it was split into two different paths by a second dichroic mirror (Omega Optical, 560 DCLP/E XF2016/E), see figure 2.1. The long wavelength emission path was long-pass filtered (Semrock, LP02-647RU-25) and the short wavelength emission path was band-pass filtered (Chroma HQ560-80m) in between the tube lens and the intensifier of the CCD camera. One pixel on the camera (22.5 μm) corresponded to 135 nm in the objective focal plane. The intensifier gain was set to a value of 65 units (see paragraph 2.3.1 for a more detailed description of the intensifier settings). Phase contrast (LCPLFL 60xPH, CPLN 10xPH/0.25 objectives) and DIC (TIRFM objective) were used to obtain bright field images with enhanced contrast.

Camera and excitation control

Localization inaccuracy due to mobility of the probe during the excitation can easily be minimized by controlling the excitation time. By independent control of pulse length and pulse power for both excitation channels during a two-color experiment, excitation conditions were optimized according to each probed protein or lipid individually (fig. 2.2). The camera settings were controlled by the standard Winview32 software supplied by Roper Scientific. The camera triggering, laser line selection, attenuation and timing were controlled by a home made Labview script. Only a part of the CCD chip was used for imaging. ROIs (Regions Of Interests) of 170 x 170, 200 x 200 (single color mode) and 200 x 400 (dual color mode) pixels were used. Cells were imaged at frame rates of 20Hz. Unless stated otherwise, the pulse lengths were set to 4ms (HeNe) and 2ms (514-nm line) while the power densities were set to its maximum (1 and 6.5 kW/cm^2) for a 26μm excitation diameter.

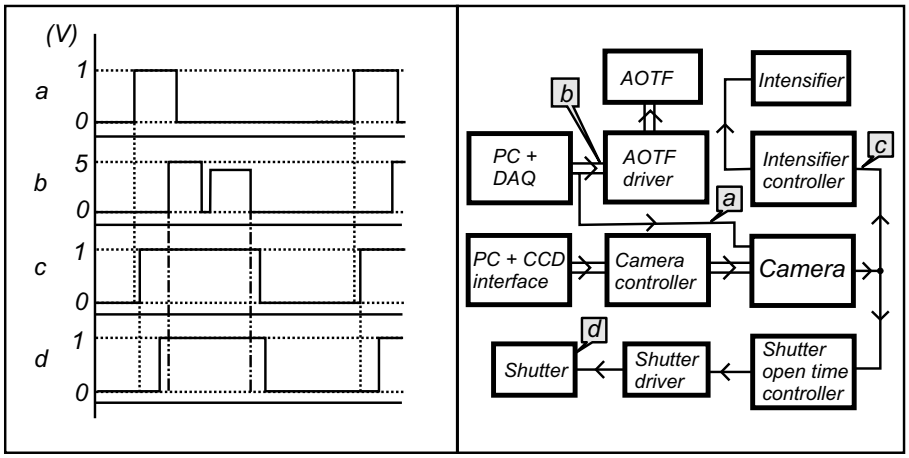

Figure 2.2. *Block diagram and pulse scheme of the camera and excitation control. The camera was coupled to a PC for frame grabbing and for controlling of settings such as excitation time and number of frames (see block diagram). The camera was triggered externally by another PC with a DAQ card (National Instruments) generating pulses continuously, see pulse scheme 'a' probed at position 'a'. This PC also generated pulses to control the AOTF (b). Trigger and excitation pulses were generated by a home made Labview script in such a way that excitation pulses overlapped with the camera exposure time (pulse scheme c) and started after the mechanical shutter opened (pulse scheme d), see vertical lines dropping from pulse scheme 'b'. The intensifier was activated by a TTL output of the camera, which was high during the exposure time of the camera. A mechanical shutter was used to block the excitation when no frames were retrieved. The mechanical shutter opened with 1 ms delay upon the rising flank of the TTL output and the 'open time' of the shutter was controlled by a home-made control box.*

Temperature control

A custom-made incubator was built around the upper half of the microscope body to maintain the sample at 37 °C while temperature gradients over the microscope body and parts involved in focussing remain stable for TIR fluorescence microscopy. The temperature control was realized by recirculation of the air in the incubator box through an external heater-controller unit (WPI, Air-Therm Z-ATX, 0.2 °C accuracy). After overnight stabilization of the microscope at 37 °C, no drift was observed during measurements ($<$ 1 minute).

2.2.3 Single nanocluster tracing on living cells

An algorithm for tracking of high densities of colloidal particles ([171], translated to Matlab by Daniel Blair and Eric Dufresne) was adapted for tracing fluorescently labeled protein nanoclusters on living cells. To track the particles, the original algorithm filtered the images spatially. Nanoclusters were then discriminated from the background by setting a threshold and the (x,y)-positions were determined by finding the center of mass of the local maxima. The found positions in the individual frames were linked together into trajectories.

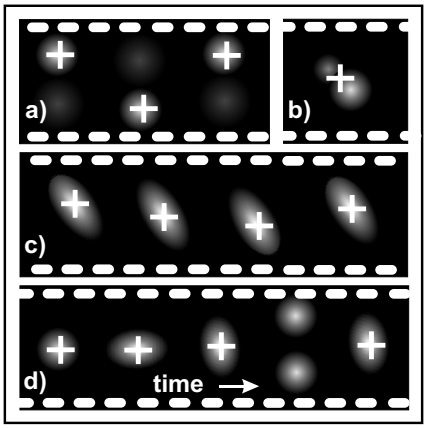

Figure 2.3. *Events in movies that can 'fool' most tracking algorithms. The images show frames sequenced in time and the detected positions of fluorophores are highlighted by crosses. a) Two adjacent spots with intensities fluctuating around the intensity threshold have the potential to cause intermixing in the tracking algorithm. b) When two fixed spots are separated by a distance in the order of the diffraction limit, a mobility artifact can be caused when one of the spots is blinking. c) A potential artifact caused by spots larger than the diffraction limit of light with a heterogeneous and dynamic distribution of intensity. d) Artifact caused by close-by (beyond the diffraction limit) moving fluorophores.*

To avoid intermixing of traced nanoclusters in dense areas, the typical single cluster displacement δ should be sufficiently smaller than a typical interparticle distance d: $\delta < L < d/2$ where L is the maximum allowed displacement of a nanocluster between two consecutive frames (as already implemented in the unmodified algorithm) [171]. Inspection of the CPD (Cumulative Probability Distribution) of radial displacements was used to estimate the correct L: a truncated CPD curve indicated an underestimated L. A maximum interparticle distance d_{limit} was set in the customized algorithm to remove nanocluster positions that violate $\delta < L < d/2$. In this way, highly dense areas were

excluded from the analysis till bleaching of probes reduced d sufficiently. Potential artifacts due to spot intensity fluctuations (fig 2.3a) were reduced by setting a second threshold at a lower intensity level. This threshold was used to remove all local maximums being closer to each other than d_{limit} within one frame, while the high threshold was used to find the most appropriate positions that had a sufficiently high signal to background level. Furthermore, spot intensity and radius of gyration outputs of the unmodified algorithm were used to discriminate bright, small or large spots (camera artifacts, label aggregates and autofluorescence) from regular spots (single dye molecules and diffraction limited nanoclusters).

After generation of trajectories a ROI was drawn manually to select specific areas of the cell. Trajectories that were more than 30% outside the border were excluded from the dataset. Finally, a tool for visual inspection of individual trajectories was implemented. Artifacts represented in figure 2.3 b) and c) were recognized by repetitive steps in between two fixed positions of a trajectory in its (x,y)-plane. Potential artifacts due to loss of tracking or particle interchange were recognized by abrupt deviations of the displacement distances and the Intensity-time trace of the trajectory. Furthermore, a Mean Square Displacement (MSD) plot of the represented trajectory was used for inspection. MSD points were derived as discussed below and depending on the trajectory length, they were fitted by a linear function through the first three or four points. Potential tracking artifacts were recognized if the offset of the fit exceeded $0.020\mu m^2$ or when the fit failed to go through the error bars of the first MSD points. Finally, the software included the simultaneous visualization of a movie with an enlarged view on the trajectory place and the found cluster position to allow visual inspection of the algorithm performance.

2.2.4 Data Analysis

For each traced nanocluster, the MSD ($< r(t)^2 >$) versus timelag plot was generated using the formula [163, 123]:

$$MSD(n \cdot \Delta t) =$$

$$\frac{1}{(N-1-n)} \sum_{j=1}^{N-1-n} [x(j\Delta t+n\Delta t)-x(j\Delta t)]^2 + [y(j\Delta t+n\Delta t)-y(j\Delta t)]^2 \quad (2.1)$$

where Δt is the frame period, N is the trajectory length expressed in the number of frames and $x(j\Delta t + n\Delta t)$, $y(j\Delta t + n\Delta t)$ describes the fluorophore position following a time lag $t = n \cdot \Delta t$ after starting at position $x(j\Delta t)$, $y(j\Delta t)$. n and j are positive integers, n represents the time lag. The algorithm has been adapted to incorporate trajectories containing single-frame interruptions. A linear fit was made through the first three or four time lags of the MSD curve.

In order to avoid interdependence between squared displacements and scatter in the MSD plot, trajectories were fitted through not more than $1/4^{th}$ of the total number of time lags [172]. As a result, short trajectories (13-16 frames) were fitted through the first 3 time lags and longer trajectories (> 16 frames) were fitted through the first 4 time lags using the relation:

$$< r(t)^2 >= 4Dt + {\Delta_0}^2 \tag{2.2}$$

Where ${\Delta_0}^2$ is the MSD offset at time zero. Throughout this work, we define D as the short time diffusion constant in the derived MSD plot. We assume that the proteins have minimum interaction with obstacles in their micro-environment during the first three or four time lags, implying random diffusion behavior during these first time lags [123]. Finally, the short time diffusion constants of all analyzed trajectories were included in a histogram.

Since D at short time lags do not report on the long-term diffusion behavior, we applied cumulative probability distribution (CPD) analysis to enquire on the type of diffusion exhibited by the mobile fraction of nanoclusters ($D \geq D_{th}$) over a long time interval (1.5 s) [158]. The CPD of square displacements was fitted with a two- (or one-) component Fick's law based function as a model:

$$P(r^2, t) = 1 - \left[f \cdot exp\left(-\frac{r^2}{r_1^2} \right) + (1 - f) \cdot exp\left(-\frac{r^2}{r_2^2} \right) \right] \tag{2.3}$$

Where $P(r^2, t)$ is the probability that a particle starting at the origin will be found within a circle of radius r at time lag t; where fit parameter f is the fraction of the first component and $(1 - f)$ is the fraction of the second component. The fit parameters r_1^2 and r_2^2 represent the square displacements of both components. Square displacement curves were retrieved for both diffusion components by fitting the CPD at increasing time lags. The errors in the square displacements were estimated by bootstrapping (resampling residuals approach) [173, 174]; the error bars represent 2 times the standard deviation. The type of mobility of the subpopulations was classified by fitting their square displacement curves with functions associated to the different classes of mobility, as defined by single particle tracking [72].

2.3 Results

2.3.1 Characterization of intensifier gain

To maximize the dynamic range of the intensifier-camera combination and to minimize the amount of speckles in the images, the intensifier gain setting was

optimized to single molecule sensitivity with a wide dynamic range. For a single molecule representative illumination power in the order of 90 photons per pixel on the intensifier, the camera became shot noise limited on a single pixel level (signal to noise ratio = 5.3) between a gain setting of 50 and 60 arbitrary units. We chose an intensifier setting of 65 a.u. for all measurements, corresponding with a real gain of 20.1. Since a count corresponds to 20 electrons, each count corresponds to approximately one photon-electron created by the intensifier phosphor layer on the detection side. To be able to estimate the shot noise limited gain setting in future experiments by means of a simple calculation, the real gain of the intensifier was characterized as a function of gain setting, see figure 2.4. An exponential relation between intensifier setting and gain was found.

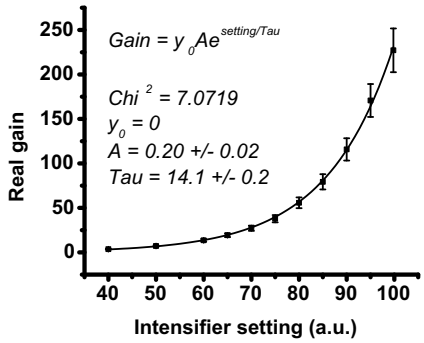

Figure 2.4. *The relation between intensifier setting and real (photon-electron) gain. The data was fitted with an exponential function.*

2.3.2 General setup performance

The number of photons detected per single molecule per frame (N_{sm}), the background level per frame (N_{bg}) and the signal-to-background level for detection of single molecules (SB) were determined for L16-Atto647N conjugates on glass in buffer and for L16 labeled LFA-1 nanoclusters on fixed THP-1 cells, see table 2.1. In case a recorded LFA-1 nanocluster was labeled with multiple fluorophores, only the last bleaching step in an intensity-time trace was taken into consideration to retrieve N_{sm} and SB, see fig. 2.5. Probes were excited as described in section 2.2.2. N_{sm} was derived by integration of the number of counts over 13 pixels, substraction of the background level and multiplication by the gain factor.

	$\mathbf{N_{bg} \pm \sigma}$	$\mathbf{N_{sm} \pm \sigma}$	**SB**
L16-Atto647N (glass)	100	180±47	1.8±0.5
L16-Atto647N (cells)	130	225±63	1.7±0.5

Table 2.1. *N_{sm} and SB were derived by taking the average and standard deviation (σ) over results obtained from eight intensity-time traces.*

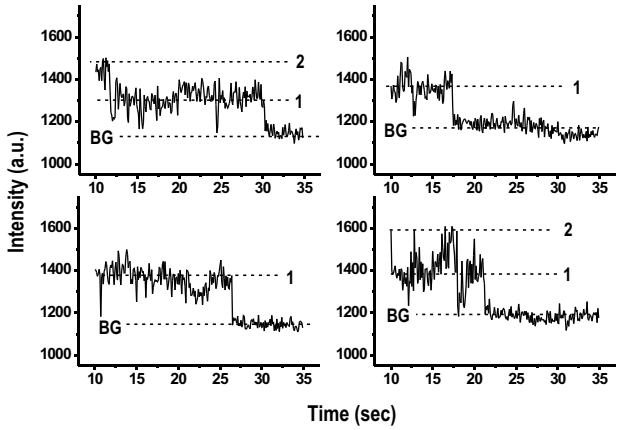

Figure 2.5. *Representative examples of one- or two- step photobleaching of L16-Atto647N labeled LFA-1 nanoclusters on the surface of fixed THP-1 cells. The intensity-time traces of individual LFA-1 spots imaged for ∼25s show the characteristic discrete steps of photobleaching of individual dye molecules (one or two steps in the examples given). BG: background level.*

The total detection efficiency of the setup was given by the numerical aperture of the objective, by the intensified camera and the chosen dye-filter combinations. The SNR (The signal-to-noise ratio) of the intensified camera is limited by the shot noise and the variance in the amplification process of the intensifier. The maximum quantum efficiency of the camera is 45% at a wavelength of 600nm and it should be multiplied by a factor $1/\sqrt{2}$ in order to correct for the variance in the amplification process. Dye-filter combinations were chosen in such a way that crosstalk between emission channels was less than 5%. The setup detection efficiencies can be estimated for the detection of Atto520 and Atto647N molecules:

$$\eta_{det} = A \cdot B \cdot \eta_{obj} \cdot \eta_{ICCD} \tag{2.4}$$

Where A includes all mirror and lens contributions, B includes all filter efficiencies for the given dye molecules, η_{obj} is the combined objective collection and

transmission efficiency and η_{ICCD} represents the corrected intensified camera quantum yield. The estimated detection efficiencies were ∼6% and ∼7% for Atto520 and Atto647N respectively.

2.3.3 Dual-color performance

The two-color detection scheme was tested by means of a calibration sample with multi-color diffraction limited fluorescent beads, see figure 2.6. The aberration was estimated by determination of the bead positions for both images. The maximum (direction dependent) aberration was 0.72 pixel = 0.10 ± 0.02 μm over a distance of 10 μm. During single molecule sensitive dual-color experiments with Atto520 and Atto647N dyes, no crosstalk due to labeling itself was observed (result not shown).

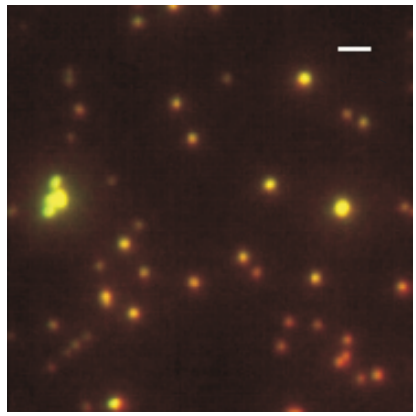

Figure 2.6. *Overlay of two images of the same multi-color fluorescent beads recorded simultaneously through two emission channels. A mixture of three different types of diffraction limited beads was imaged (Tetra-Speck^{TM} and PS-Speck^{TM} orange and deep-red beads, Molecular Probes), resulting in different spot colors. Long wavelength emission is represented in red, short wavelength emission is represented in green and in case of perfect overlay beads appear homogeneous yellow or orange in color. Since not all spots represent single beads, intensity varies. Scale bar: 2μm.*

Color aberrations in the direction of the optical axis were minimized by adjustment of the mirrors in the emission paths. Due to the positioning of the final (and only) imaging tube lens before the emission channel separation, filter and mirror induced distortions of the objective's point spread function are negligible. Therefore, colocalization can be determined without extensive

image correction measures. Nevertheless, in case that higher colocalization is required, found spot positions can be corrected by a linear correction function [140]. The correction function parameters can be found by calibrating the images with beads added to the sample.

2.3.4 Accuracy

Position accuracy

The position accuracy of a single traced fluorescently labeled protein or molecule is the ultimate measure for the performance of the total setup. It includes the setup detection efficiency, the performance of the used fluorescent probes, the ability to suppress (auto-) fluorescence background and the ability of the tracking program to determine the positions of individual fluorescent spots. Here the position accuracy is determined for individual Atto647N molecules immobilized on glass and for L16-Atto647N sub-labeled LFA-1 nanoclusters on fixed monocytes. The position accuracy can be determined in two ways:

First, the position accuracy has been estimated based on the formula presented by Thompson et. al. [106], taking into account the number of collected photons per molecule per frame (N, measurement presented in table 2.1), the pixelation noise (pixel size a), the background noise per pixel (b photons/pixel, as derived from table 2.1) and the estimation of the standard deviation of the point-spread function for wide field microscopy (s, 120 nm [141]):

$$\langle(\Delta x)^2\rangle = \frac{s^2 + \frac{a^2}{12}}{N} + \frac{8\pi s^4 b^2}{a^2 N^2} \tag{2.5}$$

For each dimension, an estimated position accuracy of 25nm was found for both single molecules on glass and sub-labeled nanoclusters on fixed cells respectively. Surprisingly, an equal positional accuracy was found for single molecules on glass and on fixed cells. This can be explained by the large error margins in the obtained N_{sm} (see table 2.1).

Second, the position accuracy can be determined from a direct measurement, taking the offset at the origin of a linear fit to the mean square displacement (MSD) curve. The MSD offset $< r(0)^2 >$ equals the squared displacement error ${\Delta_0}^2$ in case the dynamic contribution to the error is negligible (see par. 2.2 formula 2.2). Then, ${\Delta_0}^2$ is directly related to the position accuracy by $\langle(\Delta x)^2\rangle = {\Delta_0}^2/2d$ where d corresponds to the number of dimensions in which the diffusion takes place. Therefore, the 'static' position accuracy is given by $\sqrt{< r(0)^2 > /4}$. We determined ${\Delta_0}^2$ from the MSD of fixed fluorescent spots and calculated the 'static' position accuracy, see figure 2.7. For each dimension, the found position accuracies were 37nm and 47nm for single molecules on glass and sub-labeled nanoclusters on fixed cells respectively. As expected,

the position accuracy on cells is slightly lower than that of single molecules on glass. This is essentially due to the lower signal-to-background obtained on cell samples.

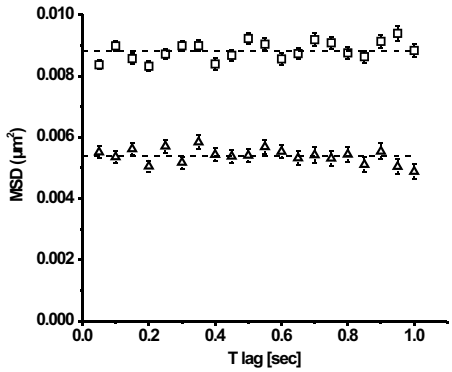

Figure 2.7. *MSD curves of fixed fluorescent spots. Open triangles: immobile L16-Atto647N conjugates on glass in buffer,* $< r(0)^2 >= 0.0053 \pm 0.0002\mu m^2$. *Open squares: immobilized nanoclusters on fixed cells,* $< r(0)^2 >= 0.0088 \pm 0.0002\mu m^2$.

In reality, the squared displacement error ${\Delta_0}^2$ also contains a dynamic component caused by the finite acquisition time. However, under our experimental conditions this effect will play a role at very large diffusion values ($D > 3.75\mu m^2/s$) [175]. Since the diffusion constant of $\beta 2$ integrin receptors on the cell membrane is orders of magnitude smaller [34, 28, 176], the effect of the dynamic error is thus negligible. Therefore, we conclude that we can determine the position of single nanoclusters under our experimental conditions with a precision of at least 47nm, which is well below the diffraction limit of the microscope and comparable to other SDT studies [177, 178, 169].

Determination of the minimum detectable diffusion constant

The diffusion constant D of a probed object is calculated from a linear fit through the MSD versus time lag points. The errors in the MSD points will depend on the position accuracy and on the trajectory length and they propagate in the error in D (ΔD). Also ΔD can be determined in two ways: first, ΔD can be estimated by a linear approximation of the error in the re-arranged derivative of ($< r^2 >= 4Dt$) to t (time lag):

$$D = \frac{1}{4} \cdot \frac{\partial < r^2 >}{\partial t} \tag{2.6}$$

$$\Delta D = \frac{1}{4} \cdot \Delta(\frac{\partial < r^2 >}{\partial t}) \tag{2.7}$$

The error in D is thus determined by the error in the slope of the linear fit through the MSD plot ($\Delta(\frac{\partial < r^2 >}{\partial t})$). Since the MSD remains constant in time for immobile spots, the following upper limit of the error in the slope of the fit can be estimated:

$$\Delta(\frac{\partial < r^2 >}{\partial t}) = ([\frac{\partial < r^2 >}{\partial t}]_{max} - [\frac{\partial < r^2 >}{\partial t}]_{min}) \tag{2.8}$$

In the case of the calculation of D by linearly fitting through the first 4 MSD points, this equation becomes:

$$\Delta(\frac{\partial < r^2 >}{\partial t}) = (\frac{\Delta < r(4\Delta t)^2 > + \Delta < r(\Delta t)^2 >}{4\Delta t - \Delta t} - 0) \tag{2.9}$$

Where $[\frac{\partial < r^2 >}{\partial t}]_{max}$ and $[\frac{\partial < r^2 >}{\partial t}]_{min}$ are the maximum and the minimum not-negative slope of a line that can be drawn through the error markers of the first ($< r(\Delta t)^2 >$) and the fourth ($< r(4\Delta t)^2 >$) MSD point in the MSD plot and Δt is the frame period.

Since motion is completely absent, the error in the MSD at time lag $t = n \cdot \Delta t$ is given by:

$$\Delta < r(t)^2 >= \frac{< r(0)^2 >}{\sqrt{N(t)}} \tag{2.10}$$

where $N(t)$ is the number of squared displacement points for the given time lag.

Finally ΔD can be derived by combining formulas 2.10, 2.9 and 2.7:

$$\Delta D = \frac{1}{12\Delta t} \cdot [\frac{< r(0)^2 >}{\sqrt{N(4\Delta t)}} + \frac{< r(0)^2 >}{\sqrt{N(\Delta t)}}] \tag{2.11}$$

and

$$D_{min} = 2 \cdot \Delta D \tag{2.12}$$

Clearly, D_{min} is linearly dependent on the square of the position accuracy and reciprocally dependent on the square root of the trajectory length (reflected by $N(\Delta t) + 1$) and the frame period Δt. For a trajectory length of 21 frames, a frame rate of 20Hz and a position accuracy of $47nm$, the estimated minimum detectable diffusion constant $D_{min} = 0.007\ \mu m^2/s$.

Second, D_{min} has been directly determined from measured trajectories of immobilized L16 labeled LFA-1 nanoclusters on fixed monocytes. Diffusion constants have been calculated for each individual trajectory by linear fitting

of the MSD plot through its first 4 points and results have been presented in a histogram, see figure 2.8. Due to the error in D, a distribution with a finite width will be observed, even if all probed objects are intrinsically immobile. We define the minimum detectable D as D_{min}, for which the null hypothesis 'the traced spot is immobile' can just be rejected with 95% certainty. In other words, $D_{min} = 2\sigma$, where σ is the standard deviation of the distribution of D of traced intrinsically immobile LFA-1 nanoclusters.

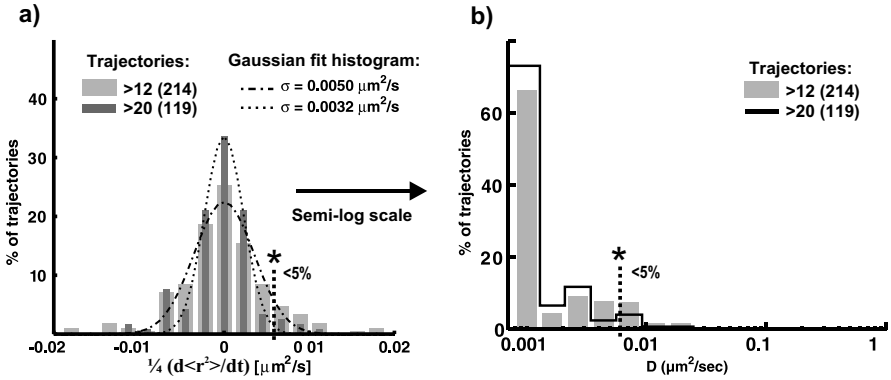

Figure 2.8. *The distributions of diffusion constants of L16 labeled LFA-1 nanoclusters on fixed THP-1 cells for different minimum trajectory lengths (see legends). The bars in the histogram were normalized to the total number of trajectories. a) The data is represented in a linear histogram and fitted with a Gaussian function to determine the standard deviation (σ) of the distribution. To avoid confusion on the physical meaning of a negative MSD derivative, the x-axis is named $1/4[\partial < r^2 > /\partial t]$ instead of D. b) The distribution of D of immobile nanoclusters has been represented in a semi-logarithmic histogram. *: boundary D_{min} for a min. trajectory length of 21 frames.*

As shown in figure 2.8a), the found distribution of MSD linear fit derivatives was symmetric and very well fitted by Gaussian functions. We derived D_{min} by taking $2 \cdot \sigma$ of the fit: for a minimum trajectory length of 21 frames $D_{min} = 0.006\mu m^2/s$ and for a minimum trajectory length of 13 frames $D_{min} = 0.01\mu m^2/s$. As expected, D_{min} decreased upon increase of the minimum trajectory length. The experimental results obtained are in excellent agreement with the estimated D_{min}. In the following we will use the experimentally determined D_{min} to discriminate the mobile fraction from the total trajectory population. Furthermore, we will use diffusion histograms like the one shown in fig. 2.8b to discriminate and quantify the immobile subpopulation with respect to the total population of LFA-1 nanoclusters on living cells.

2.3.5 Imaging and tracing individual fluorescent nanoclusters

The imaging, localization and tracing of individual dye-labeled LFA-1 nanoclusters on the dorsal side of living monocytes is demonstrated in figure 2.9. It is possible to trace individual nanoclusters within a heterogeneous packing

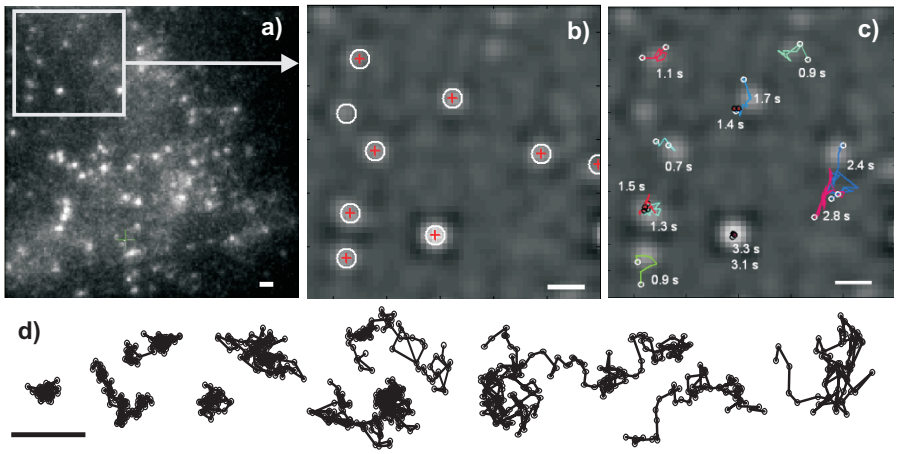

Figure 2.9. *Tracing of dye-labeled LFA-1 nanoclusters on the dorsal side of living monocytes. Images were taken at a frame rate of 10 Hz (figure pane a, b and c). (a) Representative frame illustrating the fluorescent signal of labeled LFA-1 nanoclusters. (b) Nanocluster positions are determined with 47nm accuracy after spatial filtration of the image. (c) Nanocluster positions are linked together into trajectories. d) Representative trajectories of L16-Atto647N labeled LFA-1 nanoclusters. Framerate: 20Hz, scale bar: 1 µm.*

density at a relatively high background level with single molecule detection sensitivity. The LFA-1 nanoclusters on THP-1 cells show a broad spectrum of mobility behavior (fig. 2.9d). Figure 2.10 illustrates the implemented routine to monitor several parameters of a traced nanocluster simultaneously.

2.3.6 Analysis of nanocluster trajectories

The observed heterogeneity in the mobility of LFA-1 prompted us to develop a rigorous analysis approach to dissect and characterize different mobilities within the ensemble of a single SDT dataset. To begin with, we inquired on the short-time diffusion constant D for every individual trajectory and all D's have been presented in a semi-logarithmic histogram, see fig. 2.11. The distribution displays a peak with a shoulder, suggesting at least two mobility subpopulations. Also, a considerable immobile subpopulation can be observed.

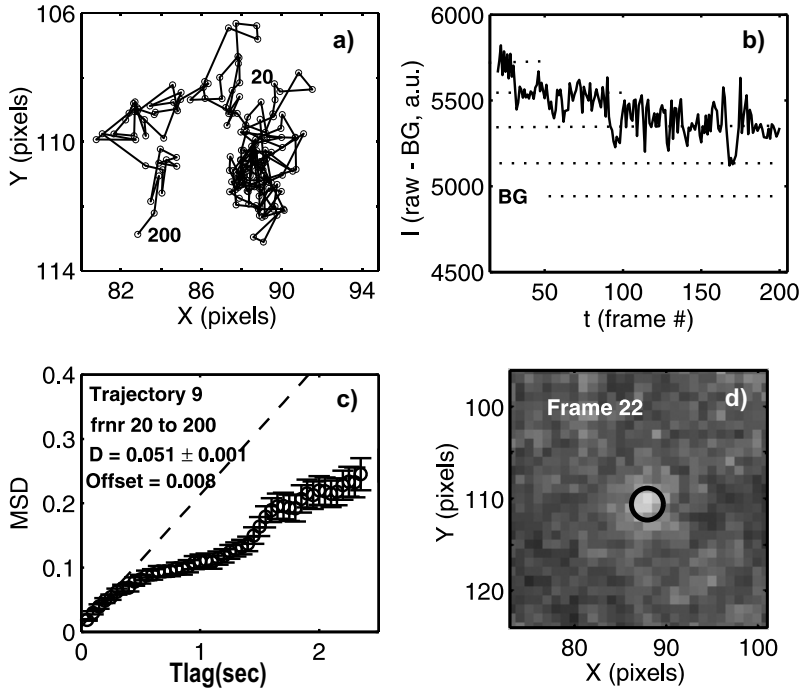

Figure 2.10. *Inspection panel of the tracking routine. The figure shows a representative trajectory of an LFA-1 nanocluster labeled with L16-Atto647N on the dorsal cell membrane of THP-1 cells. a) Trajectory in the x-y plane. b) The Intensity-time plot of the trajectory. c) MSD plot of the represented trajectory, linearly fitted through the first four points. d) Each individual traced spot is followed frame-by-frame in its local environment to allow visual inspection of generated trajectories.*

An estimation of the size of the immobile subpopulation has been made by scaling the distribution of D of immobile nanoclusters on fixed cells to the first bar ($D \leq 0.001\mu m^2$) in the histogram of the dataset of living cells (black envelope line). The area under the black envelope line was then estimated as the immobile subpopulation:

$$P_{imm} = \frac{N_{<0.001}}{R} \cdot \frac{100}{N_{total}} = 19.4 \pm 2.6\% \tag{2.13}$$

Where P_{imm} is the immobile subpopulation (% of all trajectories in dataset), N_{total} is the number of trajectories in the dataset and $N_{<0.001}$ is the fraction of N_{total} with $D < 0.001\mu m^2/s$. R is the ratio between immobile nanoclusters

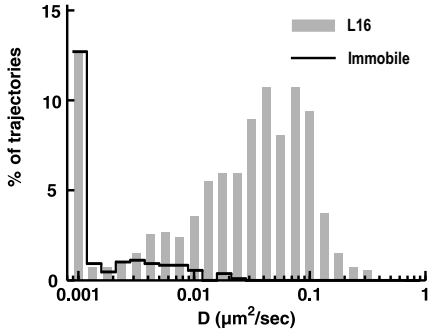

Figure 2.11. *The distribution of D of L16 labeled LFA-1 nanoclusters. The bins in the histogram are normalized to the total number of trajectories (669 from 49 cells). Minimum trajectory length: 13 frames. The black envelope line represents the estimated distribution of immobile nanoclusters.*

with $D < 0.001\mu m^2$ and all immobile nanoclusters. R has been obtained from the distribution of diffusion constants of immobile nanoclusters on fixed cells (see figure 2.8*b*, minimum trajectory length 13 frames). The errors in $N_{<0.001}$, N_{total} and the ratio R originate from Poisson errors in the numbers of trajectories and they propagate in the error ΔP_{imm} which has been estimated by linear approximation.

Since D at short time lags do not report on the long-term diffusion behavior, we applied cumulative probability distribution (CPD) analysis to enquire on the type of diffusion exhibited by the mobile fraction of LFA-1 ($D \geq D_{th}$) over a long time interval (1.5 s), see fig. 2.12. The CPD analysis has been described in detail in paragraph 2.2.4. In essence, with the CPD method different types of diffusion can be distinguished over an ensemble of individual trajectories with greater accuracy and robustness than time-dependent fitting of individual short-length trajectories [158]. The minimum trajectory length was set to 21 frames, resulting in a subset of 380 trajectories from 49 cells. D_{th} was set equal to $D_{min} = 2\sigma$ which equals $0.006\mu m^2/s$ for a minimum trajectory length of 21 frames. As a result, approximately 95% of all immobile trajectories fell below D_{th} and almost all (98%) mobile trajectories were part of the mobile fraction.

The CPD of square displacements could be best fitted using a two-component model [158]: the sum of squares of the residuals reduced from 15 to 0.17 (12627 points) with respect to a one-component model. This indicated that there were at least two dominant subpopulations present in the mobile fraction. Three

parameters were retrieved by the fitting: a fraction of slow-diffusing nanoclusters (f), a square displacement of this slow component and a square displacement of the fast-diffusing component. Eventually, square displacement curves were retrieved for both components (subpopulations) by fitting the CPD generated at different time lags. Square displacement plots of slow and fast mobile

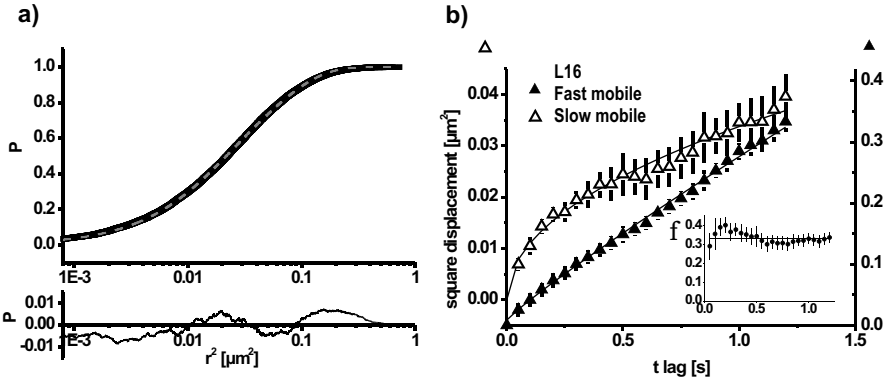

Figure 2.12. *The diffusive behavior of L16 labeled LFA-1 nanoclusters was accessed by CPD analysis. a) Semi-logarithmic representation of the CPD of the square displacements of all trajectories in the mobile fraction (time lag 3 frames). The CPD was fitted with a two-component function (dotted line). The lower plot represents the error in the fit. b) Square displacement plots of retrieved components. A slow (left y axis, open markers) and a fast (right y axis, closed markers) diffusing component were recovered and fitted with an anomalous diffusion function (lines). Goodness of the fit:* < 0.24. *Inset: the fraction f of slow diffusing nanoclusters.*

subpopulations were fitted with an anomalous diffusion representing function: $r(t)^2 = \Gamma \cdot t^\alpha + {\Delta_0}^2$ [131] (fig. 2.12b), where $r(t)^2$ is the square displacement at time lag t, Γ is the transport coefficient and ${\Delta_0}^2$ is the square displacement offset at $t = 0$. Parameter α is the anomalous parameter, values close to one signify random motion, while values below one give a measure of the degree to which the motion is restricted. The fast mobile subpopulation ($\Gamma = 0.067 \pm 0.001$) exhibited random diffusion since α is close to one ($\alpha = 0.91 \pm 0.02$), while the slow mobile subpopulation ($\Gamma = 0.009 \pm 0.001$) showed anomalous diffusion ($\alpha = 0.49 \pm 0.06$). Square displacement plots were fitted up to 24 frames with high confidence levels: the goodness of the fit was < 0.24.

Finally, we used the fraction $f = 0.33 \pm 0.03$ to derive the relative sizes of the slow and fast mobile subpopulations:

$$P_{slow} = (F_{mob} - 0.05 \cdot P_{imm}) \cdot f = 26.1 \pm 2.8\% \tag{2.14}$$

$$P_{fast} = (F_{mob} - 0.05 \cdot P_{imm}) \cdot (1 - f) = 52.9 \pm 3.9\% \tag{2.15}$$

Where P_{slow} and P_{fast} are the fast and the slow mobile subpopulation expressed in % of the total number of trajectories and F_{mob} is the percentage of trajectories in the mobile fraction. The errors have been estimated by linear approximation and originate from the standard deviations in the numbers of trajectories in the specified fractions of the histogram (Poisson noise) and the error in f.

The boundary D_{th} did cut off a small part of the shoulder in the mobile distribution. Strictly speaking, this mobile part overlapping with the immobile distribution has not been analyzed and can contain a distinctive mobility subpopulation. We named this part the 'unspecified' fraction of the total population($P_{unspecified}$):

$$P_{unspecified} = P_{total} - F_{mob} - (P_{immob} \cdot 0.95) = 1.6 \pm 3.4\% \tag{2.16}$$

Here, $P_{unspecified}$ can be interpreted as a continuation of the shoulder in the mobile part of the histogram (distribution of trajectory length ≥ 21, not shown). Therefore, we assume $P_{unspecified}$ as part of P_{slow} and both are taken together in the final calculation of P_{slow}, which becomes 27.7 ± 4.4.

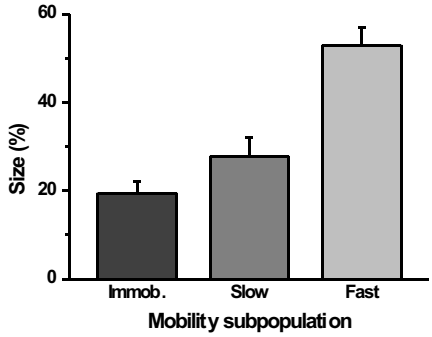

Figure 2.13. *The normalized fractions of the immobile, slow mobile and fast mobile subpopulations of L16 labeled LFA-1 nanoclusters expressed in % of the total number of trajectories. Error bars: standard deviation.*

The found percentages of the the immobile, slow and fast mobile populations are shown in fig. 2.13. A significant fraction (53%) of the L16 labeled LFA-1

nanoclusters on monocytes diffuse in a random fashion on the cell membrane, while approx. 28% show slow and anomalous diffusion. Finally, around 19% of the L16 trajectories are classified as being immobile.

2.4 Discussion

In this chapter we presented a method for imaging and tracing of heterogeneously distributed individual nanoclusters of transmembrane receptors on the cell membrane of living cells with single molecule detection sensitivity. We have developed a robust analysis method which is able to identify three subpopulations of different mobilities within a single dataset and which is capable to estimate their respective size and ensemble behavior.

We developed a straight-forward EPI/through-the-objective TIR fluorescence microscope capable of imaging integrin receptors on the cell membrane of living cells with single molecule detection sensitivity, high speed and precision. Typical position accuracies were 37nm for single molecules (Atto647N) and 47nm for L16-Atto647N labeled LFA-1 nanoclusters, both excited with 1 kW/cm^2 during an excitation time of 4 ms. These results are comparable to wide field microscope position accuracies described in the literature [177, 178]. A high efficiency dual-color detection scheme was implemented, with z-aberration adjustment, relatively little aberration and the ability to use standard-sized filters and dichroic mirrors. The combination of dual-color functionality and single molecule detection sensitivity of the microscope allows us to perform a colocalization study of the different LFA-1 conformations. In future studies, proximity dependent mobility can be studied for LFA-1 and plasma membrane associated molecules known to interact with LFA-1.

We modified colloidal particle tracking algorithms for tracing of fluorescently labeled diffraction limited spots in a heterogeneous packing density which show a wide range of mobility behavior. Cell areas with a high object density and areas with a high nonuniform background level were excluded until bleaching reduced the object density to acceptable levels. In addition, selection of specific areas and manual trajectory inspection improved tracking precision. Consequently, a much wider range of measured cells could be traced. Recently, new approaches have been demonstrated which optimize found trajectories in a spatio-temporal manner by minimizing the total trajectory length in an image stack [160, 161]. The colloidal particle tracking algorithm used here works on a frame-to-frame basis and can thus be improved by these approaches.

We developed an analysis method where single trajectory analysis and ensemble analysis techniques were combined to inquire on the wide range of mobility behavior within a single dataset. Single trajectory analysis was implemented to investigate the distribution of short time diffusion coefficients (D)

of probed objects. Detailed analysis of the distribution of D of immobile LFA-1 nanoclusters on fixed cells gave us the ability to separate and quantify the immobile subpopulation. An appropriate threshold value D_{th} was determined for the distribution of D to inquire on different modalities within the mobile fraction of trajectories with minimal interference from the immobile subpopulation. CPD analysis [158] was implemented to distinguish two subpopulations of different mobilities within the mobile fraction. By analysis of trajectories of L16 labeled LFA-1 nanoclusters on living monocytes, we demonstrated that our software is able to distinguish three subpopulations of different mobilities and estimate their respective size and ensemble behavior. Our results demonstrate that a combination of ensemble averaging [158, 178, 164] and single trajectory analysis [169, 62] is a powerful approach, capable of resolving detailed mobility information on subpopulations while taking the advantages of the SDT technique.

2.5 Conclusion

A toolbox has been developed to image, trace and analyze the mobility behavior of transmembrane receptor nanoclusters on living cells. An EPI-TIR fluorescence microscope with single molecule detection sensitivity has been implemented with a dual-color detection scheme, capable of imaging LFA-1 nanoclusters on the membrane of living monocytes with high speed and precision. Typical localization accuracies were $0.037\mu m$ for single molecules (Atto647N) and $0.047\mu m$ for L16-Atto647N labeled LFA-1 nanoclusters, both excited with 1 kW/cm^2 during an excitation time of 4 ms. Colloidal particle tracking algorithms have been successfully modified and implemented for semi-automatic tracing of individual LFA-1 nanoclusters that are in a heterogeneous packing density and have a wide range of mobility behavior. Furthermore, we have developed a robust and dedicated software to distinguish subpopulations of different mobilities and estimate their respective size and ensemble behavior, as has been demonstrated by analysis of trajectories of L16 labeled LFA-1 nanoclusters on living monocytes. The 'toolbox' presented in this chapter will be used throughout this thesis to investigate the dynamics of LFA-1 under different settings and cell systems.

Chapter 3

LFA-1 Nanocluster Mobility on THP-1 Monocytes

On resting blood derived monocytes LFA-1 is distributed in ligand independent pro-active and inactive nanoclusters on the cell membrane. However, the mobility characteristics of these pro-active and inactive nanoclusters and how cluster dynamics, affinity and valency interplay to regulate monocyte adhesion are yet unknown. We have applied single dye tracing to probe the mobility of individual LFA-1 nanoclusters on resting and ligated monocytes. We show that on resting cells 95% of the LFA-1 is mobile. We distinguished a slow and fast mobile subpopulation within this mobile fraction with both subpopulations diffusing in a considerably unhindered fashion. The minority of extended LFA-1 exhibits a distinct diffusion profile with cytoskeleton bound immobile, hindered slow-, and unhindered fast diffusion. Our results questions earlier models of cytoskeletal anchorage of the overall integrin receptor population on resting cells and support more complex models where only a subset of extended LFA-1 is bound to the cytoskeleton. Furthermore, when cells were brought into contact with ICAM-1 functionalized surfaces, extended LFA-1 was recruited to the binding site. Remarkably, the diffusion profile of extended LFA-1 was also altered at the unligated dorsal cell side, suggesting triggering of inside-out signalling pathways regulating overall LFA-1 affinity and consequently mobility.

3.1 Introduction

The lymphocyte function-associated antigen-1 (LFA-1, CD11a/CD18) is part of the leukocyte integrin subfamily: it shares a common β_2 (CD18) subunit with subfamily members and it has its own specific α_L (CD11a) subunit [78]. On leukocytes, LFA - 1 plays a key role in leukocyte arrest, crawling and transendothelial migration [13, 9–11] by binding to the intercellular adhesion molecules (ICAMs) [179]. It has been observed in-vivo that blood-borne lymphocytes can 'switch' within seconds from rolling to arrest [180].

This ability of leukocytes to 'switch' rapidly from a non-adhesive to an adhesive state has frequently been subject of interest, leading to many different and sometimes controversial perspectives on the adhesion regulation mechanisms of integrins [181, 26, 182, 31]. So far, three non-mutually-exclusive mechanisms have been proposed. First, LFA-1 can undergo conformational changes upon inside-out or outside-in signalling, leading to modulation of affinity for its ligand [48, 22–25, 4]. Second, adhesion can be regulated by redistribution of LFA-1 on the cell surface, leading to modulation of valency [30]. Re-distribution has been proposed as a primary mechanism of integrin activation [31, 29]. In this case, cytoskeletal restraints keep receptors in an inactive, non-clustered state and disruption of the actin cytoskeleton results in enhanced clustering and affinity of LFA-1 molecules, effectively activating adhesion [183, 184, 40, 185]. However, redistribution has also been proposed as a ligand binding induced assisting mechanism, where release of integrins from cytoskeletal constraints facilitates ligand-dependent mass-action-driven accumulation at the binding site [26]. Third, adhesion can be regulated by alteration of LFA - 1 mobility. It has been proposed that release of LFA-1 from cytoskeletal constraints and thereby enhancing its mobility, is an important early step in adhesion activation [34]. In this model, increased integrin mobility enhances integrin-ligand encounter probability and consequently, binding [32, 33].

Earlier redistribution and/or mobility based models of LFA - 1 regulation proposed that the molecule is confined to the cytoskeleton in resting cells and (transiently) released from its cytoskeletal constrains upon cell activation, resulting in increased mobility, clustering and/or affinity [183, 184, 40, 185]. However, recent work on T cells demonstrated a more complex mobility pattern of LFA-1 where different subsets of conformational states have distinct interactions with the cytoskeleton [28]. Variations among cell types in LFA-1 function are reflected in cell type dependent diffusion profiles of these subsets of conformational states. In line with this model are recent observations on monocyte-T-cell interactions, where it was shown that only the extended conformation of LFA-1 is recruited to the ligand binding site [3]. Moreover, TEM (transmission electron microscopy) observations revealed that on resting primary monocytes, LFA-1 is distributed in inactive (bent conformation) and pro-active (extended

conformation) LFA-1 nanoclusters prior to ligation. These observations suggest that affinity, valency and mobility regulation act in synergy to regulate LFA-1 mediated binding of monocytes. Until now, conformation-specific redistribution of LFA-1 on monocytes has only been studied on the microscale or in a static way: the underlying mobility mechanisms and the role of the cytoskeleton are yet to be defined.

This chapter focusses on the characterization of the mobility of the total versus the extended LFA-1 nanocluster population on monocytes. We applied the SDT (single dye tracing) approach in combination with conformer specific antibody labeling to map the mobility of individual LFA-1 nanoclusters. In line with recent tracking experiments on Jurkat T lymphocytes [28], we show that on resting monocytes a major fraction of LFA-1 is mobile. We combined individual trajectory and ensemble averaging analysis methods and distinguished a slow and a fast subpopulation within this mobile fraction, both showing considerably unhindered diffusion. On the other hand, the minority of extended LFA-1 revealed a distinctive diffusion profile with immobile, slow hindered and fast unhindered mobility subpopulations. Upon cytoskeleton disruption treatment, this immobile subpopulation of extended LFA-1 became slow mobile. Furthermore, we observed transient confinement in $9 \pm 3\%$ of the trajectories of extended LFA-1. Our results discard earlier models of cytoskeletal anchorage of the overall integrin receptor population on resting cells and support more complex models where only a subset of extended LFA-1 is transiently bound to the cytoskeleton [28, 167]. Finally, we investigated LFA-1 mobility of cells plated on ICAM-1-Fc functionalized surfaces. Surprisingly, extended LFA-1 is not only immobilized and recruited at the ligated ventral side, but its mobility profile is also altered at the dorsal side of the cell. These data suggest that ligation triggers inside-out signalling pathways regulating the overall balance between conformational states and consequently mobility.

3.2 Materials and Methods

Antibodies and antibody conjugates

Antibody conjugates TS2/4-AlexaFluor647, TS2/4-Atto520 and NKI-L16-Atto-647N were a gift from the Tumor Immunology Laboratory (NCMLS, the Netherlands). Both TS2/4 and NKI-L16 (further referenced as L16) are reactive with the alpha subunit of LFA-1 [3]. Activation reporter mAb L16 (IgG2a) was labeled by conjugation of fluorophores to the thiol-groups, the non-blocking mAb TS2/4 (IgG1) was labeled by conjugation of fluorophores to the amino groups. The labeling ratios of the antibody-fluorophore conjugates were as follows: $\sim$ 1:2 for TS2/4-AlexaFluor647, $\sim$ 1:0.3 for TS2/4-Atto520 and $\sim$ 1:0.8 for L16-Atto647N. The labeling ratio of TS2/4- AlexaFluor647 was determined

by analysis of single molecule intensity-time traces on individual antibodies on glass. The labeling ratios of TS2/4-Atto520 and L16-Atto647N conjugates have been determined by analysis of absorption spectra of antibody solutions. Unless stated otherwise, single color experiments were performed with either L16-Atto647N or TS2/4-AlexaFluor647 antibody fluorophore conjugates. Dual color experiments were performed with L16-Atto647N and TS2/4-Atto520. For co-grabbing, a goat-anti-mouse IgG-AlexaFluor488 antibody conjugate was used. The commercially available conjugates mIgG1κ-AlexaFluor647, mIgG1κ-PE and mIgG2α-APC were used as isotype controls. For the control measurements in the ligation experiments the following antibodies were used: Mouse-anti-Human ICAM-1 and Goat-anti-Mouse-AlexaFluor647.

Cell culture and sample preparation

Cell culture and sample preparation were performed according to the procedures described in chapter 2. Shortly, THP-1 monocytes (referenced as monocytes) were incubated on FN (Fibronectin) or PLL (Poly-L-Lysine) coated (chambered) cover glasses for 15 minutes. After removal of unbound cells, samples were blocked by a 15 min incubation with 1% Human Serum in RPMI. After blocking, samples were incubated with antibody conjugates in RPMI medium at a concentration of $2\mu g/ml$ (TS2/4-Atto520) and/or 0.2 $\mu g/ml$ (TS2/4-AlexaFluor647 and L16-Atto647N) for 3.5 minutes. RPMI without phenol red was used as an imaging medium. The measurement started 10 minutes after the beginning of the labeling step. All incubation steps were performed at 37 °C. When required, samples were fixed (2% PFA in PBS, filtered) before imaging.

Preparation of Cytochalasin-D treated samples

Samples were prepared in duplex; one sample was labeled with mAb L16 and the other sample was labeled with the appropriate isotype control. Approximately 10^5 cells were taken, rinsed in RPMI, re-suspended in 1ml RPMI + Cyto-D (Cytochalasin-D) except that Cyto-D or DMSO was added to all solutions used in all sample preparation steps. At the start of the measurement, samples had been incubated with Cyto-D for 1hr:17min.

Preparation of F-actin stained samples

Cyto-D-treated samples were prepared as described above up to the last rinsing step before labeling. After rinsing, samples were fixed (20 min. incubation, 2% PFA in PBS, filtered). Cyto-D treatment prior to fixation was 43 minutes. After fixation, samples were washed 3x (PBS). Cells were then permeabilized by a 5 minute incubation in a 0.5% TritonX 100 solution. Samples were washed

3x (PBS) and stored in a PBS + 1% BSA + 100mM azide solution for two and a half days. Samples were rinsed 3 times with PBS and stained with a 0.25μg/ml phalloidin-TRITC solution for 30 minutes at room temperature. Finally, samples were washed twice (PBS) and stored in mowiol.

Preparation of ICAM-1 coated surfaces

ICAM-1-Fc coated LabtekII chambered coverglasses (8 well) were prepared as follows: first, 100μl 10$\mu g/ml$ Goat-anti-Human Fc (Fab')$_2$ dissolved in TSM (20mM Tris, 150mM NaCl, 1mM $CaCl_2$, 2mM $MgCl_2$, pH 8.0.) was added per well and incubated for 1 hour at 37 °C. The substrates were rinsed three times with TSM. Substrates were then blocked for 30 minutes with 100μl/well 1% BSA containing TSM. After three times rinsing with TSM, substrates were incubated for 1 hour with 100μl/well 5$\mu g/ml$ ICAM-1-Fc dissolved in TSM. Finally, substrates were rinsed three times with TSM and once with RPMI just before use (within 24 hours after preparation). Immuno staining and fluorescence microscopy was used to verify functionality, specificity and uniformity of ICAM-1-Fc functionalized surfaces.

Co-grabbing experiment

After SDT measurements on multiple cells, co-grabbing antibodies were added at a concentration of 5 $\mu g/ml$. The measurement continued directly after addition to monitor co-grabbing effects on LFA-1 mobility.

Flow cytometry

THP-1 cells were rinsed, re-suspended in RPMI medium containing 2% human serum (Sigma-Aldrich, male AB+) and incubated for 30 min. at 37 °C. Until fixation, the rest of the procedure was carried out at 4 °C. The sample was split in X Eppendorf tubes each containing 1M of cells. Each tube was rinsed 3 times with the right buffer (RPMI or PBS + BSA). Between each washing step a waiting time of 5 minutes was implemented. Tubes were split in the final number of samples needed and cells were re-suspended in 50μl buffer. L16-Atto647N and isotype control mIgG2α^{APC} conjugates diluted in the right buffer were added to reach a final labeling concentration of 10$\mu g/ml$ in 100μl/well. Samples were incubated for 30 minutes. Finally, samples were washed two times with the appropriate buffer before overnight fixation in 2% PFA containing PBS. Samples were analyzed by immunofluorescence flow cytometry (Beckman & Coulter).

Cellular Imaging

The experiments were performed on a home-made dual-color excitation / emission combined EPI-TIR (Total Internal Reflection) fluorescence microscope as

described in chapter 2. Briefly, samples were excited with one or two gated laser excitation sources. For each frame, the pulse length and power density were set to 4ms, ∼1kW/cm^2 for the 633nm HeNe laser and 2ms, ∼2kW/cm^2 for the 514.5nm line of an Ar^+Kr^+ laser. Fluorescence was collected with a 60x TIRFM objective (Olympus, PLAPO 60X0TIRFM 1.45 NA) and separated into two channels by a home-built emission path. Both images were projected onto a different area of an Intensified CCD camera (Princeton Instruments, I-Pentamax, genIV photo cathode). Single color experiments were performed at 20Hz (L16-Atto647N) or 10Hz (TS2/4-AlexaFluor647). Dual color experiments (L16-Atto647N and TS2/4-Atto520) were performed at 20Hz. Detection efficiencies of the different antibody-fluorophore conjugates varied from 5-7% under our experimental conditions. Typical position accuracies were $0.037\mu m$ for single Atto647N molecules on glass. Position accuracies of LFA-1 nanoclusters on THP-1 cells varied between 0.047 μm (L16-Atto647N or TS2/4-Atto520 labeled fixed cells) and 0.055 μm (TS2/4-AlexaFluor647 labeled cells). Experiments were performed at 37 °C. Measurement at the dorsal side of the cell: DIC (Differential Interference Contrast) enhanced bright field imaging was used to select stretched cells, which were imaged above the nucleus, to avoid detection of autofluorescence from the cytosol. Through the objective type TIR excitation was used to image the ventral cell membrane. To switch to TIR excitation, the excitation beam was translated in the back focal plane until the image of the dorsal membrane of a cell disappeared. Then, the ventral membrane was brought into focus.

Single Dye Tracing and analysis of square displacements

SDT techniques and analysis of square displacements have been described in chapter 2. Briefly, two dimensional trajectories in the plane of focus were reconstructed by the aid of colloidal particle tracking software [171], which has been modified and implemented for tracing of fluorescently marked individual nanoclusters on living cells. MSD (mean square displacement) curves were generated for every single trajectory with a minimum length of 13 frames. The short timelag diffusion coefficient D was retrieved by linear fitting (first 3 or 4 points of the MSD plot for a trajectory length of ≥13 or ≥21 frames respectively). Finally, a semi-logarithmic histogram of D for individual LFA-1 nanoclusters was generated.

CPD (Cumulative Probability Distribution) analysis [158] was further used to identify and characterize different mobility subpopulations within the mobile fraction of the trajectories ($D \geq D_{th}$). For CPD analysis, trajectories ≥ 21 frames were selected, resulting in $D_{th} = 0.006\mu m^2/s$ (see 2.3). One or two components were identified in the mobile fraction and their square displacement curves were retrieved. Fit parameter f corresponds to the slow diffusing part of the mobile fraction (in case 2 components were identified). Square displacement

curves were fitted with an anomalous diffusion representing function: $r(t)^2 = \Gamma \cdot t^{\alpha} + {\Delta_0}^2$ [131], where $r(t)^2$ is the square displacement of the component in question at time lag t, Γ is the transport coefficient, α is the anomalous parameter and ${\Delta_0}^2$ is the square displacement offset at $t = 0$. In addition, square displacement curves were also fitted with a linear function through the first four points to obtain the short timelag diffusion coefficient (D) of the retrieved components. The component with the lowest D was defined as the 'slow' mobile subpopulation and the other component was defined as the 'fast' mobile subpopulation.

Finally, the immobile, slow and fast mobility subpopulations were quantified (% of the total number of trajectories). For that, the immobile subpopulation has been estimated by scaling the histogram of D of immobile nanoclusters on fixed cells to the first bar ($D < 0.001 \mu m^2$) in the histogram of the experimental dataset. Then, the average of the fit parameter f was used to determine the percentages of the slow and fast mobile subpopulations. Error bars represent the approximated standard deviation of the mobility subpopulation in question. Significance levels were derived using the single sided two-sample z-test.

Single trajectory transient confinement detection

A software dedicated to the detection of transient confinement was written according to the method described by Simson et al. [133]. Shortly, a trajectory is classified as 'transiently confined' if it contains periods in which the probe remains in a specific membrane area considerably longer than a Brownian diffusant would stay in an equally sized region. During screening, a confinement probability level L is calculated for every time point over a moving time interval (bin size S) within the trajectory. Noise within L at time point t was reduced by averaging over bin sizes ranging from S_{min} to S_{max}. If a randomly diffusing protein becomes trapped for a sufficient number of frames, the calculated confinement probability level L will raise above a defined threshold level L_c for a duration longer than the defined threshold time t_c. In this case, the trajectory is classified as transiently confined. Trajectories with a minimum length of 61 were screened by the algorithm. We optimized S_{min} and S_{max} to have sufficient transient confinement detection sensitivity and found 10 and 14 frames respectively. Depending on S_{min} and S_{max} and depending on the chosen values for L_c and t_c, a certain percentage of trajectories will be classified as transient confined in a false-positive manner. We analyzed simulated movies containing random diffusing trajectories and found the combination $L_c = 1.5$ and $t_c = 1$ frame (0.05s) corresponding to $1 \pm 0.5\%$ false-positively classified trajectories. Our simulated movies contained trajectories with a distribution of diffusion constants comparable to our measured data and the average trajectory length was approximately 200 frames. Since the majority of the measured trajectories had a shorter trajectory length compared to the simulations, the probability

to detect a false-positive transiently confined trajectory is lower for these trajectories than the estimated percentage, which forms an upper boundary.

3.3 Results

3.3.1 Optimization of direct antibody labeling on monocytes.

We tested and optimized labeling concentrations for our used TS2/4 and L16 antibody-fluorophore conjugates. First, the antibody conjugate L16-Atto647N was tested for functionality by immunofluorescence flow cytometry analysis. The mAb L16 labels the extended fraction of LFA-1 and its expression is dependent on the extracellular Ca^{2+} level [39, 24]. In order to test the functionality of L16-Atto647N, cells labeled with the conjugate were measured under high and low extracellular Ca^{2+} conditions. Representative results from one out of four experiments are presented in figure 3.1. In all four experiments, the mean fluorescence intensity of L16 labeled cells at high Ca^{2+} and Mg^{2+} concentrations was clearly shifted to higher intensity values compared to the intensity of the isotype controls and we observed the expected Ca^{2+}-dependent mean intensity. Thus, the L16-Atto647N conjugate labels specifically and is well detectable by flow cytometry.

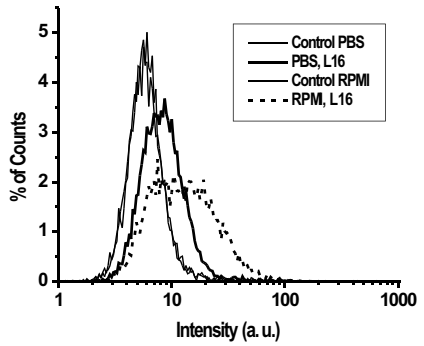

Figure 3.1. *The expression level of the LFA-1 L16 epitope subpopulation on THP-1 cells has been assessed by immunofluorescence flow cytometry analysis. Cells were incubated, labeled and measured in PBS (0mM Ca^{2+}) versus RPMI (0.4mM Ca^{2+}, Mg^{2+}) in order to compare epitope expression at different cation levels. The following median intensity values (a.u.) have been found for the analyzed samples: PBS: 7.8, isotype control: 5.6, RPMI: 12, isotype control: 5.6.*

Second, titration experiments have been performed to optimize the labeling

concentrations for SDT experiments. The labeling concentrations were optimized with respect to signal-to-background level: for TS2/4- AlexaFluor647 and L16-Atto647N conjugates, a concentration in the order of 0.1 $\mu g/ml$ resulted in an optimal signal to background ratio. For the TS2/4-Atto520 conjugate, the optimal labeling concentration was in the order of 1 $\mu g/ml$. The differences in optimal concentration can be explained by the different antibody / fluorophore ratios. Furthermore, differences in antibody affinity and fluorophore stability might also play a role. Due to the heterogeneous level of expression of LFA-1 on THP-1 cells, it was not possible to optimize the antibody concentration for an optimal spot density.

3.3.2 Single Dye Tracing of individual LFA-1 nanoclusters

To gain insight into the dynamics of LFA-1 nanoclusters on resting monocytes, we applied SDT to study the mobility behavior of the total LFA-1 nanocluster population. A representative experiment is shown in figure 3.2. monocytes were plated on PLL or FN coated coverglasses, labeled with mAb TS2/4 and fluorescently imaged on the dorsal membrane at a frame rate of 10 Hz. Due to the sublabeling procedure, only a fraction of the LFA-1 molecules has been labeled and single molecule bleaching steps can be observed in intensity-time traces of labeled nanoclusters (par. 2.3.2). On average, samples were imaged for 25 min and approximately 10 cells were investigated per experiment. Movies suitable for SDT were selected and trajectories were reconstructed (fig. 3.2*b*). Individual trajectories were analyzed by MSD analysis and the short time lag diffusion coefficient (D) was derived (see 3.2*c*). Different types of diffusion behavior, ranging from confined or immobile to random diffusion are already apparent from fig. 3.2*d*.

It has been shown that LFA-1 molecules are primarily organized in randomly distributed nanoclusters on the cell membrane of resting monocytes [3]. Similar results were found for monocytes: high resolution microscopy and simulations showed that at least 60% of the LFA-1 is nanoclustered [77]. Therefore, the observed heterogeneous diffusion behavior can be mainly addressed to LFA-1 nanoclusters.

3.3.3 Effect of the substrate on the mobility of LFA-1 nanoclusters

To understand the role of the substrate in LFA-1 mobility, we investigated TS2/4 labeled LFA-1 nanocluster mobility on the dorsal versus the ventral

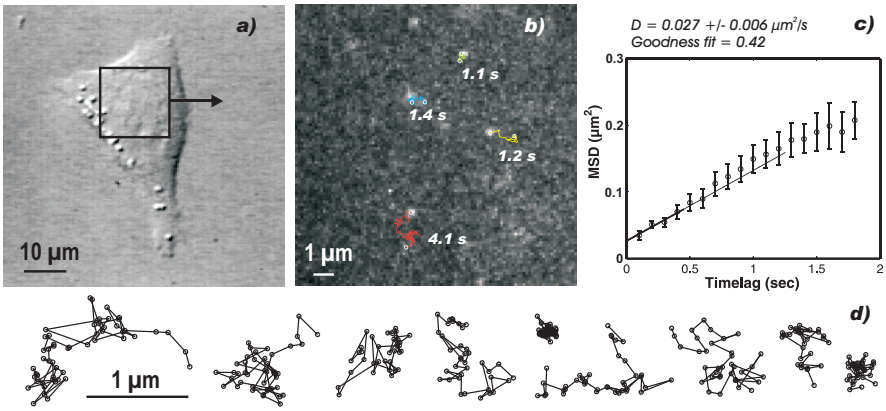

Figure 3.2. *Tracing fluorescently labeled LFA-1 nanoclusters on the dorsal side of living monocytes. (a) THP-1 stretched on a FN-coated surface. (b) Representative frame illustrating the fluorescent signal of labeled LFA-1 nanoclusters made at the position of the inset in figure a. The nanocluster positions are determined with sub-100nm accuracy and linked together into trajectories. (c) MSD vs. time lag plot of a representative LFA-1 trajectory. The first four MSD points were fitted with a linear function and D was derived. (d) Representative trajectories of TS2/4-AlexaFluor647 labeled LFA-1 nanoclusters.*

side[1] of the cell (see fig. 3.3). The distribution of diffusion constants of individual nanoclusters on the dorsal cell side (histogram bars) and the ventral cell side (dotted line) have been compared. We observed a relatively broader distribution and a significant increase of trajectories exhibiting $D < 0.001 \mu m^2$ on the ventral side of the cells. An explanation can be found in extra hindrance experienced by nanoclusters on the ventral side. Hindrance may have its origin in immobile, FN-bound β_1 integrins and additional cytoskeletal structures which are involved in cell support at the adhesion sites. To avoid any potential artifacts due to the substrate, we chose to concentrate on the mobility at the dorsal cell membrane.

Furthermore, we also investigated LFA-1 mobility of cells plated on two different types of substrate; PLL and FN. Cells were plated on both substrates and labeled with TS2/4. We found no significant differences between the distributions of diffusion constants of PLL (black envelope line) and FN plated

[1]For study of mobility on the ventral side of the cells, data of two different type of measurements were combined in order to gain sufficient statistics: in one measurement cells were labeled with TS2/4-AlexaFluor647 and measured in EPI excitation mode at a frame rate of 10Hz, in the other measurement cells were labeled with TS2/4-Atto520 and measured in TIR excitation mode at a frame rate of 20Hz.

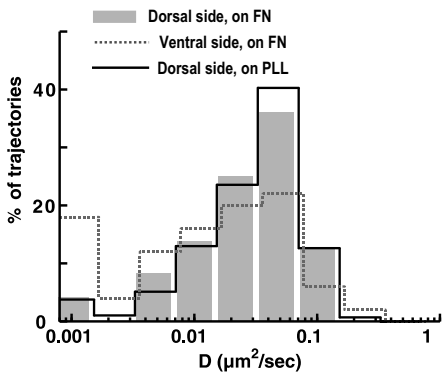

Figure 3.3. *Effect of the substrate on TS2/4 labeled LFA-1 nanocluster mobility. Distributions of diffusion constants were retrieved from nanocluster trajectories on the dorsal side (bars, 72 trajectories) and on the ventral side of FN plated cells (grey dotted envelope line, 50 trajectories). Furthermore, a distribution has been made of nanocluster trajectories measured on the dorsal side of cells plated on a PLL coated surface (black envelope line, 293 trajectories). The bins are normalized to the number of trajectories in the dataset.*

cells (bars). We conclude that the influence of PLL and FN coated surfaces on TS2/4 epitope LFA-1 mobility is negligible when mobility of LFA-1 is probed at the dorsal side of the cells. On the other hand, cells adhere in a more physiological, active manner to FN [186–188] than to PLL [189] coated surfaces. Although the first part of TS2/4 labeled cell experiments were performed on PLL plated cells, we chose to continue further experiments using FN coated surfaces for cell stretching. Besides the more physiological conditions, FN coated surfaces also gave us an additional control for cell viability. Experiments were only performed as long as cells remained well stretched on the FN substrate.

3.3.4 LFA-1 nanoclusters are primarily mobile on resting monocytes

We generated large datasets of trajectories from TS2/4 labeled cells to obtain a detailed profile of the mobility of LFA-1 nanoclusters on resting monocytes. The MSD of every individual trajectory was generated to obtain the distribution of D, see fig. 3.4a. We observed a broad, predominantly mobile distribution of diffusion constants over more than one order of magnitude. Strikingly, our data reveals that the majority of the LFA-1 on resting monocytes is mobile: only a minority of the nanodomains ($\sim 5\%$) were found in the immobile subpopulation (see black envelope line). These results are in contrast with earlier

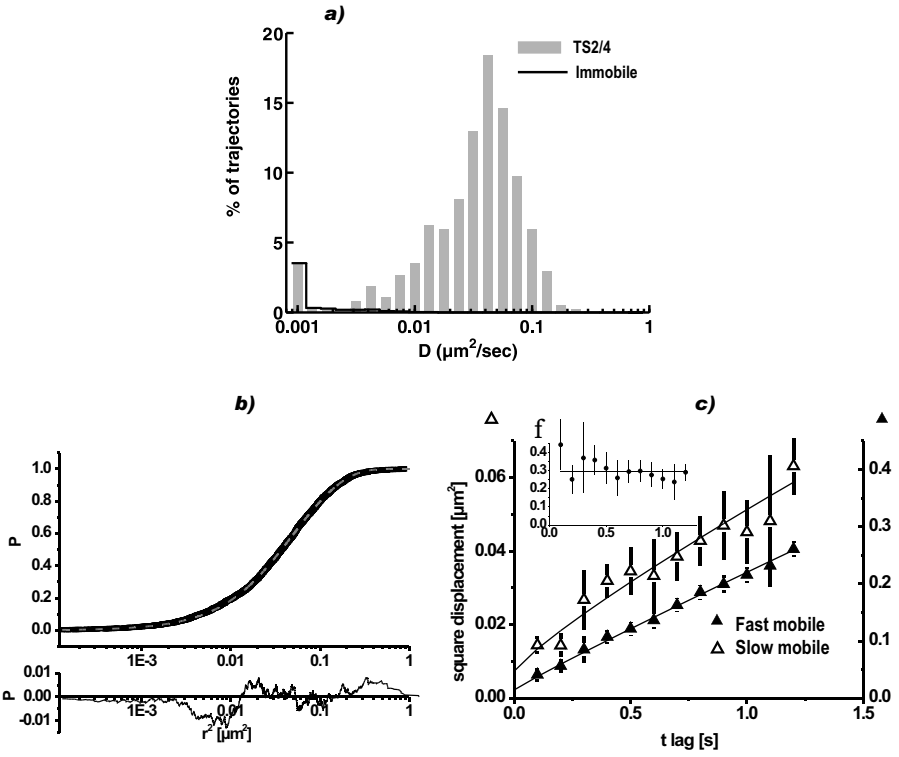

Figure 3.4. *The diffusive behavior of TS2/4 labeled LFA-1 nanoclusters on resting monocytes has been characterized using single trajectory and CPD analysis. (a) The distribution of short time lag diffusion constants of individual trajectories (369 trajectories from 128 cells). The black envelope represents the estimated distribution of immobile nanoclusters. (b,c) The diffusive behavior of the mobile fraction of LFA-1 nanoclusters (158 from 96 cells) has been characterized using CPD analysis. (b) CPD of square displacements, fitted with a function representing two diffusing components. The lower plot represents the error in the fit. (c) Obtained square displacement plots of slow mobile (left y-axis, open triangles) and fast mobile (right y-axis, closed triangles) subpopulations, fitted with an anomalous diffusion representing function. The fit parameters are presented in table 3.1. Fits were performed on 12 points. An average slow mobile fraction of the mobile trajectories* $f = 0.30 \pm 0.05$ *was found (line in inset). Error bars:* $2 \cdot \sigma$.

SPT studies on lymphocytes, where β_2 integrins were found to be immobile on resting lymphocytes [34, 183, 184]. On the other hand, a more recent SPT study also showed a significant mobile LFA-1 subpopulation on resting Jurkat

T cells [28].

Since the distribution of D does not report on long term diffusion behavior, we applied CPD analysis to study the mobile fraction of our trajectories over a longer time interval (typically 1.2s). Although the CPD analysis is an ensemble averaging method, it can isolate two mobility subpopulations from one dataset, while maintaining precision at longer time lags [158] (see materials and methods, par 3.2). We fitted the CPD of the mobile fraction of TS2/4 with functions representing one and two random diffusing components. The error in the fit reduced strongly when the CPD was fitted with a two-component function: the sum of squares of the residuals reduced from 1.9 to 0.07 (3411 points), indicating that there are at least two dominant subpopulations present in the mobile fraction (fig. 3.4*b*). Using the two-component fit functions, we generated square displacement curves for the 'slow' and 'fast' mobile subpopulations (fig. 3.4*c*). In addition, the fraction of slow mobile nanoclusters (f) was also obtained. Square displacement curves were fitted with both anomalous and linear diffusion fit functions as described in materials and methods. The anomalous diffusion exponent α is used to classify the type of diffusion [131]; $\alpha < 1$ is indicative for anomalous diffusion, $\alpha = 1$ represents random diffusion and $\alpha > 1$ is suggests a directional component within the diffusion. The results are presented in table 3.1.

The obtained D_{slow} and D_{fast} correlate with the peaks in the previously obtained distribution of D of individual nanoclusters, indicating that the CPD approach is consistent with the single trajectory analysis. The majority of LFA-1 nanoclusters is contained in the fast mobile subpopulation and its diffusion can be considered as Brownian ($\alpha_{fast} = 0.94 \pm 0.06$). Also the minority of slow mobile nanoclusters seem to diffuse in an unhindered fashion ($\alpha_{slow} = 0.86 \pm 0.2$). Altogether, these results show that resting monocytes contain an immobile, slow mobile and fast mobile subpopulation of LFA-1 nanoclusters. These nanoclusters are predominantly mobile (95%) and moving in an unhindered fashion.

3.3.5 Extended LFA-1 reveals a distinctive diffusion profile

Although it has been documented that on resting cells integrins are predominantly in a "bent", inactive configuration [190], we previously showed that on resting monocytes ∼25% of the LFA-1 nanoclusters are in an extended state prior to ligation [3]. Interestingly, it has been shown that this "primed" fraction of LFA-1 nanoclusters on resting monocytes is an important prerequisite for cell binding [3]. However, its mobility has not been investigated yet. Here we characterize the mobility of the extended LFA-1 fraction on resting monocytes by labeling with activation reporter mAb L16 [39, 24] and compare obtained results with the mobility of the total LFA-1 population.

To inquire on the mobility of extended LFA-1, we generated 669 individual

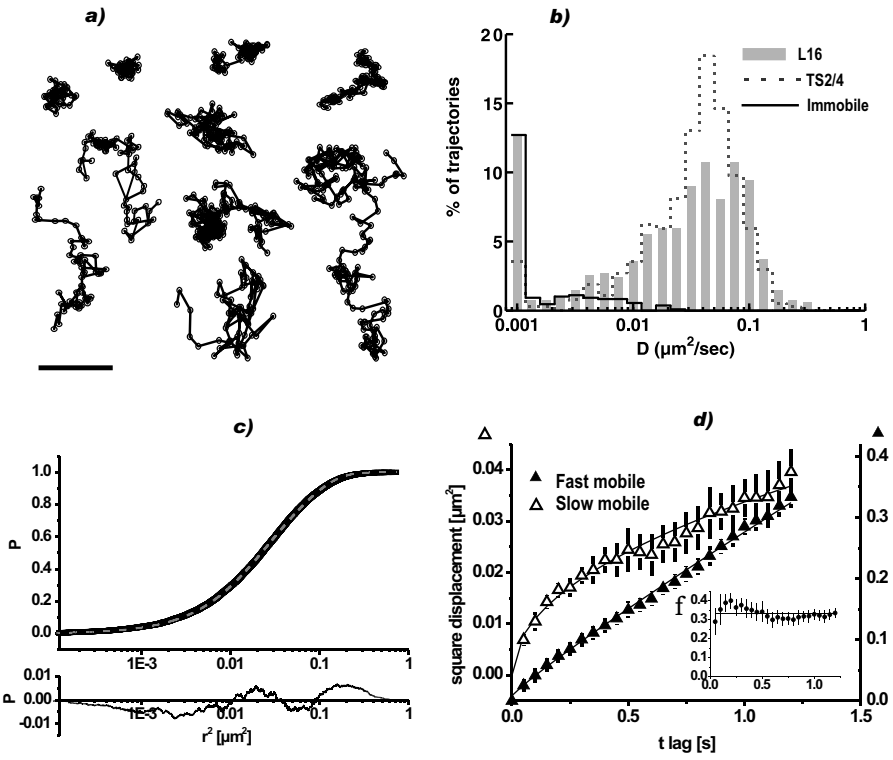

Figure 3.5. *Analysis of L16$^+$ LFA-1 nanocluster trajectories on resting monocytes. (a) Representative L16 trajectories. Scale bar: 1μm.(b) The distribution of short time lag diffusion constants of individual trajectories (669 trajectories from 49 cells). The black envelope represents the estimated distribution of immobile nanoclusters. (c,d) The diffusive behavior of the mobile fraction (380 trajectories from 49 cells) has been characterized using the CPD analysis. (c) CPD of square displacements, fitted with a function representing two diffusing components. The lower plot represents the error in the fit. (d) Obtained square displacement plots of slow mobile (left y-axis, open triangles) and fast mobile (right y-axis, closed triangles) subpopulations, fitted with an anomalous diffusion representing function. The fit parameters are presented in table 3.1. Fits were performed on 24 points. An average slow mobile fraction $f = 0.33 \pm 0.03$ was found (line in inset). Error bars: $2 \cdot \sigma$.*

trajectories from 49 L16-labeled resting monocytes. Representative trajectories are shown in fig. 3.5a, together with the distribution of D in fig. 3.5b. Compared to the distribution of D of the total LFA-1 population (labeled with TS2/4,

dotted line), L16 displays a larger immobile subpopulation (area under black line) and a reduced peak in the mobile fraction. We quantified the immobile subpopulations and found ∼19% and ∼5% for L16 and TS2/4 labeled cells respectively (fig. 3.6). Noteworthy, the diffusion constants of the L16 epitope are distributed over the same range as the total LFA-1 population. Therefore, the extended fraction of LFA-1 is not contained in one mobility subpopulation of the total LFA-1 population but rather distributed over all three mobility subpopulations.

$< r^2 >= \Gamma t^{\alpha} + \Delta_0$	α_{slow}	α_{fast}	f
TS2/4	0.86 ± 0.2	0.94 ± 0.06	0.30 ± 0.05
L16	0.49 ± 0.06	0.91 ± 0.02	0.33 ± 0.03

$< r^2 >= 4Dt + \Delta_0$	D_{slow} $[\mu m^2/s]$	D_{fast} $[\mu m^2/s]$	pnts
TS2/4	0.014 ± 0.005	0.056 ± 0.006	3411
L16	0.017 ± 0.001	0.081 ± 0.001	12627

Table 3.1. *The mobile fractions of TS2/4 and L16 epitope subpopulations have been analyzed by means of the CPD method (see figure 3.5). Found square displacement plots were fitted with an anomalous or a Brownian diffusion model. Fit parameters related to the slow mobile subpopulation are tagged with the subscript 'slow' and fit parameters related to the fast mobile subpopulation are tagged with the subscript 'fast'. The fit parameters D (short timelag diffusion coefficient) and α (anomalous factor) were retrieved. Furthermore, fraction f and the number of points of the CPD (at a time lag of 3 frames) are presented. The χ^2_{red} values of the fit functions were < 1.22 for TS2/4 and < 0.24 for L16 square displacement curves.*

We applied CPD analysis to study the distribution of mobile trajectories over mobility subpopulations and to inquire on the long term diffusion behavior of L16 labeled LFA-1 nanoclusters (fig. 3.5 and table 3.1). Also here, the CPD was best fitted using a two-component model (the sum of the squares of residuals reduced from 15 to 0.17). The fast mobile subpopulation of L16 labeled cells reveals similar Brownian diffusion compared to TS2/4 labeled cells. In contrast, the slow mobile subpopulation of the L16 epitope reveals more anomalous (hindered) diffusion compared to the TS2/4 epitope (L16: $\alpha_{slow} = 0.49 \pm 0.06$, TS2/4: $\alpha_{slow} = 0.9 \pm 0.2$). In addition, the percentage of nanoclusters revealing Brownian motion is reduced with respect to TS2/4 labeled cells (L16: $53 \pm 4\%$ fast vs. TS2/4: $32 \pm 6\%$ slow + $64 \pm 7\%$ fast, see fig. 3.6). Altogether, these results show that nanoclusters containing extended LFA-1 reveal a distinctive mobility profile compared to the overall LFA-1 nanocluster population. Although the distribution over immobile, slow and fast mobile subpopulations prevailed, the L16 epitope reveals anomalous diffusion in one of the mobility subpopulations and a decreased mobility compared to

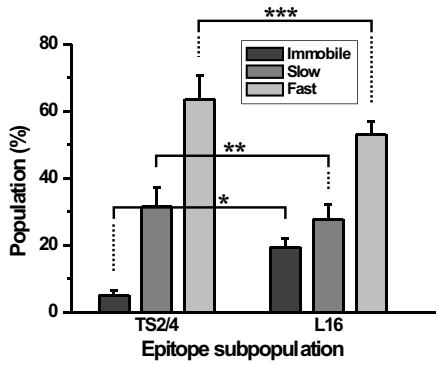

Figure 3.6. *The sizes of the immobile, slow mobile and fast mobile subpopulations for the TS2/4 and L16 epitopes normalized to the total number of trajectories. Error bars:* $1 \cdot \sigma$. $*$ $p < 0.0003$, $**$ $p = 0.3$ *and* $***$ $p = 0.095$.

the TS2/4 epitope.

3.3.6 A fraction of the extended LFA-1 nanoclusters is anchored to the actin cytoskeleton

In the previous section we showed that the minority of L16 positive LFA-1 nanoclusters revealed a reduced mobility with respect to the overall nanocluster population. These results prompted us to investigate the role of the cytoskeleton in mobility regulation of this conformational subset of LFA-1. We disrupted the actin cytoskeleton organization by Cyto-D (Cytochalasin-D) treatment and compared found results with those of untreated cells. In order to find an optimal concentration of Cyto-D, we tested cell viability versus disruption of cytoskeletal structures at different concentrations of Cyto-D. Treatment with RPMI + 0, 0.1, 1 or $5\mu g/ml$ Cyto-D was initiated prior to cell stretching and lasted for 43 minutes prior to fixation and actin staining. After bright field microscopy and confocal inspection, an optimal concentration of $1\mu g/ml$ was found. Upon Cyto-D treatment, cells became more round and the organization of actin was disturbed, see figure 3.7a.

To study the role of the actin cytoskeleton in LFA-1 nanocluster dynamics on resting cells, we probed LFA-1 mobility upon cytoskeleton disruption treatment. In figure 3.7b the distribution of diffusion constants and a quantification of the immobile subpopulation (inset) is presented. The results show a reduction of approximately 50% of the immobile subpopulation and an increase of the percentage of trajectories with a diffusion constant around $0.005\mu m^2/s$. Above this value, no differences in the diffusion of LFA-1 nanoclusters were observed

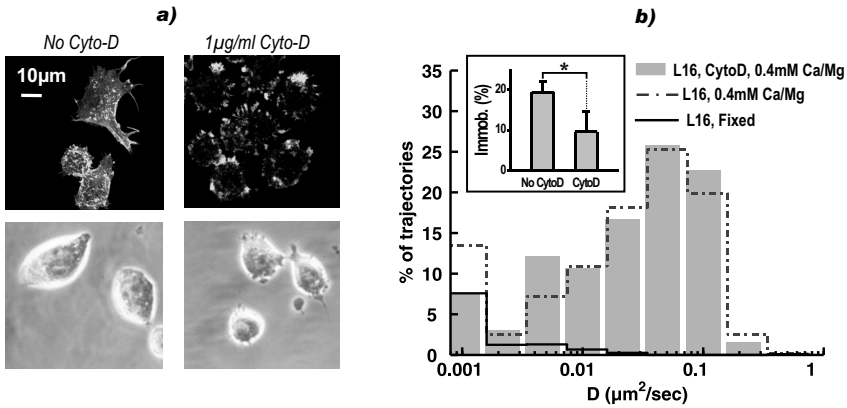

Figure 3.7. *The effect of cytoskeleton disruption treatment upon THP-1 cell morphology, the actin cytoskeleton and LFA-1 nanocluster mobility. a) Phalloidin-TRITC stained cells were imaged with phase contrast enhanced brightfield microscopy and confocal microscopy after Cyto-D treatment. b) The effect of cytoskeleton disruption treatment upon the mobility of L16 labeled LFA-1 on resting monocytes. The distributions of diffusion coefficients of treated (bars, 66 trajectories) and untreated (dotted line, 669 trajectories) cells are displayed. The black envelope represents the estimated distribution of immobile nanoclusters. Inset: quantification of immobile subpopulations.*$* p < 0.04$

as compared to the untreated cells. Our results show that part of the extended LFA-1 on resting monocytes is anchored to the actin cytoskeleton, which is in line with recent SPT work on Jurkat T cells [28].

3.3.7 Transient confinement in L16 epitope subpopulation.

Transient confinement might be one of the possible explanations for the anomalous diffusion found in part of the trajectories of L16 positive LFA-1 nanoclusters. Visual inspection of L16 positive LFA-1 nanocluster trajectories indeed suggested that transient confinement might be present. Therefore, we screened trajectories with a minimum length of 61 frames with a software dedicated to the detection of transient confinement, which was written according to the method described by Simson et al. [133].

Shortly, a trajectory is classified as 'transiently confined' if it contains periods in which the probe remains in a specific membrane area considerably longer than a Brownian diffusant would stay in an equally sized region. If a randomly diffusing protein becomes trapped for a sufficient number of frames, the calculated confinement probability level L will raise above a defined threshold level

L_c for a duration longer than the defined threshold time t_c. In this case, the trajectory is classified as transiently confined.

Figure 3.8*a* shows a representative trajectory which has been classified as transiently confined. Although no confinement can be deduced from the MSD plot of the trajectory (fig. 3.8b), the confinement probability level L crosses critical level L_c during the second half of the trajectory, indicating the presence of transient confinement (fig. 3.8c). Results from measured trajectories were compared to results from simulated random diffusing trajectories. $9 \pm 3\%$ of the trajectories were classified as transiently confined, while in the dataset of simulated trajectories with similar diffusion constants and random diffusing trajectories, only $1 \pm 0.5\%$ of the trajectories were classified as transient confined. This demonstrates that a subset of L16 positive trajectories shows transient confinement.

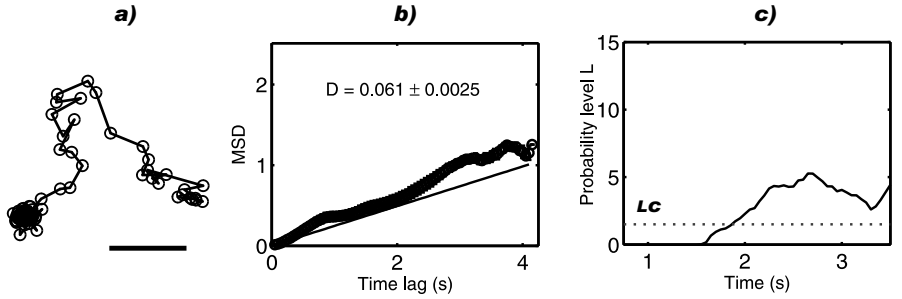

Figure 3.8. *Inspection pane for the detection of transient confinement. a) A typical trajectory classified as transient confined. Bar: 0.5μm. b) The MSD plot of the trajectory in a. c) Confinement probability level L_c as a function of time. Dotted line: critical confinement probability level $L_c = 1.5$.*

Since trajectory length, localization accuracy and frame rate are finite, only part of the spectrum of transient confinement periods can be detected [71, 154]. Therefore, the percentage of transient confined trajectories is probably underestimated. We estimated the minimum detectable residence time of a cluster in a confinement zone according to the work of Meilhac et al. [155]. By assuming that the undetected short-term fast diffusion coefficient within the confinement area was equal to the diffusion coefficient D outside the confinement area of the trajectory, we found that a confinement period should last for at least $2.1s$ or 42 frames in order to be detected. Therefore, the detected transient confinement might form the top of the iceberg of a broad scala of transient confinement periods, which might in general be much shorter in time.

Altogether, we can conclude that on THP-1 cells, the L16 epitope subpopulation contains *at least* $9 \pm 3\%$ transient confined trajectories.

3.3.8 ICAM-1 functionalized surfaces alter LFA-1 mobility on ventral and dorsal side of the cell membrane.

In the previous results, LFA-1 nanocluster mobility has been studied on resting monocytes labeled and measured in RPMI conditions. It has been previously reported that LFA-1 couples to the cytoskeleton upon ICAM-1 ligation [79, 176]. To achieve such a 'cytoskeleton-enhanced' strengthening of the LFA-1-ICAM-1 bonds, LFA-1 mediated signalling is essential and interaction between LFA-1 cytoplasmatic tails and regulatory proteins like talin and cytohesin-1 must take place [191–193]. However, it is unknown if such an outside-in signalling process is only locally affecting LFA-1 at the LFA-1-ICAM-1 binding site, or if it is affecting all active LFA-1 molecules at cell membrane by means of triggering inside-out signalling. Therefore, we not only investigated LFA-1 mobility at the ICAM-1 binding site, but also at the dorsal side of the cells where no ICAM-1 was present.

Except for the use of ICAM-1-Fc functionalized surfaces and a shorter cell stretching incubation time of 10 minutes, samples were prepared following similar procedures as FN plated cells. LFA-1 mobility at the binding site was probed using TIR fluorescence microscopy and LFA-1 mobility at the dorsal side was probed using EPI fluorescence microscopy. Cells were double labeled with TS2/4 and L16 antibodies and imaged in dual color mode, to facilitate collection of large amount of data.

Figure 3.9 shows how L16 epitope subpopulation nanocluster mobility on the dorsal cell side of THP-1 cells is altered by plating cells on ICAM-1 coated surfaces. Surprisingly, upon ICAM-1 ligation the distribution of D of individual trajectories in the dataset (bars) was shifted with respect to FN plated cells (dotted line) towards smaller D values. . At the same time, the immobile subpopulation (black line) increased with respect to FN plated cells (fig. 3.9*a*). We quantified the mobility subpopulation sizes and compared them with the quantities found for L16 labeled, FN plated cells to show the significance of the observed shift in the histogram (fig. 3.9*b*). The fast subpopulation of the mobile fraction decreased at the benefit of the immobile population (see significance level $*$ and $**$ in figure caption), while the slow subpopulation remained unaltered. The mobility subpopulations in the mobile fraction were characterized by means of CPD analysis, see fig. 3.9*c* and *d*. The square displacement curves of the two found components were fitted with anomalous diffusion representing functions (fig. 3.9*d*). Compared to cells plated on FN, the slow subpopulation had a tendency towards a more random mobility behavior ($\alpha = 0.7 \pm 0.2$ versus $\alpha = 0.49 \pm 0.06$), while the fast subpopulation

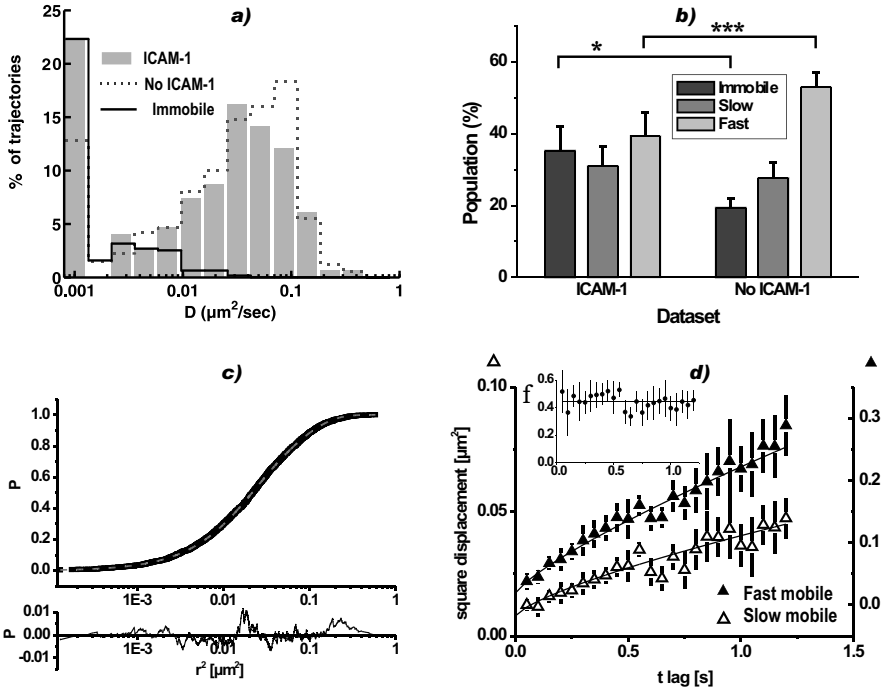

Figure 3.9. *L16 labeled LFA-1 nanoclusters on the dorsal membrane of THP-1 cells reveal an altered mobility when plated on ICAM-1 coated surfaces. a) Distributions of D of ICAM-1 plated cells (bars, 148 trajectories from 8 cells) and FN plated cells (grey dotted line) are being compared. The immobile subpopulation of ICAM-1 plated cells has been estimated (black line). b) The mobility subpopulations of ICAM-1 plated cells have been quantified (% of total population) and compared with the those found for FN plated cells.* $* \; p = 0.015$ *and* $* * * \; p = 0.038$. *c) The CPD of the mobile fraction of the L16 epitope subpopulation of ICAM-1 plated cells, fitted with a two-component diffusion model. Below: the residual between the fit function and the measurement data. d) The square displacement curves of the two found components were fitted with anomalous diffusion representing functions. An average slow mobile fraction* $f = 0.44 \pm 0.05$ *was found (line in inset). Error bars:* $2 \cdot \sigma$.

had a more anomalous behavior ($\alpha = 0.8 \pm 0.1$ versus $\alpha = 0.91 \pm 0.02$). These results indicate that local ligation has an overall effect on LFA-1 mobility.

To study differences in epitope specific mobility directly induced by binding of LFA-1 to ICAM-1, we analyzed datasets containing trajectories measured

at the ventral side of the cell. We obtained the logarithmic distributions of D for the TS2/4 and L16 epitope, see figure 3.10. The distribution of the TS2/4 epitope subpopulation on ICAM-1 coating (fig. 3.10*a*) has great resemblance with the distribution of immobile nanoclusters on fixed cells (envelope line). After subtraction of the estimated distribution of immobile nanoclusters, only a minor fraction of the trajectories remained in the distribution, indicating that most of the nanoclusters were indeed immobile. Furthermore, the nanocluster mobility of the TS2/4 epitope subpopulation on ICAM-1 plated cells was also compared to that obtained on FN plated cells (grey dotted line). Binding to ICAM-1 induced an increase of the immobile population from 26 ± 9% to 69 ± 7% (see inset). On the other hand, the distribution of D of the L16 epitope (fig. 3.10*b*) was essentially similar to that obtained on fixed cells, clearly indicating that upon ICAM-1 binding extended LFA-1 nanoclusters are immobile (with 79 ± 6% being immobile, see inset).

These data strongly suggest recruitment of $L16^+$ LFA-1 nanoclusters to the ICAM-1 binding site, which is in line with previous SDT studies on THP-1 monocytes [194]. Possibly, also inactive LFA - 1 is to some extend recruited to the binding site, where it might become activated by inside out signalling processes or by interaction with ICAM-1 [26]. Since L16 labeling has been performed *after* adherence to ICAM-1 coated surfaces, this possibility cannot be excluded. By assuming that exclusively $L16^+$ LFA-1 is immobilized at the ICAM-1 binding site, the percentage of recruited or converted $L16^+$ nanoclusters can be estimated. We scaled the immobile subpopulation of L16 to the immobile subpopulation of TS2/4 and estimated a L16 epitope subpopulation of 87% with respect to the total (TS2/4 labeled) LFA-1 population. This clearly indicates the massive recruitment of, or conversion towards, extended LFA-1 at the binding site. This recruitment was specific, since a much smaller immobile fraction was found when cells were plated on a FN coated surface (see fig. 3.3).

3.3.9 Induced microclustering of LFA-1 slows down its lateral mobility on the membrane

In the previous sections we found a significantly higher diffusion values of LFA-1 nanoclusters compared to other SPT (single particle tracking) studies on LFA-1 mobility [34, 176, 28]. Potential cross-linking of LFA-1 by beads used in SPT experiments might be one of the major causes of this discrepancy [135]. Therefore, we compared the LFA-1 lateral mobility between nanoclusters and artificially induced microclusters. THP-1 cells were plated on FN coated chambered coverglasses, labeled with L16 and imaged. First, L16 epitope mobility was assessed before the addition of co-grabbing secondary antibodies to the sample. Second, co-grabbing antibodies were added during the same experiment and mobility

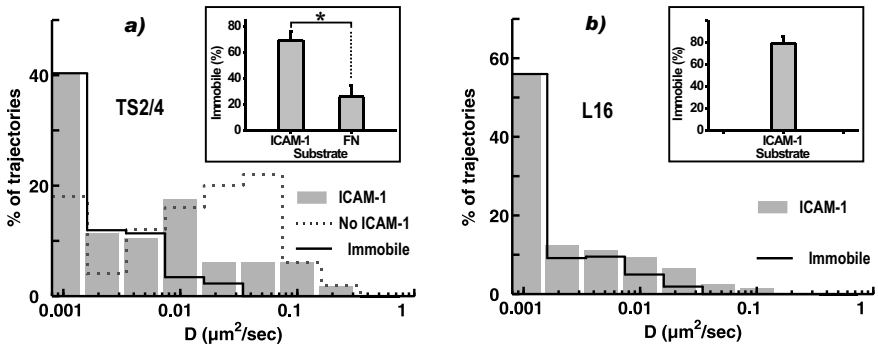

Figure 3.10. *Distributions of D of LFA-1 nanoclusters on the ventral side of ICAM-1-Fc plated cells (bars) versus distributions of immobile nanoclusters on fixed cells (black envelopes). a) The normalized distribution of the TS2/4 epitope subpopulation. The nanocluster mobility of the TS2/4 epitope subpopulation on ICAM-1 plated cells has been compared with nanocluster mobility on the ventral side of FN plated cells (grey dotted line). b) The normalized distribution of the L16 epitope subpopulation. Insets: Quantification of the immobile subpopulations (% of total population).* $* \; p = 0.0013$.

was assessed again after a stabilization period of 11 min. Representative extracted trajectories from before, and after adding co-grabbing antibodies are displayed in figure 3.11*a*. Clearly, Ab-induced microclusters (right) exhibited a slower or restricted type of mobility compared to nanoclusters (left). Single trajectory analysis confirmed this observation (fig. 3.11*b*). After co-grabbing, the distribution of diffusion constants becomes much broader and concentrated at values below $D_{th} = 0.01\mu m^2/s$ (see * in histogram). MSD analysis of all trajectories together before versus after co-grabbing revealed an eight fold decrease of the D upon addition of the co-grabbing antibodies ($D = 0.076 \pm 0.001\mu m^2/s$ before vs. $D = 0.0097 \pm 0.0004\mu m^2/s$ after co-grabbing). Microclustering increases valency, potentially enhancing the probability that a cluster contains cytoskeleton anchored LFA-1 molecules and thereby reducing mobility. Alternatively, microclustering might induce activation of LFA-1 molecules [43]. These observations support the idea that cross-linking is at least partly responsible for the differences in probed protein mobility between SDT as performed here and previous SPT experiments [34, 176, 28].

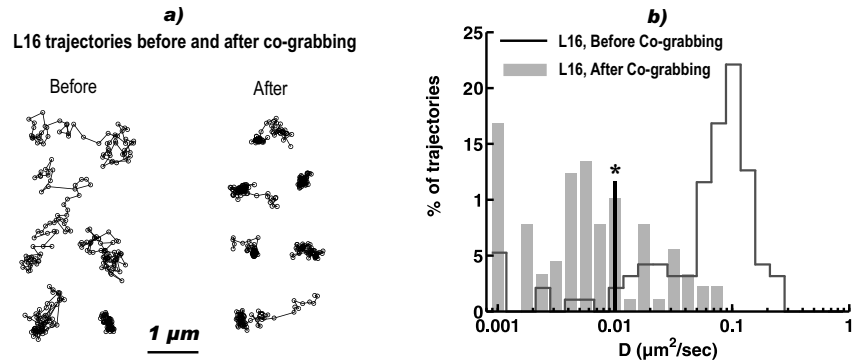

Figure 3.11. *L16 epitope nanocluster mobility on the dorsal side of the membrane of monocytic cells has been measured before and at least 11 min after addition of co-grabbing secondary antibodies. a) Two subsets of representative L16 epitope trajectories are displayed; one before, and one after adding secondary antibodies. To be able to compare both subsets by visual inspection, long trajectories have been selected and truncated at 61 frames. b) Distribution of diffusion constants before (black envelope line, 95 trajectories), and after adding secondary antibodies (grey bars, 89 trajectories).*

3.4 Discussion

We have performed a detailed study of conformation specific mobility of individual LFA-1 nanoclusters on monocytes by means of SDT techniques and labeling with conformation specific mAbs. Our results show that: (1) LFA-1 is primarily mobile on resting monocytes. (2) LFA-1 nanoclusters display different modes of motion as immobile, slow and fast mobile subpopulations have been observed. On resting cells, these mobile subpopulations show Brownian diffusion. (3) The minority of extended LFA-1 nanoclusters reveal a distinctive mobility profile compared to the overall LFA-1 nanocluster population. Although the distribution over immobile, slow and fast mobile subpopulations prevailed, the L16 epitope on resting cells reveals anomalous diffusion in the slow mobile subpopulation and a decreased mobility compared to the TS2/4 epitope. (4) A fraction of the extended LFA-1 on resting cells is anchored to the actin cytoskeleton. (5) On resting cells, at least $9 \pm 3\%$ of the extended LFA-1 exhibits transient confinement. (6) $L16^{+}$ nanoclusters are massively recruited to the ICAM-1 binding site. (7) Upon ligation, the mobility profile of the L16 epitope also changes at the unligated dorsal side of the cells. (8) Induced microclustering of LFA-1 slows down its lateral mobility on the membrane.

Based on the earliest SPT results of β_2 integrins on lymphocytes, it was

proposed that release of cytoskeletal restrains was an important step in the onset of β_2 integrin mediated binding [34]. Other work focussed on integrin conformational rearrangements and consequent affinity changes upon cell activation, leading to enhanced integrin mediated cell binding capacity [26]. These observations have supported the current paradigm of LFA-1 mobility regulation: on resting cells LFA-1 is in a low affinity conformation and bound to the cytoskeleton, while upon cell activation LFA-1 becomes active and released from the cytoskeleton, resulting in increased affinity, mobility and microclustering [185, 35, 31]. However, more complex models have also been proposed where cytoskeletal anchoring of LFA-1 is conformation specific and related to the integrins functional role during distinctive phases of the cells lifespan [79]. Recent SPT work on T cells provided direct evidence in favor of these models, by showing a more complex mobility pattern of LFA-1 where different subsets of conformational states have distinct interactions with the cytoskeleton, which can be influenced by cellular activation [28]. Our work is in line with these latest findings. We show that extended LFA-1 indeed has a distinctive mobility profile with respect to the total LFA-1 population and we show that part of the extended LFA-1 interacts with the actin cytoskeleton. Furthermore, mobility profiles of TS2/4 and L16 epitopes are modulated differently upon ligation of LFA-1 and show a reduced mobility of especially the extended conformation of LFA-1.

When LFA-1 is in the high affinity (extended open headpiece) conformation, there is an increased probability that it binds to the cytoskeleton by cytoplasmatic regulatory proteins like talin [193, 4, 192, 195]. Therefore, it is tempting to assign the high affinity form of LFA-1 to the cytoskeleton related, immobile fraction detected in our experiments, in agreement with Cairo et al. [28]. Since mAb L16 labels both the high and the intermediate (extended closed headpiece) affinity conformation of LFA-1, the latter should be assigned to the mobile fraction of $L16^+$ LFA-1. These results suggest that on resting monocytes only a small subpopulation (5%) of the total LFA-1 population needs to be in the high affinity form and anchored to the cytoskeleton providing the seed for nascent adhesion sites that after ligand activation will promote firm adhesion by diffusion of inactive and/or intermediate (mobile) LFA-1. In the case of the inactive form, activation will occur by coupling of outside-in signalling (brought about by the ligand in close proximity to the inactive molecules) with inside-out signalling, potentially mediated amongst others, by membrane rafts [77].

Since the TS2/4 epitope reflects the total population of LFA-1, it must also contain the L16 epitope subpopulation. Therefore, the found 19.4% of immobile L16 nanoclusters must be contained inside the 5% of immobile nanoclusters found for the TS2/4 epitope. The L16 epitope mobility subpopulations

can be scaled to the ratio between the L16 and TS2/4 immobile subpopulations in order to find the upper boundary of the fraction of $L16^+$ nanoclusters. Accordingly, at most 26% of all LFA-1 nanoclusters are L16 positive. This upper boundary is in good agreement with found colocalization results described elsewhere [3] and is supporting our suggestion that the immobile fraction can be assigned to the high affinity form of LFA-1. We subtracted the scaled L16 from the TS2/4 epitope mobility subpopulations and generated a representation of the balance between pro-active ($L16^+$) and inactive LFA-1 nanoclusters within the found mobility subpopulations on resting monocytes (fig. 3.12). It

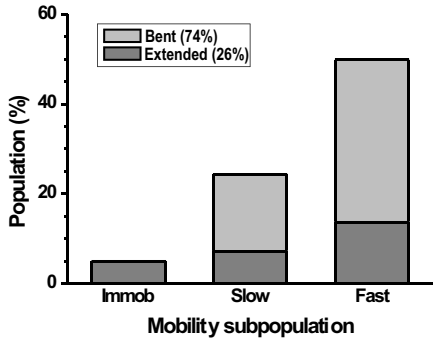

Figure 3.12. *Estimated mobility subpopulation fractions of the extended and bent conformation of LFA-1. Bars represent the percentage of the total LFA-1 population.*

can be observed that each conformational subset is differently distributed over all three mobility subpopulations, suggesting that each LFA-1 conformation has its own set of unique equilibria between general modes of mobility. We indeed observed considerable 'switching' of individual nanoclusters between different types of interaction with its micro environment in so-called transient confined trajectories. This idea of nanodomains 'switching' between different types of diffusion is in addition to the proposed 'switching' of LFA-1 molecules between conformational states, as proposed by Luo et al. According to their findings, integrins are not in an unchangeable conformational state, but have a certain probability to 'switch' between states [51]. Altogether, figure 3.12 suggests a meshwork of equilibria between conformational states and different types of interaction with the micro environment, which is illustrated in fig. 3.13. This meshwork of equilibria can be modulated directly by outside-in signalling processes like ligation or divalent cations binding to LFA-1, forcing the balances between conformational states towards the high affinity conformation and supporting adhesion [196, 3, 37]. The balance between mobility subpopulations and conformational subsets can also be altered by LFA-1 mediated inside-out

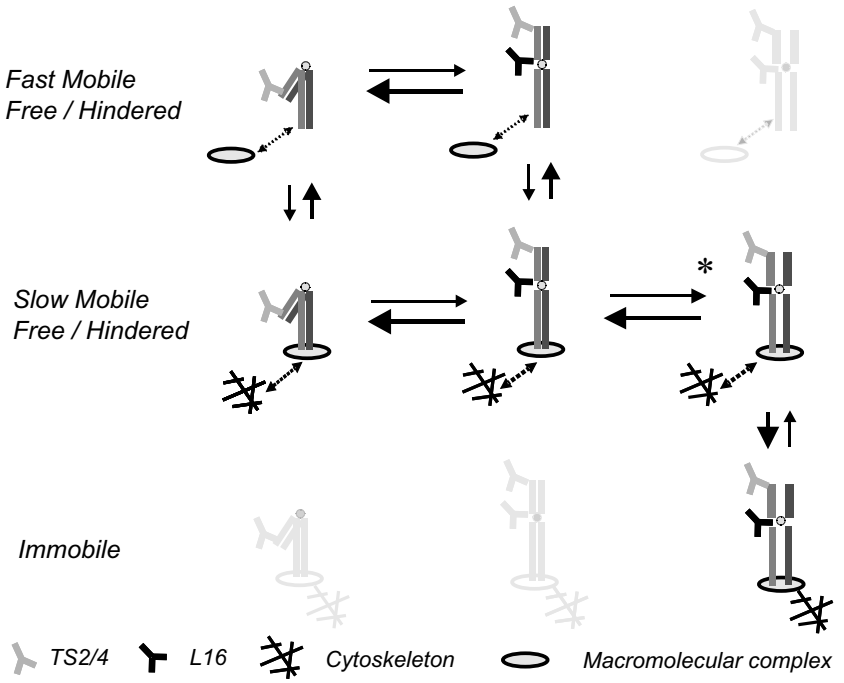

Figure 3.13. *We propose a model for observed LFA-1 mobility on monocytic cells. The total LFA-1 population is formed by different conformational subsets (columns) which are in equilibrium with each other (horizontal arrows). Each conformational subset contains its own set of equilibria (vertical arrows) between different mobility subpopulations (rows). Mobility subpopulations are caused by interaction of LFA-1 nanoclusters with their micro environment. Free moving nanoclusters (fast mobile subpopulation) slow down when coupled to macromolecular complexes (slow mobile subpopulation) and become immobile when coupled to the cytoskeleton. The arrows in between states are related to K_{on} and K_{off} values. Behavior of mobility subpopulations can become anomalous in case LFA-1 manifests transient interactions with macromolecular complexes or when it is hindered by structures like the cytoskeleton. In case cells are being plated on a chimera-ICAM-1 functionalized surface, the K_{on} between the extended closed headpiece and the extended open headpiece increases (see *), leading to an increased immobile subpopulation and a reduction of the fast mobile subpopulations.*

signalling pathways. It has been demonstrated that mobility and affinity of LFA-1 can be altered on a cellular scale [35, 197], but also on a subcellular scale [79, 2], to tailor LFA-1 mediated binding to a specific cell function in the immune system.

We indeed observed an alteration of the mobility profile of $L16^+$ LFA-1 upon ligation. When plating cells on ICAM-1 coated surfaces, the fast mobile subpopulation on the dorsal side became reduced and more anomalous with respect to FN plated cells. A mass-action driven transport of freely moving intermediate (fast mobile) LFA-1 towards the ICAM-1 binding site might have occurred. Once recruited at the binding site, LFA-1 would become further activated by ligation (extended open headpiece), which on its turn could trigger interaction with cytoplasmatic regulatory proteins to further strengthen the bond [196, 26, 3, 193]. An almost fully immobile L16 epitope subpopulation at the binding side confirmed this hypothesis. The reduced and more anomalous fast mobile subpopulation at the dorsal side can then be interpreted as remaining intermediate LFA-1, which was hindered on its way towards the binding site. Interestingly, the ratio between immobile and slow mobile nanoclusters at the dorsal unligated side of the cells increased, indicating enhanced docking of LFA-1 to the cytoskeleton at the unligated side of the cell. This increased docking to the cytoskeleton might be caused by an overall shift of the balances between LFA-1 conformers towards the high affinity state. Altogether, these results are in line with previous studies which showed that ligation with dimeric or multimeric ICAM-1 induced the high affinity state of LFA-1 at the binding site [196] and triggered recruitment of LFA-1 to the binding site [3, 28, 26]. In addition, we show that mobility subpopulations are also altered at the unligated cell side. These results suggest that local outside-in signalling processes induced by ligation, can trigger inside-out signalling pathways regulating the overall balance between conformational states and consequently mobility.

The lateral mobility of LFA-1 has been studied before, by means of FRAP (Fluorescence Recovery After Photobleaching) and SPT [34, 176, 184, 28]. To our knowledge, this is the first time SDT has been applied for the study of LFA-1 mobility on leukocytes. The majority of LFA-1 nanoclusters show unhindered diffusion. Therefore, found diffusion constants can be compared to those found by FRAP and other methods deriving diffusion constants over longer time periods and larger spatial areas [158, 131]. The diffusion constants found by us on monocytes are in the same order as FRAP results found by others on cultured neutrophils, T cells and blood derived T cells [28, 195, 198]. SPT studies on transformed B-cells and on T-cell lines found 2-20 times smaller diffusion constants, depending on experimental conditions and used probes [34, 176, 28]. Besides microcluster formation of LFA-1 by beads, differences in cell lines and sample temperature, a-specific labeling most probably played a major role in these differences. Therefore, found diffusion constants in SPT

experiments are hard to relate to each other or to SDT experiments in an absolute manner. Our experiments are done at 37 °C using a SDT approach and therefore give a most realistic picture of the absolute diffusion constant of individual integrin receptor nanoclusters on cultured leukocytes.

The mechanism behind the found slow and fast mobility subpopulations remains unclear. Our cytoskeleton disruption experiments exclude the actin cytoskeleton as a cause for distinctive slow and fast mobile subpopulations. Furthermore, the modeled relation between lateral mobility and nanocluster cross-sectional radius was found to be weak and there are not many examples of large changes in receptor mobility due to clustering alone [199]. Besides, we did not find a correlation between lateral mobility and probed nanocluster intensity in our data. Alternatively, LFA-1 might participate in macromolecular complexes formed by interaction with TM4SF proteins (transmembrane-4 superfamily) like CD81 [200] or CD82 [201], see figure 3.13. TM4SF proteins may facilitate assembly of signalling complexes by tethering intracellular signaling molecules to integrin heterodimers [202, 203]. Once LFA-1 nanoclusters associate with these macromolecular complexes, its diffusion constant decreases due to increased drag caused by protein-protein interactions on the cytoplasmic side of the complex. However, CD81 is fully excluded from LFA-1 on monocytes and CD82 is only associated with LFA-1 during its recruitment at the ligand binding site (R. Diez-Ahedo, unpublished results).

Another possible explanation for distinctive slow and fast LFA-1 mobility subpopulations is association of LFA-1 with lipid rafts. Cholesterol-rich lipid rafts have been proposed to be involved in microclustering of LFA-1, though these studies seem to be quite controversial [82, 36, 204, 83]. Results from biochemical analysis suggested that at the plasma membrane, integrin-tetraspanin signalling complexes are partitioned into specific microdomains *proximal* to cholesterol-rich lipid rafts [203]. Direct nanoscale imaging has been applied to map the LFA-1 nanocluster and GPI-AP (raft components) nanodomain organization on the membrane of resting THP-1 monocytes and a subpopulation (25%) of LFA-1 in close proximity of GPI-APs was observed [77]. Alternatively, rafts have a bridging role between extended LFA-1 and the actin cytoskeleton [86, 87], which could explain the transient confinement and the anomalous diffusion observed in the L16 positive fraction of LFA-1. Altogether these studies suggest that a fraction of LFA-1 nanoclusters does interact with, but does not reside inside lipid rafts.

Nevertheless, the effect of rafts on their local membrane viscosity forms a likely explanation for the observed slow mobile subpopulation. The effects at a distance of both mobile and immobile membrane proteins on a diffusing "tracer" molecule can be of strong influence on membrane viscosity (i.e., the drag exerted by immobile particles in an intervening fluid) [205]. Therefore, the effect of cytoskeleton tethered GPI-AP nanodomains on the effective viscosity

experienced by diffusing LFA-1 nanoclusters in their direct vicinity might be sufficient to induce a separate, slow mobile subpopulation. In addition, the fraction of LFA-1 nanoclusters in close proximity of GPI-AP nanodomains (25%) [77] is comparable to the percentage of slow mobile LFA-1 nanoclusters. Further investigation is required to validate this hypothesis.

The anomalous behavior observed in the slow mobile subpopulation might have its origin in collisions with a densely packed structure of 'fixed' obstacles underneath the membrane, like the cytoskeleton [206]. Since only extended $L16^+$ LFA-1 moves in an anomalous fashion, we hypothesize that extended LFA-1 tends to make larger protein complexes on the intracellular side, enhancing the possibility of hinderance by these structures. Furthermore, anomalous diffusion might be related to a broad distribution of periods of transient confinement. Transient confinement or transient immobility in part of the L16 subpopulation might either originate from continuously changing traps [131, 154] or from protein-protein interactions [73]. The former might be due to interactions of LFA-1 with the dynamic meshwork of actin, inter filaments [185] or micro tubili [184] underneath the membrane, while the latter might have its origin in interactions between LFA-1 and short-existent lipid rafts [67, 207, 65] or between extended LFA-1 and cytoskeleton related proteins like talin [193, 192, 195]. Since only a minority of the slow mobile LFA-1 moves in a hindered manner, there must be separate mechanisms for decreasing LFA-1 mobility and inducing anomalous diffusion.

3.5 Conclusion

We have demonstrated that on resting monocytes, LFA-1 is primarily mobile, without interaction to the cytoskeleton and with a small subset of nanoclusters in the extended conformation. This subset displays a different mobility profile with immobile cytoskeleton tethered, slow hindered and fast Brownian diffusion. Upon ligation, extended LFA-1 is massively recruited to and immobilized at the binding site. We propose that the subset of immobile, extended LFA-1 exhibits the high affinity (extended open headpiece) conformation and is responsible for the onset of LFA-1 mediated adhesion. Initial binding is further strengthened by mass-action driven recruitment of mobile LFA-1 nanoclusters to the ligand binding site. Remarkably, the diffusion profile of extended LFA-1 also alters at the unligated, dorsal side of the cell, suggesting that local outside-in signalling processes induced by ligation, can trigger inside-out signalling pathways regulating the overall balance between conformational states and consequently mobility.

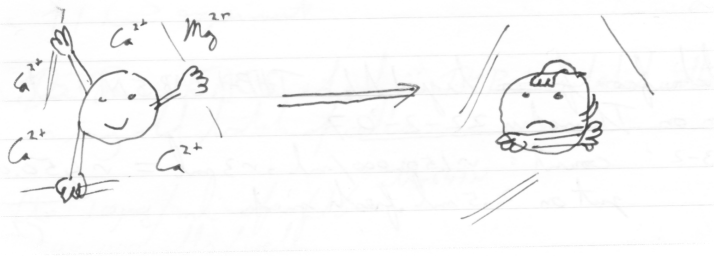
Ca2+
Mg2+
Ca2+
Ca2+
Ca2+

Chapter 4

Extracellular Ca^{2+} Links Integrin Nanocluster Conformation to Mobility

Extracellular Ca^{2+} ions seem to play a dual role in affinity versus avidity regulation of LFA-1 mediated adhesion. Although removal of extracellular Ca^{2+} increases integrin activation by promoting high affinity states of LFA-1, avidity has found to be reduced under these conditions. To investigate this controversy, we applied SDT (single dye tracing) in combination with conformer specific antibody labeling to map the mobility of individual LFA-1 nanoclusters on resting monocytes under different extracellular cation conditions. We found that under low (0.04mM) Ca^{2+} conditions nanocluster mobility is strongly reduced with respect to high (0.4mM) Ca^{2+}/Mg^{2+} conditions. We further observed that the mobility of the overall LFA-1 population and the fraction containing extended LFA-1 became similar. Cytoskeleton disruption reversed immobilization of LFA-1. On the other hand, the reduction of the extracellular Mg^{2+} level did not have any strong effects on nanocluster mobility. Altogether, we find that extracellular Ca^{2+}, but not Mg^{2+}, induces conformational changes that translate into global rearrangements of the LFA-1 nanocluster activation state, affecting nanocluster mobility via interaction with the actin cytoskeleton. With shear flow assay experiments we observed that under low shear flow conditions (0.2 dyn/cm^{-2}), Ca^{2+} dependent avidity synergizes with Mg^{2+} dependent affinity to establish LFA-1 mediated cell binding. Under higher shear flow conditions (0.5 dyn/cm^{-2}) only affinity seems to play a role. Our results have direct implications for studies where integrin activation is induced by removal of Ca^{2+} because although high affinity forms are generated, this pool of molecules is not able to reach the required avidity, failing to support firm adhesion under low shear flow conditions.

The results described in this chapter will be published as:

Bakker G.J., Diez-Ahedo R., Eich C., Perez-Samper G., van Zanten T., Figdor C.G., Cambi A. and Garcia-Parajo M.F. *Lateral mobility of individual integrin nanoclusters orchestrates the onset for leukocyte adhesion,* **submitted**

4.1 Introduction

The integrin LFA-1 plays a crucial role in leukocyte arrest and migration through the vasculature and in binding to antigen presenting cells. Aside from binding to its ligand ICAM-1, LFA-1 is also a bi-directional mediator of signals across the extracellular membrane [25]. Signalling properties and monomeric ligand binding capacity modulation go hand in hand, both depending on structural re-arrangements within the protein [4]. Outside-in signals are articulated as a modulation of the distance between cytoplasmic domains upon interplay of divalent cations [38, 4] and ligands [25, 43] with the extracellular domains of the integrin. By means of binding and shear flow assays these conformational changes could be coupled to changes in affinity of LFA-1 for its counter ligand in model systems like K562 cells [37, 38, 11, 30, 42, 208]. It has been suggested that the two key steps of leukocyte adhesion, i.e. rolling and firm arrest, are regulated by conformational changes of integrins on the headpiece, which in turn can be modulated by external divalent cations [37, 209, 42].

How these cation-induced conformational changes of LFA-1 affect downstream signalling cascades and what kind of inside-out signalling processes they regulate in leukocytes remains poorly understood. Ca^{2+} ions seem to play a dual role in regulation of LFA-1 mediated adhesion: mutagenesis experiments showed that removal of Ca^{2+} favor the high affinity form of the integrin and combined with Mg^{2+} synergize to promote firm adhesion [37, 38]. Accordingly, high Ca^{2+} concentrations (>1mM) have a negative regulatory effect so that integrins become involved in rolling by establishing weak, transient interactions with their ligand [210, 37]. These experiments have supported the current paradigm for integrin activation brought about by cations (bypassing the requirements for intracellular signaling events): high Ca^{2+} levels stabilize integrins in the inactive or low affinity conformations, while Ca^{2+} removal (in the presence of Mg^{2+}) increases integrin activation by promoting high affinity states. On the other hand, Ca^{2+} ions seem to induce microclustering of LFA-1 on various types of T lymphocytes, a necessary step for avidity-based regulation [30].

These apparent conflicting observations suggest that extracellular divalent cations might simultaneously regulate affinity and avidity so that both modes of integrin function modulation are interconnected. Such an interconnection between affinity and avidity has been found for inside-out regulatory processes, induced by PMA-stimulation or cytokines. It was shown that inside-out signalling induced cytoskeleton mediated redistribution of LFA-1 and/or changes in affinity, depending on the triggered signalling pathways [35, 79, 197, 9, 28, 211]. The dependence of endogenous LFA-1 mediated adhesion upon extracellular cation concentrations has been demonstrated by shear flow experiments on primary blood lymphocytes [9]. When solely cations were used, cell binding was reduced compared to chemokine induced inside-out signalling processes, but

divalent cation dependent modes of motion (rolling, arrest) prevailed upon cytokine stimulation, underscoring the relevance of divalent cations in the process of cell binding under physiological conditions. Yet, the precise role of divalent cations regulating affinity and avidity remains obscure despite that their absolute requirement for integrin function is widely recognized [4].

Here we exploit the high spatial (nanometer) accuracy and temporal resolution of SDT (single dye tracing) microscopy to measure for the first time the lateral diffusion of individual LFA-1 nanoclusters on the dorsal side of live monocytes under different divalent cation conditions. We used the activation reporter mAb NKI-L16 (further referenced as L16) to discriminate nanoclusters containing extended LFA-1 from the overall LFA-1 population (labeled with mAb TS2/4). In the previous chapter, it was shown that under high extracellular cation conditions (0.4mM Ca^{2+}/Mg^{2+}), most nanoclusters diffused randomly, while extended slow mobile nanoclusters diffused in an anomalous fashion. Upon tenfold reduction of extracellular Ca^{2+} concentrations a vast increase of the immobile and slow mobile subpopulations was observed for both epitopes, with a concomitant decrease of the percentages of the fast mobile subpopulations. Furthermore, the mobility in the overall LFA-1 population and in the fraction containing extended LFA-1 became similar. Cytoskeleton disruption reversed the alterations of nanocluster mobility, although more nanoclusters remained in the slow mobile subpopulation. Reduction of the extracellular Mg^{2+} level did not have a strong effect on nanocluster mobility. Our results indicate that extracellular Ca^{2+} couples affinity to avidity in a process that is tightly regulated by the cytoskeleton.

4.2 Materials and Methods

Antibodies and labeling

Antibody conjugates TS2/4-AlexaFluor647, TS2/4-Atto520 and L16-Atto647N were used in epi-fluorescence experiments and flow cytometry measurements. A goat-anti mouse IgG-AlexaFluor488 antibody conjugate was used as a secondary labeling antibody for flow cytometry. Phalloidin-TRITC staining was used to label the F-actin cytoskeleton. A detailed description of used antibodies is given in Chapter 3.

Cell culture and sample preparation

Cell culture and sample preparation were performed according to the procedures described in Chapter 2. Shortly, THP-1 monocytes (referenced as monocytes) were incubated on FN (Fibronectin) coated Labtek II cover glasses for 15 minutes. After removal of unbound cells, samples were blocked by a 15 min incubation with 1% Human Serum in RPMI. After blocking, cells were washed

twice with buffer A (RPMI-1640), buffer B (PBS + 0.1mM Ca^{2+}); or buffer C (Ca^{2+}- and Mg^{2+}-free HBBS, Sigma-Aldrich, H6648 + 0.04mM Ca^{2+}), depending on the experiment. During the last rinsing step, cells were incubated for 5 minutes. Then, samples were incubated for 3.5 minutes with 0.2μg/ml L16-Atto647N or TS2/4-AlexaFluor647 in buffer A or B or with 0.2μg/ml L16-Atto647N and $2\mu g/ml$ TS2/4-Atto520 in buffer C. All further steps (labeling, rinsing and measurement) were performed as described in Chapter 2, except that 'RPMI' should be read as buffer A, B or C. All incubation steps were performed at 37 °C. Specific isotype controls were always taken along.

Preparation of Cytochalasin-D treated samples

Three samples were prepared simultaneously and measured right after each other; one sample was treated with 1μg/ml Cyto-D and doubly labeled with L16 and TS2/4, the two control samples were treated with 0.5μl/ml DMSO only. One control was labeled as the Cyto-D treated sample, the other control sample was labeled with the appropriate isotype controls. Approximately 10^5 cells were taken, rinsed in RPMI, re-suspended in 1ml RPMI + Cyto-D and incubated for 15 minutes. Then, samples were prepared with HBBS + Ca^{2+} according to the paragraph above, with the main difference that Cyto-D or DMSO was added to all solutions used in all sample preparation steps. At the start of the measurement, samples were incubated with Cyto-D for 1hr:12min.

Flow cytometry analysis

The procedure described in Chapter 3 has been followed, except for the following modifications. For buffers, HBBS + BSA + 1mM Ca^{2+}/Mg^{2+} or +0.04mM Ca^{2+} were used. Furthermore, samples were secondary labeled with $10\mu g/ml$ GαM-Cy5^{TM} antibodies in a similar manner as described for the primary labeling step. Finally, samples were measured without fixation.

Cellular Imaging

Single molecule detection sensitive dual-color excitation / emission epi- fluorescence microscopy has been described in Chapter 2 and 3. Briefly, samples were excited with one or two gated laser excitation sources. For each frame, the pulse length and power density were set to 4ms, ~1kW/cm^2 for the 633nm HeNe laser and 2ms, ~2kW/cm^2 for the 514.5nm line of an Ar^+Kr^+ laser. Fluorescence was collected with a 60x TIRFM objective, filtered and projected onto an Intensified CCD camera. Movies were retrieved at a frame rate of 10Hz (TS2/4 labeled cells measured under 0.4mM Ca^{2+}/Mg^{2+} and 0.1mM Ca^{2+} conditions) or 20Hz (all other conditions). Typical position accuracies

were $0.037\mu m$ for single Atto647N molecules on glass. Experiments were performed at 37 °C. DIC (Differential Interference Contrast) enhanced bright field imaging was used to select stretched cells which were imaged above the nucleus, to avoid detection of autofluorescence from the cytosol.

Single Dye Tracing and analysis of (mean) square displacements

SDT techniques and analysis of square displacements have been described in Chapter (2). Briefly, two dimensional trajectories in the plane of focus were reconstructed by the aid of colloidal particle tracking software [171], which has been modified and implemented for tracing of fluorescently marked individual nanoclusters on living cells. MSD (mean square displacement) curves were generated for every single trajectory with a minimum length of 13 frames. The short timelag diffusion coefficient D was retrieved by linear fitting (first 3 or 4 points of the MSD plot for a trajectory length of $\geq$13 or $\geq$21 frames respectively). Finally, a semi-logarithmic histogram of D for individual LFA-1 nanoclusters was generated.

CPD (Cumulative Probability Distribution) analysis [158] was further used to identify and characterize different mobility subpopulations within the mobile fraction of the trajectories ($D \geq D_{th}$). For CPD analysis, trajectories $\geq$ 21 frames were selected, resulting in $D_{th} = 0.006\mu m^2/s$ (see 2.3). One or two components were identified in the mobile fraction and their square displacement curves were retrieved. Fit parameter f corresponds to the slow diffusing part of the mobile fraction (in case 2 components were identified). Square displacement curves were fitted with an anomalous diffusion representing function: $r(t)^2 = \Gamma \cdot t^{\alpha} + {\Delta_0}^2$ [131], where $r(t)^2$ is the square displacement of the component in question at time lag t, Γ is the transport coefficient, α is the anomalous parameter and ${\Delta_0}^2$ is the square displacement offset at $t = 0$. In addition, square displacement curves were also fitted with a linear function through the first four points to obtain the short timelag diffusion coefficient (D) of the retrieved components. The component with the lowest D was defined as the 'slow' mobile subpopulation and the other component was defined as the 'fast' mobile subpopulation.

Finally, the immobile, slow and fast mobility subpopulations were quantified (% of the total number of trajectories). For that, the immobile subpopulation has been estimated by scaling the histogram of D of immobile nanoclusters on fixed cells to the first bar ($D < 0.001\mu m^2$) in the histogram of the experimental dataset. Then, the average of the fit parameter f was used to determine the percentages of the slow and fast mobile subpopulations. Error bars represent the approximated standard deviation of the mobility subpopulation in question. Significance levels were derived using the single sided two-sample z-test.

Shear flow assay

THP-1 cells under different cation conditions with/without Cyto-D treatment were prepared along the line of sample preparation protocols described above. For Mn^{2+} containing buffers, Hepes was used instead of HBBS to avoid precipitation. The total incubation times of cells under different conditions were kept similar compared to epi-fluorescence experiments. Cells were brought to a concentration of $0.5x10^6$ cells/ml. In blocking experiments, anti-α_L integrin antibody NKI-L15 (10μg/ml) was included. Cover slips (40mm Menzel, Braunschweig, Germany) were coated with 10μg/ml Protein A (Sigma) for 2 hours at 37 °C. Coverslips were washed with PBS; Protein A coated coverslips were overlaid with 10μg/ml recombinant ICAM-1-Fc (R&D systems) and assembled in a 37 °C Focht flow chamber, mounted on an inverted phase-contrast microscope (Axiovert 35M Zeiss) connected to a camera (Variocam, PCO computer Optics GmbH, Kelheim, Germany). Cells were perfused at physiological shear stress rates (0.1-1.5 dyne/cm^2) for 60 sec. After washing for 1-5 min, adherent cells were monitored by imaging 5 microscopic fields (1,673 mm^2) and adherent cells were quantified.

4.3 Results

4.3.1 Expression of L16 and TS2/4 epitopes at different Ca^{2+} conditions

The expression levels of the LFA-1 L16 and TS2/4 epitopes on THP-1 cells under 1mM Ca^{2+}, Mg^{2+} and 0.04mM Ca^{2+} extracellular cation concentrations have been assessed by immunofluorescence flow cytometry analysis to validate antibody conjugate functionality, see fig. 4.1. Since mAb TS2/4 binds in a non-conformational dependent manner, extracellular Ca^{2+} should not affect its expression level. As expected the expression level of TS2/4 remained constant. On the other hand, L16 expression decreased upon reduction of Ca^{2+} concentrations. The mAb L16 reads out the extended conformation of LFA-1, though its expression level is also dependent on the presence of Ca^{2+} at the integrin genu [39]. Therefore, this result demonstrates the functionality of the L16 conjugate by showing its dependence on the presence of extracellular Ca^{2+}. However, the result on its own does not report on the expression level of extended conformation LFA-1.

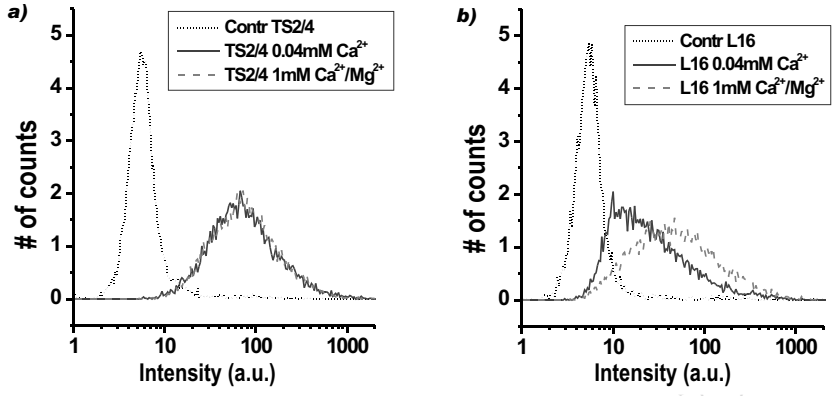

Figure 4.1. *The expression levels of the LFA-1 TS2/4 and L16 epitopes on THP-1 cells have been assessed by immunofluorescence flow cytometry analysis. Cells were incubated, labeled and measured in HBBS + 0.04mM Ca^{2+} versus HBBS + 1mM Ca^{2+}, Mg^{2+} in order to compare epitope expression at different cation levels. The following median intensity values have been found for the analyzed samples (1mM Ca^{2+}+Mg^{2+}, 0.04mM Ca^{2+} and control respectively): TS2/4: 70, 67 and 5.4; L16: 44, 20 and 5.2.*

4.3.2 Effect of extracellular Mg^{2+} on LFA-1 mobility

In body fluids, Mg^{2+} and Ca^{2+} ions are present at a concentration of ∼1mM. Mg^{2+} ions are of utter importance for conformational integrin activation. Indeed, without Mg^{2+} bound to the β I-like domain of the integrin, the probability to convert to the high-affinity open headpiece conformation is very low [37]. Although Mg^{2+} has been associated with the affinity state of LFA-1, its role in integrin mobility has not been investigated yet. Here we inquire on the effect of Mg^{2+} on LFA-1 nanocluster mobility. In figure 4.2, the distributions of diffusion coefficients of the TS2/4 (a) and L16 (b) epitopes are shown. The mobility of both epitopes display high overlap between 0.1mM Ca^{2+} without Mg^{2+} (bars) and 0.4mM Ca^{2+}, Mg^{2+} (dotted line) conditions, with a broad, predominantly mobile distribution of diffusion constants spread over more than one order of magnitude. Aside from a decrease on the peak of the mobile fraction of the TS2/4 epitope in the absence of Mg^{2+}, no potential influence of Mg^{2+} is found on the distribution of D of the epitopes investigated.

Since the distribution of D does not report on long term diffusion behavior, we applied CPD analysis to study the mobile fraction of our trajectories over a longer time interval (typically 1.2s). For both epitopes we were able to discriminate a slow and a fast mobile subpopulation within the mobile fraction.

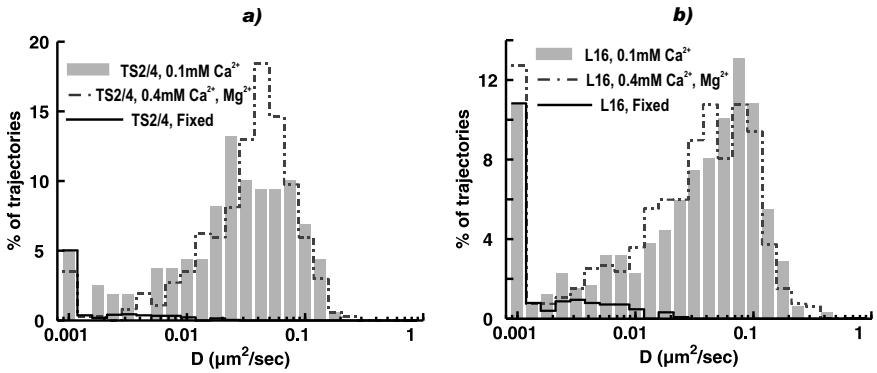

Figure 4.2. *The distributions of diffusion coefficients of the TS2/4 (fig. a) and L16 (fig. b) epitopes measured in buffer without Mg^{2+} (0.1mM Ca^{2+}, bars) and with Mg^{2+} (0.4mM Ca^{2+}, Mg^{2+}, dotted lines). The bins in the histograms are normalized to the total number of trajectories (TS2/4: 318 and 369 trajectories, L16: 656 and 669 trajectories for 0.1mM Ca^{2+} and 0.4mM Ca^{2+}, Mg^{2+} respectively). Black envelopes: estimated distributions of immobile nanoclusters.*

Retrieved square displacement plots were fitted with an anomalous diffusion function. The results of the analysis are compared with the high Ca^{2+}, Mg^{2+} conditions (fig. 4.3 and table 4.1).

In absence of Mg^{2+} and under reduction of Ca^{2+}, no major changes can be observed for the type of diffusion of LFA-1 nanoclusters. The α value of the slow mobile subpopulation of the L16 epitope increases slightly ($p < 0.07$, single sided two-sample z-test), indicating that the LFA-1 nanoclusters within this fraction experienced less hindrance from their micro environment. Mobility in other subpopulations and short time lag diffusion constants (D_{slow} and D_{fast}) remained similar. Moreover, no major changes can be observed in f (the slow diffusing part of the mobile fraction) of the L16 epitope. On the other hand, f of the TS2/4 epitope increased from 0.3 to 0.45 ($p < 0.05$, single sided two-sample z-test). The latter observation is in line with the reduced peak in the distribution of D (fig. 4.2).

In all, these results show that absence of Mg^{2+} and fourfold reduction of Ca^{2+} have minor effects on the lateral mobility of LFA-1 observed under high extracellular Ca^{2+}, Mg^{2+} conditions.

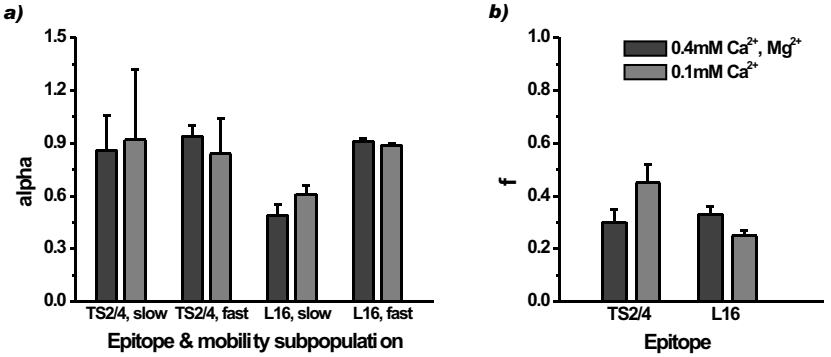

Figure 4.3. *CPD analysis of the mobile fractions of the TS2/4 and L16 epitope trajectories measured in buffer with 0.1mM Ca^{2+} in the absence of Mg^{2+} versus buffer with 0.4mM Ca^{2+}, Mg^{2+}. (a) The type of diffusion of the slow and fast components was characterized by fitting obtained square displacement curves with an anomalous diffusion representing function (table 4.1) and the α values are represented. (b) The slow diffusing part of the mobile fraction (f) under given cation conditions. Error bars: σ.*

4.3.3 LFA-1 mobility decreases dramatically upon reduction of extracellular Ca^{2+}

To investigate the effect of extracellular Ca^{2+} on LFA-1 mobility we monitor LFA-1 nanocluster dynamics under different extracellular Ca^{2+} concentrations. Because extracellular Ca^{2+} is essential for cell viability, we compromised on the low-Ca^{2+} condition and used a minimum concentration of 0.04mM. The distributions of diffusion constants of individual trajectories of both TS2/4 and L16 epitopes reveal a strong decrease of LFA-1 nanocluster mobility upon reduction of extracellular Ca^{2+} to a level of 0.04mM in absence of Mg^{2+} (see fig. 4.4). The distribution of TS2/4 labeled nanoclusters displays a reduction of the peak in the mobile fraction with an associated strong increase of the immobile subpopulation. The distribution of L16 labeled nanoclusters displays a similar shift between subpopulations together with an increase of slow mobile trajectories (see $*$ in fig. 4.4).

We further used CPD analysis to inquire on the TS2/4 and L16 mobility profiles at low Ca^{2+} concentrations and compared retrieved results with those found at higher Ca^{2+} concentrations (fig. 4.5 and table 4.1). First, a trend towards more anomalous diffusion i.e., reduction of α, can be observed in the fast mobile subpopulations of both epitopes, indicating hindered diffusion on

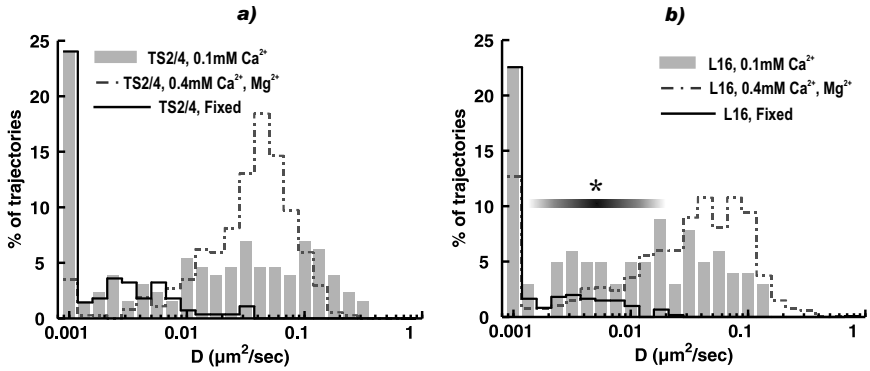

Figure 4.4. *The distributions of diffusion coefficients of the TS2/4 (a, 129 trajectories) and L16 (b, 102 trajectories) epitopes measured under 0.04mM Ca^{2+} conditions (bars) compared with the 0.4mM Ca^{2+}, Mg^{2+} condition (dotted lines). Black envelopes: estimated distributions of immobile nanoclusters. $*$: area in histogram containing a mixture of slow mobile and immobile trajectories.*

the membrane (fig. 4.5a). Interestingly, the mobility of the slow mobile subpopulation of the L16 epitope becomes less anomalous. Second, the fraction of slow mobile trajectories is increasing upon reduction of extracellular Ca^{2+} levels (fig. 4.5b). This trend can especially be appreciated in the TS2/4 epitope. Third, the short term diffusion constants of both L16 epitope mobility subpopulations are decreasing upon reduction of Ca^{2+} levels (table 4.1). Altogether, our results show that the short and long term diffusion are reduced upon reduction of extracellular Ca^{2+} levels.

A quantification of immobile, slow mobile and fast mobile subpopulations of both epitopes is given in figure 4.6. For both epitopes, the immobile subpopulation increases at the expense of the fast mobile subpopulation when extracellular Ca^{2+} is decreased from 0.4mM to 0.04mM. Furthermore, upon reduction of extracellular Ca^{2+} levels, the percentages of mobility subpopulations of the TS2/4 and L16 epitopes approach each other.

All in all, LFA-1 mobility decreases dramatically upon reduction of the extracellular Ca^{2+} concentration. Furthermore, our results show that the differences in long term diffusion behavior and in mobility subpopulations between the TS2/4 and L16 epitope disappear upon reduction of extracellular Ca^{2+}.

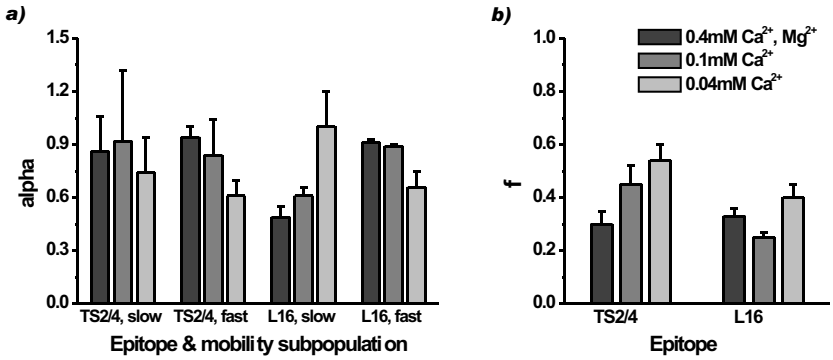

Figure 4.5. *The mobile fractions of TS2/4 and L16 epitope trajectories retrieved under 0.04mM Ca^{2+} conditions have been analyzed by means of the CPD method. The results are compared with those obtained under 0.1mM Ca^{2+} and 0.4mM Ca^{2+}, Mg^{2+} conditions. (a) The type of diffusion of the slow and fast components was characterized by fitting obtained square displacement curves with an anomalous diffusion representing function (table 4.1) and the α values are represented. (b) The slow diffusing part of the mobile fraction (f) under given cationic conditions. Error bars: σ.*

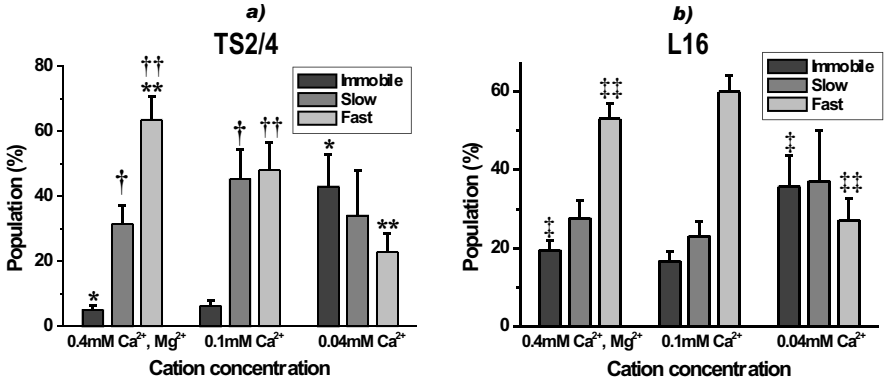

Figure 4.6. *Quantification of mobility subpopulations of TS2/4 (a) and L16 (b) epitopes under different extracellular cation conditions. Cells were measured under 0.4mM Ca^{2+}+Mg^{2+}, 0.1mM Ca^{2+} and 0.04mM Ca^{2+} conditions and relative sizes (%) of immobile, slow mobile and fast mobile subpopulations were estimated. Error bars represent the standard deviation.* $*\ p < 0.001$, $**\ p < 0.00003$, $\dagger\ p < 0.11$, $\dagger\dagger\ p < 0.08$, $\ddagger\ p < 0.03$ *and* $\ddagger\ddagger\ p < 0.001$

$< r^2 >= \Gamma t^{\alpha} + \Delta_0$	α_{slow}	α_{fast}	f
TS2/4,0.4mM Ca^{2+}, Mg^{2+}	0.86 ± 0.2	0.94 ± 0.06	0.30 ± 0.05
TS2/4,0.1mM Ca^{2+}	0.92 ± 0.4	0.84 ± 0.2	0.45 ± 0.07
TS2/4,0.04mM Ca^{2+}	0.74 ± 0.2	0.61 ± 0.09	0.54 ± 0.06
L16,0.4mM Ca^{2+}, Mg^{2+}	0.49 ± 0.06	0.91 ± 0.02	0.33 ± 0.03
L16,0.1mM Ca^{2+}	0.61 ± 0.05	0.89 ± 0.01	0.25 ± 0.02
L16,0.04mM Ca^{2+}	1.0 ± 0.2	0.66 ± 0.09	0.40 ± 0.05

$< r^2 >= 4Dt + \Delta_0$	D_{slow} $[\mu m^2/s]$	D_{fast} $[\mu m^2/s]$	pnts
TS2/4,0.4mM Ca^{2+}, Mg^{2+}	0.014 ± 0.005	0.056 ± 0.006	3411
TS2/4,0.1mM Ca^{2+}	0.015 ± 0.004	0.079 ± 0.01	1698
TS2/4,0.04mM Ca^{2+}	0.008 ± 0.003	0.073 ± 0.01	620
L16,0.4mM Ca^{2+}, Mg^{2+}	0.017 ± 0.001	0.081 ± 0.001	12627
L16,0.1mM Ca^{2+}	0.0098 ± 0.0003	0.076 ± 0.001	13415
L16,0.04mM Ca^{2+}	0.0029 ± 0.002	0.035 ± 0.004	1196

Table 4.1. *Analysis of the mobile fractions of TS2/4 and L16 epitope subpopulations retrieved at different extracellular cation concentrations. The fit parameters D and α were obtained together with their errors. Furthermore, fraction f and the number of points of the CPD (at a time lag of 3 frames) are presented. The χ^2_{red} values of the fit functions were < 1.2 for TS2/4 and < 0.33 for L16 square displacement curves.*

4.3.4 LFA-1 binds to the actin cytoskeleton upon reduction of extracellular Ca^{2+} levels

To study the role of the cytoskeleton in the immobilization of LFA-1 upon reduction of extracellular Ca^{2+}, we probed LFA-1 mobility upon cytoskeleton disruption treatment at 0.04mM Ca^{2+} conditions. The distributions of diffusion coefficients of the overall TS2/4 labeled LFA-1 population of Cyto-D-treated and DMSO control cells are shown in figure 4.7. Upon Cyto-D treatment, the immobile subpopulation reduced more than fourfold compared to the data of the control, to a percentage similar to TS2/4 labeled cells under 0.4mM Ca^{2+}, Mg^{2+} conditions. DMSO has no significant effect on the immobile fraction (see fig. 4.7b). These results show that at low extracellular Ca^{2+} levels, immobile LFA-1 is tethered to the actin cytoskeleton since it is released upon cytoskeletal disruption.

Interestingly, the mobile fraction of the distribution of diffusion coefficients observed upon Cyto-D treatment under low Ca^{2+} conditions is not equal to the distribution observed under 0.4mM Ca^{2+}, Mg^{2+} conditions (fig. 4.7a). Although tethered nanoclusters are released from the cytoskeleton, the fast mobile subpopulation did not restore to levels observed under high Ca^{2+} conditions. Instead, a peak appears at 0.01 $\mu m^2/s$, suggesting that alteration of extracellular Ca^{2+} levels is not only modulating immobilization of LFA-1 to the actin cytoskeleton.

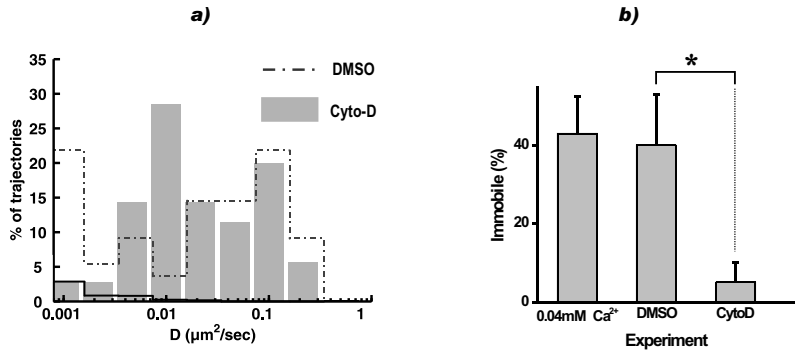

Figure 4.7. *The effect of Cyto-D-treatment on LFA-1 nanocluster mobility under 0.04mM Ca^{2+} conditions, in the absence of Mg^{2+}. a) The distributions of diffusion coefficients of TS2/4 labeled LFA-1 on Cyto-D-treated cells (bars, 35 trajectories) and DMSO control cells (dotted line, 55 trajectories) are shown. The black envelope represents the estimated distribution of immobile nanoclusters. b) Immobile subpopulations have been quantified and compared with the immobile subpopulation of untreated cells measured under 0.04mM Ca^{2+} conditions. Error bars:* $1 \cdot \sigma$. $*$ $p < 0.006$

We also investigated the effect of Cyto-D treatment on the mobility of the extended form of LFA-1 using the L16 epitope. In figure 4.8*a* the distribution of diffusion coefficients of Cyto-D treated cells under 0.04mM Ca^{2+} conditions is presented. In line with the results on the TS2/4 epitope (fig. 4.7), figure 4.8*a* shows a strong reduction in immobile LFA-1 nanoclusters upon Cyto-D treatment while the fraction of slow mobile trajectories increases. This trend can be appreciated more clearly in figure 4.8*b*, where an almost fourfold decrease of the immobile and a increase of the slow mobile subpopulation is obtained upon Cyto-D treatment.

Furthermore, the percentages of mobility subpopulations of the L16 epitope observed upon Cyto-D treatment under low Ca^{2+} conditions are not equal to those observed under 0.4mM Ca^{2+}, Mg^{2+} conditions. The slow mobile subpopulation is increased and the fast mobile subpopulation is reduced compared to high Ca^{2+}, Mg^{2+} conditions ($p < 0.006$ and $p < 0.02$ respectively). In contrast, the type of diffusion of the L16 epitope became similar to those observed under 0.4mM Ca^{2+}, Mg^{2+} conditions. The slow mobile subpopulation showed anomalous diffusion, while the fast mobile subpopulation displayed random diffusion upon Cyto-D treatment (see the fit parameters retrieved from CPD

analysis, table 4.2).

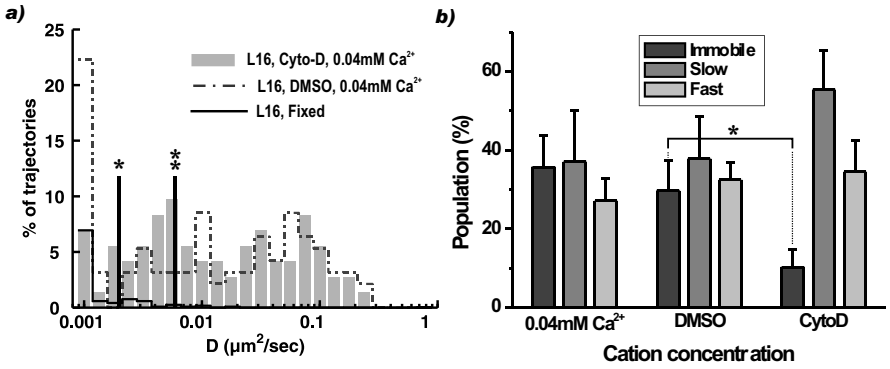

Figure 4.8. *The effect of cytoskeleton disruption treatment upon the L16 epitope mobility under 0.04mM Ca^{2+}, no Mg^{2+} conditions. a) The distributions of diffusion coefficients of Cyto-D treated cells (bars, 72 trajectories) and DMSO control cells (dotted line, 94 trajectories) are shown. The minimum trajectory length was 21 frames. The black envelope represents the estimated distribution of immobile nanoclusters. $*$ and $**$: threshold levels for the CPD analysis of Cyto-D and DMSO treated cells respectively. Since the immobile subpopulation of Cyto-D treated cells was small, the threshold level for the mobile fraction (D_{th}) could be set at a lower value while keeping overlap of the immobile subpopulation and mobile fraction below 5%. b) Mobility subpopulations have been quantified and compared with the mobility subpopulations of untreated cells measured under 0.04mM Ca^{2+} conditions. Error bars: $1 \cdot \sigma$. $*$ $p < 0.02$.*

Altogether, these results show that under low extracellular Ca^{2+} conditions, LFA-1 is tethered to the actin cytoskeleton. Actin cytoskeleton disruption releases tethered LFA-1 and the type of mobility reverses to those observed under high cation conditions. Interestingly, the percentages of slow and fast mobile nanoclusters do not reverse upon cytoskeleton disruption, indicating that alteration of extracellular Ca^{2+} levels has a global effect on LFA-1 mobility and not solely modulates cytoskeletal tethering.

4.3.5 Extracellular Ca^{2+} enhances cell binding under low, but not under high shear flow conditions.

Since extracellular Ca^{2+} affected conformational state and lateral mobility of LFA-1 nanoclusters, we questioned whether extracellular Ca^{2+} played also a role on cell adhesion under shear flow conditions. Therefore, we assessed cell binding to highly dense ICAM-1 coated substrates (see 4.2) by means of shear flow assay

$< r^2 >= \Gamma t^\alpha + \Delta_0$	α_{slow}	α_{fast}	f
L16, Cyto-D	0.46 ± 0.08	0.95 ± 0.05	0.59 ± 0.09
L16, DMSO	0.77 ± 0.2	0.77 ± 0.05	0.45 ± 0.04
L16, 0.04mM Ca^{2+}	1.0 ± 0.2	0.66 ± 0.09	0.40 ± 0.05
L16, 0.4mM Ca^{2+}, Mg^{2+}	0.49 ± 0.06	0.91 ± 0.02	0.33 ± 0.03

$< r^2 >= 4Dt + \Delta_0$	D_{slow} $[\mu m^2/s]$	D_{fast} $[\mu m^2/s]$	pnts
L16, Cyto-D	0.007 ± 0.002	0.056 ± 0.006	2234
L16, DMSO	0.012 ± 0.005	0.09 ± 0.02	2026
L16, 0.04mM Ca^{2+}	0.0029 ± 0.002	0.035 ± 0.004	1196
L16, 0.4mM Ca^{2+}, Mg^{2+}	0.017 ± 0.001	0.081 ± 0.001	12627

Table 4.2. *The mobile fraction of the dataset of Cyto-D-treated (low Ca^{2+}) L16 labeled cells and its DMSO control as analyzed by the CPD method (see figure 4.5d). The results from 0.04mM Ca^{2+} and 0.4mM Ca^{2+}, Mg^{2+} datasets have been added. The fit parameters D and α were retrieved together with their errors. Furthermore, fraction f and the number of points of the CPD (at a time lag of 3 frames) are presented. The χ^2_{red} values of the square displacement fit functions were < 0.41 .*

experiments under different shear flow and extracellular cation conditions (fig. 4.9)[1]. Base level cell binding was determined by testing conditions in addition of LFA-1 blocking antibodies (mAb L15). The effect of Cyto-D-treatment on LFA-1 mediated binding has been tested for 0.04mM Ca^{2+} conditions with DMSO as a control.

Under low shear flow conditions (0.2dyn/cm^2), a combination of high Ca^{2+} and high Mg^{2+} are required to induce binding (fig. 4.9a). Although the extended, high affinity LFA-1 conformation has a prevalence for low Ca^{2+} + high Mg^{2+} conditions [42, 209, 37], less binding was observed at 0.04mM Ca^{2+} + 1mM Mg^{2+} compared to 0.4mM Ca^{2+}, Mg^{2+}. This is a remarkable result, since it is in apparent contradiction to earlier reports on K562 cells, where firm adhesion at different shear-stress conditions was obtained at low Ca^{2+} levels in the presence of Mg^{2+} [37, 209]. In fact, our data show that at low shear-flow conditions, higher Ca^{2+} levels, which allow surface mobility of LFA-1 nanoclusters being uncoupled from the cytoskeleton (fig. 4.4 and 4.6), appear to be more effective to promote cell binding than lower Ca^{2+} levels, which enhance LFA-1 affinity. Thus, at low shear-flow conditions, Ca^{2+}-mediated avidity appears to dominate over Ca^{2+}-mediated affinity.

Besides high Ca^{2+}, Mg^{2+} also appears to play an important role to induce binding under low shear flow conditions. Conditions containing both high Ca^{2+} and high Mg^{2+} induced more binding than conditions containing only high Ca^{2+} or only high Mg^{2+}. Therefore, our results indicate that also Mg^{2+}

[1]Measurement and analysis of shear flow essay results have been performed by Christina Eich, Department of Tumor Immunology, Nijmegen Centre for Molecular Life Sciences, Radboud University Nijmegen Medical Centre, The Netherlands.

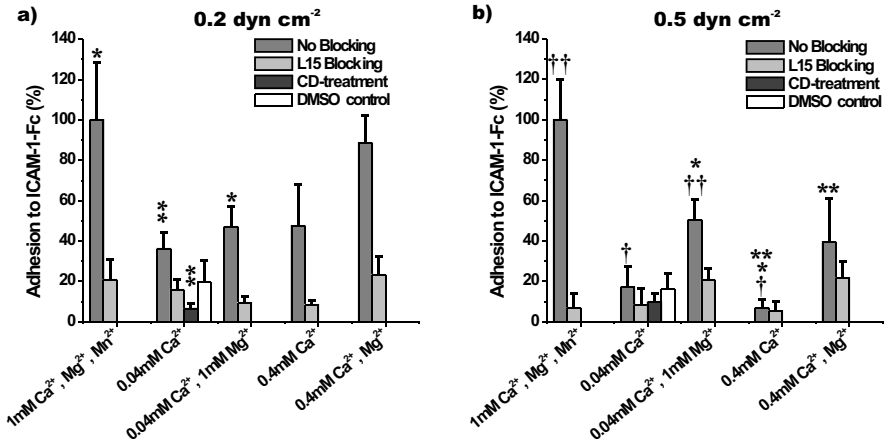

Figure 4.9. *The role of extracellular cations on LFA-1 adhesiveness under shear flow conditions. THP-1 cell binding to ICAM-1 coated surfaces has been quantified as a percentage of maximum binding observed at 1mM Ca^{2+}, Mg^{2+}, Mn^{2+} conditions at (a) 0.2 dyn cm^{-2} and (b) 0.5 dyn cm^{-2}. Error bars: standard deviation over average binding calculated over 5 different areas. One out of two experiments is presented. (a) $*\ p < 0.007$, $**\ p < 0.0013$. (b) $*\ p < 0.0001$, $**\ p < 0.071$, † $p < 0.18$ and †† $p < 0.014$.*

mediated affinity is important for cell binding under low shear flow conditions.

Surprisingly, Cyto-D treatment at 0.04mM Ca^{2+} did not result in increased adhesion, even when LFA-1 nanoclusters became more laterally mobile (fig. 4.7 and 4.8) and thus, in principle, able to increase its avidity state. The failure of LFA-1 to support firm adhesion under shear-flow conditions once the cytoskeleton is disrupted might therefore reflect its inability to stabilize initial bonds in the absence of proper cytoskeleton anchorage.

Under higher shear flow conditions (0.5dyn/cm^2), cell binding was highly dependent on Mg^{2+} (fig. 4.9b). In contrast with low shear flow conditions, the presence of extracellular Ca^{2+} did not have any effect on cell binding while addition of Mn^{2+} did increase cell binding capacity. Since Mg^{2+} and Mn^{2+} are strong promoters of LFA-1 affinity [4, 208, 30] and since no strong effect of Mg^{2+} on LFA-1 mobility was observed (paragraph 4.3.2), these results indicate that at higher shear forces affinity of LFA-1 to its ligand plays a more prominent role than its lateral mobility on the cell membrane.

4.4 Discussion

In this chapter, we have shown that mobility patterns of LFA-1 can be influenced by extracellular Ca^{2+} levels, in a conformation specific manner. It has been shown that a combination of low Ca^{2+} and high Mg^{2+} levels favors the extended, high affinity LFA-1 conformation [42, 209, 37]. We indeed observed that the mobility of the total LFA-1 population gradually changed as a function of Ca^{2+} reduction and became essentially the same as to the one displayed by extended ($L16^{+}$) LFA-1 at low Ca^{2+} levels (table 4.1 and figure 4.6). Under low (0.04mM) Ca^{2+} conditions, we observed a strong reduction of LFA-1 nanocluster mobility with respect to high (0.4mM) Ca^{2+}, Mg^{2+} conditions. In addition, our cytoskeleton disruption experiments showed that the increased percentage of immobile nanoclusters is a consequence of increased cytoskeletal anchoring of LFA-1. Since the immobile, cytoskeleton-tethered fraction can be assigned to the high affinity, extended open headpiece conformation ([193, 4, 192, 195] and our previous chapter), our results indicate that low extracellular Ca^{2+} is responsible for converting inactive to pro-active LFA-1 nanoclusters in a ligand-independent fashion.

An explanation for the observed changes in both affinity and avidity upon alterations of the extracellular Ca^{2+} level can be found in the bi-directional signalling properties of LFA-1 [25, 212, 213]. It has been demonstrated that integrin transmembrane domain separation is coupled to conformational rearrangements in the extracellular part of the integrin [25]. In case of outside-in signalling, these global rearrangements could lead to modulation of interactions between LFA-1 and related cytosolic proteins like talin [214], α-actinin [40], kindlins [215], cytohesin-1 [216] and filamin [217] that link integrins directly or indirectly to the cytoskeleton. So far, outside-in signalling of LFA-1 has only been observed for binding of specific monoclonal antibodies or as a result of ligation with soluble ICAM-1 in the presence of Mn^{2+} [25]. Our results imply that reduction of extracellular Ca^{2+} also induces conformational changes in LFA-1 that translate into integrin extension and transmembrane domain separation, leading to increased interactions with cytoskeletal mediators in the direct micro-environment of LFA-1.

On the other hand, the effects of Mg^{2+} seem to be locally confined to the headpiece of the integrin [4, 37] and do not translate into global conformational changes of the molecule that affect its avidity on the cellular membrane [44, 30]. We indeed showed that Mg^{2+} has a minor effect on the lateral mobility of LFA-1 (fig. 4.3). Moreover, the observed LFA-1 mobility follows the trend observed upon reduction of extracellular Ca^{2+} levels rather than the absence of Mg^{2+} being of influence (fig. 4.5 and 4.6).

In line with the results of others, we observed that Ca^{2+} ions have opposing effects on affinity versus avidity regulation of LFA-1 mediated adhesion. Our results indicate that the extended high affinity LFA-1 conformation is promoted

upon reduction of extracellular Ca^{2+} levels. In line with our results, shear flow experiments of others showed enhanced arrest of cells under high extracellular Mg^{2+}/ without Ca^{2+} or under Mg^{2+}/EGTA conditions [210, 209, 9]. In contrast, our work reveals that these intermediate and/or high affinity forms of the integrin are largely stationary on the cell surface underscoring a coupling between conformational states and cytoskeleton regulators in turn affecting the avidity state of the molecules. This result is in line with a previous study on avidity regulation of LFA-1, where it has been shown that binding of Ca^{2+}, but not Mg^{2+}, directly correlates with microclustering of LFA-1 at the cell surface of T cells, thereby facilitating LFA-1-ligand interaction under static conditions [30]. In addition, shear flow experiments on lymphocytes demonstrated that on low densities of ICAM-1, a combination of extracellular Mg^{2+} and Ca^{2+} induced a higher number of stable tethered cells than Mg^{2+} + EGTA [9]. Thus, depending on the experimental model used, the positive (in case of avidity) or negative (in case of affinity) regulatory effect of extracellular Ca^{2+} seems to dominate in the process of LFA-1 ligand binding.

We investigated the functional implications of the apposing effects of Ca^{2+} on LFA-1 mediated monocyte adhesion under different shear-flow conditions. Ca^{2+} ions had neither a positive nor a negative effect on LFA-1 mediated binding under higher shear stress conditions. Under these conditions, Mg^{2+}-induced affinity was sufficient to induce firm adhesion (fig. 4.9b). In contrast, under low shear flow conditions Ca^{2+}-mediated avidity was capable of supporting firm adhesion (fig. 4.9a). These results correlate with cation-dependent LFA-1-ligand binding of lymphocytes under high shear flow [9] and static [30] conditions respectively. Our results have direct implications for studies where integrin activation is induced by removal of Ca^{2+} because although high affinity forms are generated, this pool of molecules is not able to reach the required avidity, failing to support firm adhesion under low shear flow conditions. Moreover, we show that the extracellular Ca^{2+} level can be used to differentially tune the balance between affinity and avidity of LFA-1 ligand binding on resting monocytes.

Physiological Ca^{2+} and Mg^{2+} levels in most tissues are comparable to those found in the blood, which are approximately 1mM [218]. Our results suggest that under these conditions, LFA-1 avidity and affinity act in synergy in order to create optimal integrin mediated adhesion. Interestingly, a reduced ratio between extracellular Ca^{2+} and Mg^{2+} concentrations has been related to an enhanced cell migration during wound healing [219–221]. Furthermore, it was found that pathophysiological shifts in cations similar to those found in wound healing also enhance integrin mediated cell adhesion, migration and proliferation of several types of carcinoma [222–225]. Brought in the context of these physiological studies, the differential role of extracellular Ca^{2+} in LFA-1-ligand

binding might constitute a general mechanism to dynamically adapt integrin-ligand binding to the given circumstances throughout the body, by tightly regulating the interplay between affinity and avidity.

The importance of an intact cytoskeletal machinery in the regulation of LFA-1 mediated binding is demonstrated by cytoskeleton disruption treatment under low Ca^{2+} conditions. In contrast with early SPT experiments on resting lymphocytes [34], cytoskeleton disruption abolished β_2 integrin mediated binding despite the induced increase of LFA-1 mobility. However, this discrepancy can be addressed to differences in the activation state of LFA-1 between the cell types in question, since work on activated peripheral blood lymphocytes with already clustered LFA-1 showed reduced LFA-1 mediated binding upon cytoskeleton disruption [185]. Integrin-cytoskeleton bonds have found to play an important role in stabilizing integrin mediated adhesion [40, 79, 214]. Binding of cytosolic proteins like talin and kindlins to the transmembrane domains of LFA-1 are able to induce the high affinity state and association to the actin cytoskeleton [215]. Furthermore, immobile integrins can act as a force sensor, starting an inside-out signalling cascade upon initial binding [226]. Our cytoskeleton disruption data underlines the importance of this link between the intracellular and extracellular domain. Possibly, the pool of anchored, high affinity LFA-1 provides the seed for nascent adhesion sites that after ligand activation will promote firm adhesion by diffusion of inactive and/or intermediate (mobile) LFA-1 ([77] and 3.4).

Interestingly, the percentages of mobility subpopulations observed upon Cyto-D treatment under low Ca^{2+} conditions are not equal to those observed under 0.4mM Ca^{2+}, Mg^{2+} conditions. Instead, a significant increase of the slow mobile subpopulation can be observed, showing that not only the amount of cytoskeleton associated, but the whole mobility profile of LFA-1 is affected upon change of extracellular Ca^{2+} levels. This result suggests that cytoskeletal association of integrins is not a single step process, but can rather be viewed as multiple intermediate stages being coupled by a series of equilibria [6, 4]. These thoughts are in line with the model proposed in chapter 3, where it was illustrated that each LFA-1 conformation has its own set of unique equilibria between general modes of mobility and we postulated a meshwork of equilibria between conformational states and types of interaction with the microenvironment of LFA-1 nanoclusters. Here we apply this model to deepen our understanding of the dependency of LFA-1 conformation and mobility upon extracellular Ca^{2+} conditions, see figure 4.10.

The configuration of LFA-1 conformations and mobility subpopulations under high extracellular cation conditions (0.4mM Ca^{2+}/Mg^{2+}) has been described extensively in the discussion of Chapter 3. Shortly, under these conditions LFA-1 nanoclusters have the highest probability to exhibit random diffusion and to be part of the fast mobile subpopulation (fig. 4.10, upper

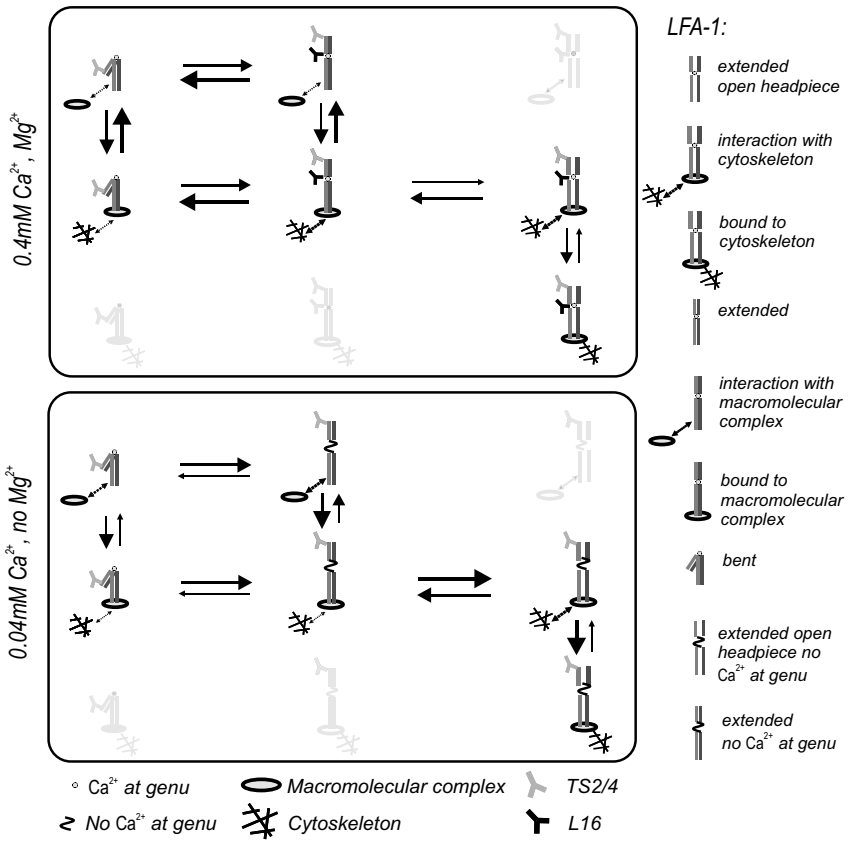

Figure 4.10. *Model for observed LFA-1 mobility on monocytic cells under different cation conditions. The total LFA-1 population is formed by different conformational subpopulations which are in equilibrium with each other (columns). Epitope specific LFA-1 mobility profiles are built up out of mobility subpopulations, which are also in epitope dependent equilibrium with each other (rows). Bent and extended LFA-1 conformations can have Ca^{2+} at the integrin genu (yellow dot) or not (wire). The arrows in between states are related to K_{on} and K_{off} values. Large arrows point towards most favorable states and less favorable states are colored gray. Behavior of mobility subpopulations can become anomalous in case LFA-1 manifests interaction (small arrows) with macromolecular complexes or cytoskeletal structures.*

box, first row). There is a smaller probability that nanoclusters are part of the slow mobile subpopulations (middle row). Slow mobile nanoclusters containing extended LFA-1 transiently interact with the cytoskeleton, depicted by anomalous diffusion (fig. 3.5). The smallest subpopulation is formed by nanoclusters which contain cytoskeleton tethered extended open headpiece LFA-1. The lower box in figure 4.10 illustrates a possible arrangement of equilibria between mobility and conformational states under low extracellular Ca^{2+} conditions. The L16 epitope requires Ca^{2+} bound near the genu subunit and its expression is therefore reduced under low Ca^{2+} levels [39]. Since the extended conformational states are in favor at low Ca^{2+} conditions, equilibria are shifted towards states on the right side. Consequently, more LFA-1 resides in the extended open headpiece conformational state, which has a preference to interact with the cytoskeleton ([193, 4, 192, 195] and our previous chapter). Therefore, a large fraction of LFA - 1 nanoclusters resides in the immobile state (lower right corner). Upon cytoskeleton disruption, nanoclusters containing extended LFA-1 are unable to form a stable link to the disturbed actin cytoskeleton and a new balance between the available states is created, reflected by the altered mobility subpopulation and epitope fractions. According to our data, the balance between mobility subpopulations is shifted towards the slow mobile states upon cytoskeleton disruption. Possibly, slow mobile LFA-1 nanoclusters originate from increased drag of LFA-1 stably bound to complexes of cytoskeleton related proteins [217, 215], which are known to be crucial in the formation of a stable link between the integrin and the cytoskeleton.

Upon Cyto-D treatment under low Ca^{2+} conditions, the type of diffusion of the L16 epitope became similar to those observed under 0.4mM Ca^{2+}, Mg^{2+} conditions. The slow mobile subpopulation showed anomalous diffusion, while the fast mobile subpopulation displayed random diffusion upon Cyto-D treatment (table 4.2 and fig. 4.5). This is a remarkable observation, since these nanoclusters are supposed to be unable to form a stable link to the disturbed actin cytoskeleton. Likely, the observed anomalous diffusion originates from interactions with other cytoskeletal structures than the filamentous actin. LFA-1 nanoclusters might interact with (LFA-1 related proteins associated to) micro tubuli [184] or intermediate filaments [185]. Interaction with other cytoskeletal structures than filamentous actin might also explain the Cyto-D treatment resistant immobile subpopulation.

4.5 Conclusion

In the previous chapter we demonstrated that under physiological divalent cation conditions, LFA-1 is primarily mobile on resting monocytes and that the minority of active ($L16^+$) LFA-1 nanoclusters has a distinctive mobility profile

with a small immobile subpopulation. Here we showed that under low extracellular Ca^{2+} conditions nanocluster mobility is strongly reduced with respect to high Ca^{2+} conditions: the immobile, cytoskeleton tethered subpopulation of the overall LFA-1 population increased 8-fold. Furthermore, we observed that the mobility of the total LFA-1 population gradually changed as a function of Ca^{2+} reduction and became essentially the same as to the one displayed by active LFA-1 at low Ca^{2+} levels. On the other hand, the absence of extracellular Mg^{2+} did not have any major effects on LFA-1 mobility. Altogether, we found that reduction of extracellular Ca^{2+}, but not Mg^{2+}, induces conformational changes in LFA-1 that translate into integrin extension and transmembrane domain separation, leading to increased interactions with cytoskeletal mediators in the direct micro-environment of LFA-1. Our results have direct implications for studies where integrin activation is induced by removal of Ca^{2+} because although high affinity forms are generated, this pool of molecules is not able to reach the required avidity, failing to support firm adhesion under low shear flow conditions. Moreover, we showed that the extracellular Ca^{2+} level can be used to differentially tune the balance between affinity and avidity of LFA-1 ligand binding on resting monocytes.

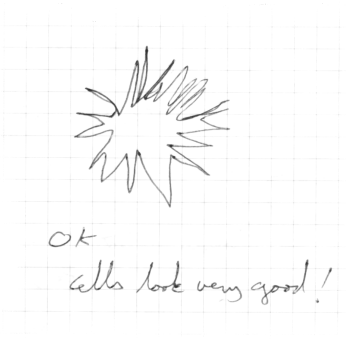

Chapter 5

Comparison of Lateral Mobility and Spatial Organization of LFA-1 on Different Immune Cells

Upon differentiation of monocytes into immature Dendritic Cells (imDCs), LFA-1 membrane organization in nanoclusters disperses and its affinity reduces. So far, the fundamental question of how these changes in organization and conformational state relate to mobility has not been addressed yet. We applied single dye tracing to examine the mobility of LFA-1 molecules on the cell membrane of imDCs and compared the results with those obtained on resting monocytes. Like on monocytes, imDCs also display immobile, slow and fast mobile subpopulations displaying similar, predominantly random diffusion. However, in contrast to monocytes, the diffusion constant of the total, primarily inactive LFA-1 population is twofold larger. This increased mobility correlates well with its change in spatial organization from nanocluster to monomeric. In addition, we compared LFA-1 mobility of imDC with resting T cells, which have a comparable low activation state of LFA-1. Compared to T cells, the LFA-1 diffusion constant is two- to fourfold smaller on imDCs. Furthermore, our observations on imDCs and T cells show that the immobile subpopulation of active LFA-1 is strongly reduced compared to monocytes, indicating that these cell types barely express cytoskeleton tethered, open headpiece conformations of LFA-1. Thus, we demonstrated that besides affinity, also changes in the nano-scale organization of LFA-1 influence its lateral mobility. Furthermore, differences in the local membrane viscosity experienced by LFA-1 are a likely explanation for the observed differences in LFA-1 diffusion constants between imDCs and resting T cells and, between slow and fast mobility subpopulations.

5.1 Introduction

Along their lifespan, monocytes differentiate into imDCs and consequently loose their spontaneous LFA-1 mediated binding capacity [3]. Surprisingly, the expression level of LFA-1 on the cell membrane remains unaltered during this transition [3]. Recently, it has been shown that on blood-derived resting monocytes LFA-1 is distributed in active and inactive (also named as extended and bent conformation) LFA-1 nanoclusters on the cell membrane [3]. Live imaging of monocyte-T-cell conjugates showed that only the active nanoclusters were recruited to the binding site. Upon differentiation towards imDCs, LFA-1 organization disperses and its affinity for its ligand reduces. This study demonstrated in a semi-physiological setting how integrin molecular re-arrangements (affinity) and integrin organization (valency) interplay to adapt integrin functionality for a specific cell stage and local environment. Despite its importance in valency regulation, LFA-1 mobility has not been monitored alongside these alterations in affinity and distribution.

Although LFA-1 is homogeneously distributed and primarily inactive on DCs, recent studies suggest an active role for LFA-1 in the DC life cycle. It has been shown that ligand binding to the pathogen recognition receptor DC-SIGN triggered recruitment of LFA-1 to the binding site where it interacts with ligands shared with DC-SIGN [15]. Furthermore, LFA-1 on recipient DCs becomes activated upon interaction with antigen bearing exosomes from donor DCs [16]. In addition, reactivation of LFA-1 on DCs appears to occur upon interaction with leukocyte chemokine CCL21 [227]. Also, a recent study showed involvement of ICAM-1 (intercellular adhesion molecule 1) in homing to the lymph nodes, suggesting an active role of LFA-1 in DC migration [17]. Finally, it was demonstrated in vivo that β_2 integrins play a role in the ameboid migration mode of DCs [18]. Above that, the fundamental question of how changes in organization and conformational state relate to mobility prompted us to study LFA-1 mobility on cell types where LFA-1 is less active and homogeneously distributed over the cell surface.

Here we present a detailed study of LFA-1 mobility on monocyte-derived imDCs and compare the results with those obtained for monocytes and Jurkat T cells. We applied SDT techniques, analysis of individual trajectories and ensemble averaging techniques to assess the mobility of LFA-1 molecules and nanoclusters on the plasma membrane. We obtained mobility profiles of the total LFA-1 population and the active fraction by labeling with mAb TS2/4 and the activation reporter mAb NKI-L16 (further referenced as L16) [24]. Like on monocytes, the majority of LFA-1 on imDCs is mobile, distributed over slow and fast mobile subpopulations and diffusing in a random fashion. However, the diffusion constants of individual LFA-1 trajectories increased by twofold while the immobile subpopulation of $L16^+$ LFA-1 reduced by fourfold compared to monocytes. According to our previous results (chapter 3 and 4), the reduced

immobile subpopulation indicates a decreased fraction of high-affinity open headpiece LFA-1, with respect to the total L16$^+$-LFA-1 fraction. We applied hydrodynamic theory to show that the increased mobility of LFA-1 matches the alteration of the spatial distribution from nanoclusters to monomeric. Interestingly, LFA-1 mobility of both slow and fast mobile subpopulations matched hydrodynamic theory, but with a different membrane viscosity. Like imDCs, resting T cells also have a reduced LFA-1 activation state with respect to monocytes [228, 79], which is reflected by their absent L16$^+$-LFA-1 immobile subpopulation. Compared to T cells, imDCs reveal a much wider distribution of diffusion constants which are shifted to two- to fourfold lower values.

Our results demonstrate that besides affinity, also changes in the nanoscale organization of LFA-1 influence its lateral mobility. In our discussion we show that differences in the local membrane viscosity experienced by LFA-1 are a likely explanation for the observed differences in LFA-1 diffusion constants between imDCs and resting T cells and, between slow and fast mobility subpopulations.

5.2 Materials and Methods

Antibodies and antibody conjugates

Antibody conjugates TS2/4-Atto520 and NKI-L16-Atto647N were a gift from the Tumor Immunology Laboratory, (NCMLS, the Netherlands). Both TS2/4 and L16 are reactive with the alpha subunit of LFA-1 [3]. The commercially available conjugates mIgG1κ-AlexaFluor647, mIgG1κ-PE and mIgG2α-APC were used as isotype controls.

Cell culture

Immature DCs (imDCs) were cultured from human peripheral blood monocytes as described previously [229, 230]. Briefly, monocytes were isolated by adherence to plastic and cultured in the presence of IL-4 and GM-CSF (500 and 800 U/ml, respectively) for 10 days. At day 3, the phenotype of the cultured DCs was confirmed by flow cytometry analysis. Jurkat A2 T cells (further referenced as T cells) were cultured in IMDM without phenol red, with L-glutamine and 5% FCS. Cells were propagated at a concentration of 0.2M cells/ml by resuspension in fresh medium every other day. The day before the experiment, cell culture was brought to a concentration of 400.000 cells/ml. THP-1 monocytes (referenced as monocytes) were cultured as described in chapter 3.

Sample preparation

Chambered cover glasses were coated with Poly-L-Lysine (Sigma-Aldrich, P1524, from human plasma) by 1 hour incubation in PBS with $50\mu g/ml$ Poly-L-Lysine. ImDC culture was diluted with RPMI to a final concentration of 10^5cells/ml containing 2-3%FBS. Cells were incubated for 20 min on PLL coated chambered coverglasses and unbound cells were removed. Then, samples were blocked by 15 min incubation with 1% Human Serum in RPMI. After blocking, samples were rinsed and incubated with antibody conjugates in RPMI medium at a concentration of $2\mu g/ml$ (TS2/4-Atto520) or 0.25 $\mu g/ml$ (L16-Atto647N) for 3.5 minutes. After labeling samples were rinsed in RPMI without phenol red, which was used as imaging medium. The measurement started 10 minutes after the beginning of the labeling step. T cells were re-suspended in IMDM and plated on uncoated chambered cover glasses at a concentration of 10^5 cells/ml. Further sample preparation was similar to those of imDCs, but RPMI was replaced by IMDM. All incubation steps were performed at 37 °C.

Cellular Imaging

Experiments were performed on a single molecule detection sensitive dual-color excitation / emission epi-fluorescence microscope which has been described in chapter 2. Samples were excited with one or two gated laser excitation sources. For each frame, the pulse length and power density were set to 4ms, $\sim$1kW/cm^2 for the 633nm HeNe laser and 2ms, $\sim$2kW/cm^2 for the 514.5nm line of an Ar^+Kr^+ laser. Fluorescence was collected with a 60x TIRFM objective, filtered and projected onto an Intensified CCD camera. The frame rate was 20Hz. Typical position accuracies were $0.046\mu m$ for both Atto647N and Atto520 labeled LFA-1 molecules on the membrane of live cells. The dorsal side of the cell was brought into focus by DIC (Differential Interference Contrast) enhanced bright field imaging. Experiments were performed at 37 °C.

Single Dye Tracing and analysis of square displacements

SDT techniques and analysis of square displacements have been described in chapter 2. Briefly, two dimensional trajectories in the plane of focus were reconstructed by the aid of colloidal particle tracking software [171], which has been modified and implemented for tracing of fluorescently marked individual nanoclusters on living cells. MSD (mean square displacement) curves were generated for every single trajectory with a minimum length of 13 frames. The short timelag diffusion coefficient D was retrieved by linear fitting (first 3 or 4 points of the MSD plot for a trajectory length of $\geq$13 or $\geq$21 frames respectively). Finally, a semi-logarithmic histogram of D for individual LFA-1 nanoclusters was generated.

CPD (Cumulative Probability Distribution) analysis [158] was further used to identify and characterize different mobility subpopulations within the mobile fraction of the trajectories ($D \geq D_{th}$). For CPD analysis, trajectories ≥ 21 frames were selected, resulting in $D_{th} = 0.006\mu m^2/s$ (see 2.3). One or two components were identified in the mobile fraction and their square displacement curves were retrieved. Fit parameter f corresponds to the slow diffusing part of the mobile fraction (in case 2 components were identified). Square displacement curves were fitted with an anomalous diffusion representing function: $r(t)^2 = \Gamma \cdot t^{\alpha} + {\Delta_0}^2$ [131], where $r(t)^2$ is the square displacement of the component in question at time lag t, Γ is the transport coefficient, α is the anomalous parameter and ${\Delta_0}^2$ is the square displacement offset at $t = 0$. In addition, square displacement curves were also fitted with a linear function through the first four points to obtain the short timelag diffusion coefficient (D) of the retrieved components. The component with the lowest D was defined as the 'slow' mobile subpopulation and the other component was defined as the 'fast' mobile subpopulation.

Finally, the immobile, slow and fast mobility subpopulations were quantified (% of the total number of trajectories). For that, the immobile subpopulation has been estimated by scaling the histogram of D of immobile nanoclusters on fixed cells to the first bar ($D < 0.001\mu m^2$) in the histogram of the experimental dataset. Then, the average of the fit parameter f was used to determine the percentages of the slow and fast mobile subpopulations. Error bars represent the approximated standard deviation of the mobility subpopulation in question. Significance levels were derived using the single sided two-sample z-test.

Single trajectory transient confinement detection

A software dedicated to the detection of transient confinement was implemented according to the method described by Simson et al. [133]. Shortly, a trajectory is classified as 'transiently confined' if it contains periods in which the probe remains in a specific membrane area considerably longer than a Brownian diffusant would stay in an equally sized region. Algorithm parameters are described in 3.2. Trajectories with a minimum length of 61 frames were screened.

5.3 Results

5.3.1 LFA-1 trajectories on monocytes, imDC and T cells.

In order to compare LFA-1 mobility on imDCs, resting T cells and resting monocytes, we generated individual trajectories of TS2/4 and L16 epitopes on the dorsal side of these cell types. On imDCs, LFA-1 mobility was monitored during day 4-10 after initiation of differentiation of monocytes. Compared

to monocytes, expression of the L16 LFA-1 epitope is low on imDCs and T cells (see 5.3.5 and [3]). Nevertheless, single molecule detection sensitive epi fluorescence microscopy enabled us to monitor both TS2/4$^+$ and L16$^+$ LFA-1 on these cell types. Suitable movies for SDT were selected and trajectories were generated. Figure 5.1 shows brightfield images of a typical imDC, T cell and monocyte, together with representative trajectories of L16 labeled LFA-1 found on these cell types. By visual inspection of trajectories no major differences can be observed between monocytes and imDCs. In contrast, on resting T cells LFA-1 trajectories clearly explore a larger spatial area compared to imDCs and monocytes. In the following sections a detailed analysis of the obtained trajectories will follow in order to investigate LFA-1 mobility on imDCs and to compare found results with those obtained for monocytes and T cells.

$< r^2 >= \Gamma t^\alpha + \Delta_0$	Γ (TS2/4)	α (TS2/4)	Γ (L16)	α (L16)
day4	0.091 ± 0.001	0.82 ± 0.02	0.097 ± 0.001	0.88 ± 0.01
day5	0.075 ± 0.001	0.83 ± 0.02	0.057 ± 0.0002	0.80 ± 0.01
day6	0.10 ± 0.002	1.00 ± 0.02	0.083 ± 0.0003	0.84 ± 0.01
day7	0.083 ± 0.001	0.95 ± 0.02	0.067 ± 0.0004	0.81 ± 0.01
day8	0.076 ± 0.001	0.81 ± 0.02	0.070 ± 0.0002	0.87 ± 0.01
day9	0.11 ± 0.002	1.00 ± 0.02	0.100 ± 0.0004	1.1 ± 0.01
day10	0.081 ± 0.001	0.94 ± 0.01	0.11 ± 0.0003	0.99 ± 0.01

Table 5.1. *The mobile fractions of TS2/4 and L16 epitope subpopulations of day 4-10 after differentiation have been analyzed by means of the MSD of the sum of the trajectories. For TS2/4 and L16 respectively, trajectories with a minimum length of 13 and 21 frames and a diffusion constant $D_{th} \geq 0.01\mu m^2/s$ and $D_{th} \geq 0.006\mu m^2/s$ respectively were selected. Found MSD plots were fitted with an anomalous diffusion representing function. The fit length was 12 and 24 for TS2/4 and L16 respectively. The fit parameters Γ and α were retrieved together with their errors. $\chi^2_{red} < 1$ for all fits.*

5.3.2 LFA-1 mobility as a function of DC maturation.

The process of differentiation of monocytes towards imDCs takes several days. Therefore, we inquired whether LFA-1 mobility on imDCs would be time dependent and we analyzed LFA-1 mobility at different days during differentiation. Figure 5.2 shows the distributions of diffusion constants of TS2/4 (a) and L16 (b) labeled LFA-1 for three representative days after initiation of differentiation. A significant decrease of the immobile subpopulation of the L16 epitope can be observed between day 4 and day 5-8 (compare bar $D \leq 0.001\mu m^2/s$ of day 4 in fig. 5.2 and of day 5-8 in fig. 5.3, 11% and 3.3% respectively, $p < 0.02$), suggesting that on day 4 monocytes are not completely differentiated into imDCs yet.

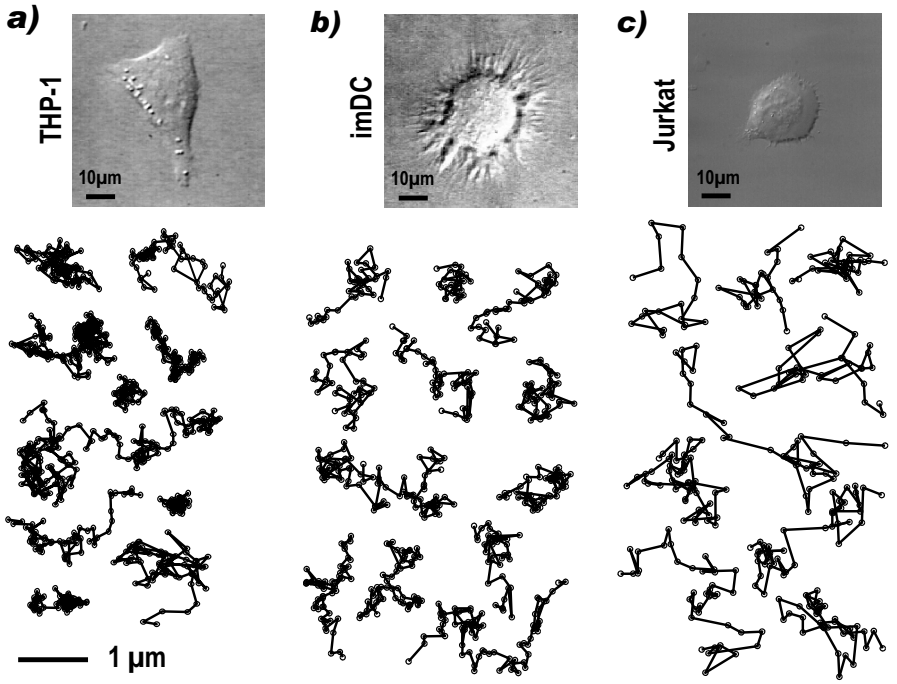

Figure 5.1. *Mobility of L16$^+$ LFA-1 on monocytes, imDCs and T cells. Above: brightfield images were obtained using DIC. Below: Representative trajectories of L16$^+$ LFA-1 on each cell type.*

The position and height of the peak in the diffusion histogram changes per day. To investigate the type of mobility as a function of time, we calculated the cumulative MSD (mean square displacement) for trajectories in the mobile fraction per epitope per day. The MSD was fitted with a fit function for anomalous diffusion as described for the CPD analysis and fit parameters were retrieved, see table 5.1. From this analysis we did not observe any significant difference in both the transport coefficient Γ or the values of the anomalous parameter α as they remained fairly similar for both TS2/4 and L16 independent of the differentiation day.

Altogether, the results above show that LFA-1 mobility is stable in between day 5-8.

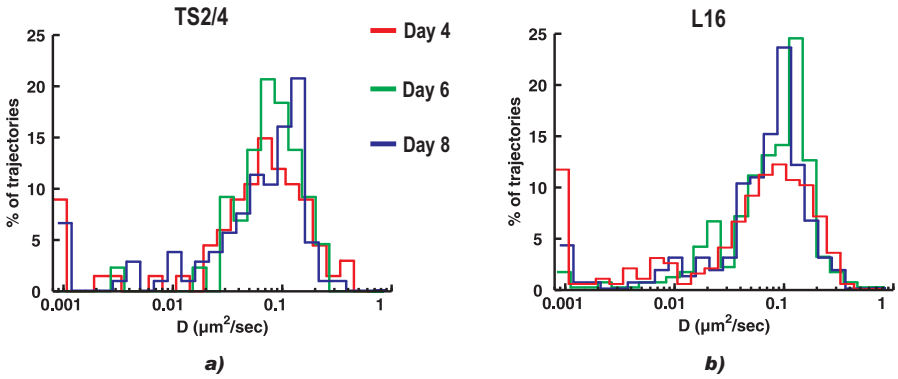

Figure 5.2. *The distributions of diffusion constants of TS2/4 (a) and L16 (b) labeled LFA-1 on imDCs measured at day 4, 6 and 8 after initiation of differentiation. The minimum trajectory length was set at 13 frames. The histograms were normalized to the total number of trajectories (TS2/4: 67, 44 and 107 trajectories from 6, 5 and 12 cells for day 4, 6 and 8 respectively; L16: 201, 210 and 172 from 6, 10 and 11 cells for day 4, 6 and 8 respectively).*

5.3.3 Diffusion constants of LFA-1 on imDCs increased twofold compared to monocytes.

Since no significant differences in diffusion were observed on imDCs as a function of differentiation day, individual LFA-1 trajectories from day 5-8 were taken together for detailed analysis and distributions of short time lag diffusion constants were generated (fig. 5.3). The distributions of diffusion constants of the TS2/4 (a) and the L16 (b) epitope show resemblance with those generated for monocytes: they are equally broad and have a main mobile population with a small shoulder on the low diffusion side. However, a clear shift of the whole distribution of LFA-1 on imDCs to approximately twofold larger diffusion constants was observed compared to the distribution on monocytes. Moreover, the immobile subpopulation of the L16 epitope reduced by fourfold ($p = 0.00003$).

5.3.4 Immature DCs show three LFA-1 mobility subpopulations

To investigate if LFA-1 mobility subpopulations were conserved upon differentiation towards imDCs and to compare their long term diffusion behavior with monocytes, we applied CPD analysis on the mobile fractions of the TS2/4 and L16 epitope trajectory datasets.

The constructed CPDs were then fitted with functions representing one and two diffusing components. CPD analysis using a 2-component function resulted

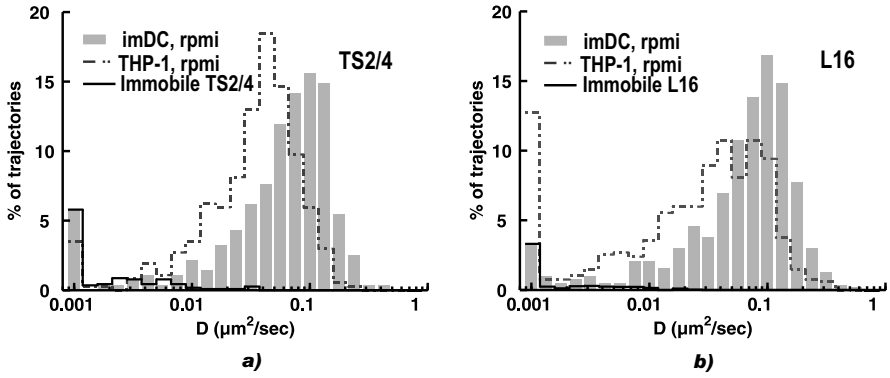

Figure 5.3. *The distributions of diffusion constants (bars) of TS2/4 (a) and L16 (b) labeled LFA-1 on imDCs measured at day 5-8 after initiation of differentiation. Dotted envelope lines: distributions of diffusion constants of LFA-1 nanoclusters on monocytes. Black envelope lines: estimated distributions of the immobile subpopulations on imDCs. The histograms were normalized to the total number of trajectories in each dataset (TS2/4: 276 trajectories from 32 cells; L16: 635 trajectories from 41 cells).*

in better fitting compared to a 1-component function: the mean square of the residuals showed a 9- and 127-fold reduction for TS2/4 and L16 respectively. We concluded that there were at least two subpopulations present in the mobile fractions of both epitopes and proceeded the analysis with a 2-component fit function.

Square displacement plots and obtained parameters from linear and anomalous fit functions are presented in figure 5.4 and table 5.2. For the TS2/4 epitope, random diffusion (α close to 1) can be observed in both mobility subpopulations. For the L16 epitope, the fast mobile subpopulation reveals mobility which is close to the random type, while the slow mobile subpopulation reveals anomalous mobility. These results are qualitatively similar to those observed on monocytes. However, the diffusion constants of the TS2/4 mobility subpopulations increased almost twofold compared to monocytes. Interestingly, the diffusion constants found for the L16 epitope barely differ from observations on monocytes: the diffusion constant of the slow mobile subpopulation is similar and the diffusion constant of the fast mobile subpopulation increased by approximately 25%.

The relative contribution of the different mobility subpopulations exhibited by the TS2/4 and the L16 epitopes expressed on imDCs is shown in fig. 5.5. In both epitopes, the fast mobile subpopulation is dominant and a smaller slow

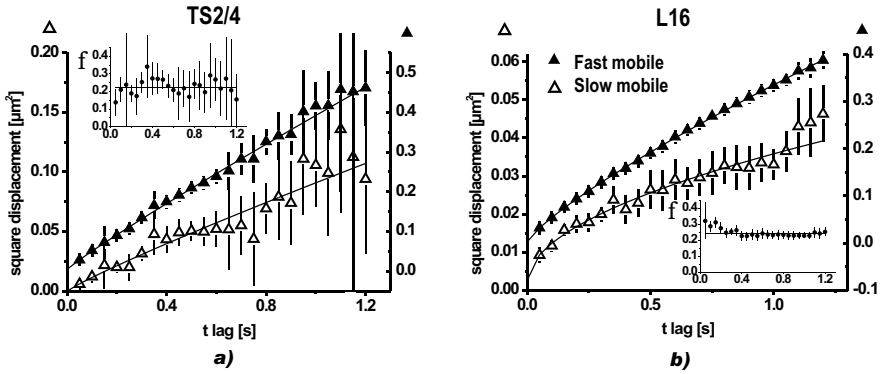

Figure 5.4. *The mobile fractions of TS2/4 (a) and L16 (b) epitopes on imDCs of day 5-8 have been analyzed by means of the CPD method. Presented square displacement plots of slow mobile (left y-axis, open triangles) and fast mobile (right y-axis, closed triangles) subpopulations have been fitted with an anomalous diffusion representing function. The fit parameters and their errors (standard deviation) are presented in table 5.2. Fits were performed on 24 points. The size of the slow component with respect to the total mobile fraction is expressed as fraction f (inset); f=0.23 ± 0.04 for TS2/4 and f=0.24 ± 0.02 for L16. Error bars:* $2 \cdot \sigma$.

$< r^2 >= \Gamma t^{\alpha} + \Delta_0$	α_{slow}	α_{fast}	f
TS2/4 THP-1	0.86 ± 0.2	0.94 ± 0.06	0.30 ± 0.05
TS2/4 imDC	0.90 ± 0.09	0.93 ± 0.02	0.23 ± 0.04
L16 THP-1	0.49 ± 0.06	0.91 ± 0.02	0.33 ± 0.03
L16 imDC	0.53 ± 0.09	0.81 ± 0.01	0.24 ± 0.02

$< r^2 >= 4Dt + \Delta_0$	D_{slow} $[\mu m^2/s]$	D_{fast} $[\mu m^2/s]$	pnts
TS2/4 THP-1	0.014 ± 0.005	0.056 ± 0.006	3411
TS2/4 imDC	0.024 ± 0.009	0.100 ± 0.004	2854
L16 THP-1	0.017 ± 0.001	0.081 ± 0.001	12627
L16 imDC	0.015 ± 0.002	0.104 ± 0.004	12399

Table 5.2. *CPD analysis of the mobile fractions of TS2/4 and L16 epitopes on imDCs of day 5-8. The fit parameters D and* α *were retrieved together with their errors. Furthermore, fraction f and the number of points of the CPD (at a time lag of 3 frames) are presented. The anomalous diffusion fits were done on 24 points, the linear fits were done on 4 points. The* χ^2_{red} *values of the fit functions were <0.24.*

mobile subpopulation is present. The results of the TS2/4 epitope on imDCs do not show significant differences compared to the results from monocytes. On the other hand, the L16$^+$ immobile subpopulation reduced by fourfold

($p = 0.00003$) at the benefit of the fast mobile subpopulation ($p = 0.002$). On

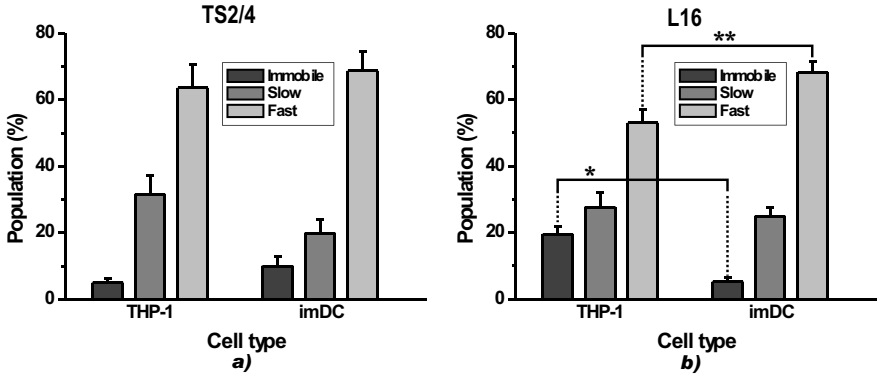

Figure 5.5. *Percentages of the immobile, slow mobile and fast mobile subpopulations have been quantified for the TS2/4 and L16 epitope subpopulations of LFA-1 on imDCs and compared to monocytes. Error bars represent the standard deviation.* $* \; p < 0.00003$, $** \; p = 0.002$

resting monocytes, the immobile subpopulation of active LFA-1 is related to the extended open headpiece conformation of LFA-1 (chapter 3 and 4). Assuming this is also true for imDCs, the results described above indicate that the ratio between extended open headpiece and extended LFA-1 is reduced on imDCs with respect to resting monocytes.

Interestingly, we also observed that $8 \pm 3\%$ of the L16$^+$ trajectories exhibited transient confinement. In a dataset of simulated random diffusing trajectories with an average length of 200 frames, only $1 \pm 0.5\%$ were classified as transient confined. According to the single sided two-sample z-test, $p < 0.05$ for the difference between the detected transient confinement in the measured and simulated dataset. Surprisingly, the found percentage of transient confinement is equal to the percentage observed on resting monocytes ($9 \pm 3\%$), despite the reduced immobile subpopulation observed for L16$^+$-LFA-1.

Altogether, these results show that the overall LFA-1 population on imDCs has equally sized mobility subpopulations and a similar type of diffusion (Brownian), but diffuses faster than LFA-1 nanoclusters on the cell membrane of monocytes. On the other hand, the fraction of L16$^+$-LFA-1 shows almost similar diffusion values compared to monocytes suggesting that determinants regulating active LFA-1 mobility on the cell membrane are preserved on monocytes and imDCs. Also similar to monocytes, a small fraction of L16$^+$ LFA-1 shows transient confinement. However, our results also indicate that L16$^+$-LFA-1 on imDCs contains a smaller fraction of cytoskeleton-tethered LFA-1

with the extended open headpiece conformation compared to monocytes, which is in line with the reduced LFA-1-ligand binding capacity observed on imDCs compared to monocytes [3].

5.3.5 The diffusion constant of LFA-1 on imDCs is reduced compared to T cells

To investigate LFA-1 mobility in relation to cell type, we studied LFA-1 mobility on resting T cells. β_2-integrin mobility has been studied before on lymphocytes by FRAP [28, 195] and SPT [34, 184, 28], although depending on the method and experimental conditions, different absolute values were found for the diffusion constants. Figure 5.6 shows the distribution of diffusion constants of

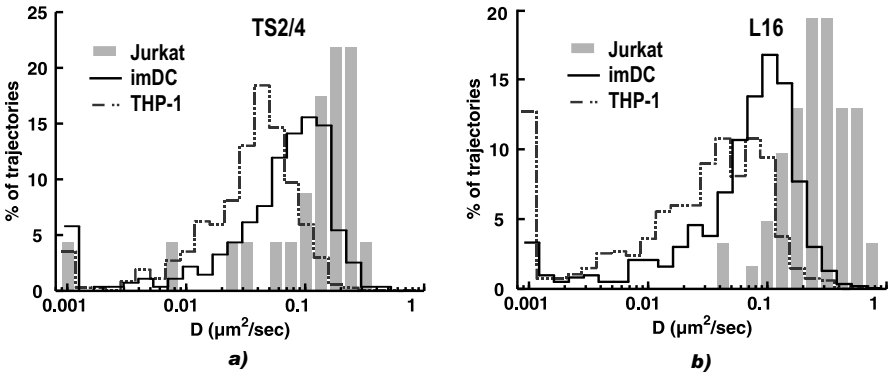

Figure 5.6. *The distributions of diffusion constants of TS2/4 (a) and L16 (b) labeled LFA-1 on T cells (bars). Dotted envelope lines: distribution of diffusion constants of LFA-1 nanoclusters on monocytes. Black envelope lines: distribution of diffusion constants of LFA-1 nanoclusters on imDCs. TS2/4: 23 trajectories from 16 cells from three experiments; L16: 62 trajectories from 13 cells from two experiments.*

trajectories retrieved from TS2/4 and L16 labeled T cells. The distributions of diffusion constants of TS2/4 and L16 labeled LFA-1 on T cells is much narrower and shifted to larger D values with respect to the distributions of diffusion constants of LFA-1 on imDCs. Furthermore, the immobile subpopulation of L16 labeled T cells is completely absent. To determine the average diffusion constant of LFA-1 on T cells, we derived the cumulative MSD of the mobile fraction of the trajectories of both the TS2/4 and the L16 epitopes. Results are presented in table 5.3. The diffusion constants of the TS2/4 and L16 epitopes on T cells are 1.7 and 3.6 times respectively larger than the values

found for imDCs.

$< r^2 >= 4Dt + \Delta_0$	D [$\mu m^2/s$] (TS2/4)	D [$\mu m^2/s$] (L16)
Jurkat	0.16 ± 0.007	0.330 ± 0.002
imDC	0.095 ± 0.001	0.092 ± 0.001

Table 5.3. *Cumulative MSD analysis of the mobile fractions of the TS2/4 and L16 epitopes on T cells compared with imDCs of day 5-8. The fit parameter D was retrieved together with its error. Linear fits were performed on the first 4 points of the MSD plot. The χ^2_{red} values of the fit functions were < 1.5 for L16 labeled imDCs and < 0.52 for all other curves.*

Compared to FRAP measurements on Jurkat T cells [28], we found a 3.5- to 7.2-fold increase of D (depending on the antibody). This discrepancy can be understood by the lower spatio-temporal resolution of FRAP compared to SDT: since FRAP operates over longer distances and at longer time scales, hindered diffusion becomes more apparent and probed diffusion constants will be reduced with respect to those determined by SDT [206]. The mobile fraction of the overall LFA-1 population on resting T cells indeed shows anomalous diffusion ($\alpha = 0.7 \pm 0.1$, results not shown).

Compared to SPT results, using SDT we found a twofold larger average diffusion constant for LFA-1 on resting Jurkat T cells [28]. Furthermore, trajectories retrieved by SPT showed a 3-fold wider distribution of diffusion constants compared to trajectories obtained by us using SDT. These differences can be explained by different experimental conditions used for SPT. Used micrometer-sized beads show a reduced specificity (5-10-fold specificity with respect to isotype control [28]) and affinity compared to molecular sized probes. Furthermore, the large size of the marker particles may lead to cross-linking of the tracked molecules [150]. In addition, SDT trajectories are much shorter in time, reducing the probability that multiple modes of motion are present in a single trajectory. If an individual trajectory is transiently confined, the MSD of the total trajectory will show a reduced D compared to the D obtained from the mobile part only, broadening the distribution of diffusion constants of mobile trajectories. Indeed, transient confinement has been observed in LFA-1 trajectories on T cells retrieved by SPT [167].

5.4 Discussion

In chapters 3 and 4 we demonstrated that LFA-1 mobility is dependent on the conformational state of LFA-1. The balance between conformational states of LFA-1 on the cell surface was shifted towards the extended open headpiece conformation upon reduction of extracellular Ca^{2+} levels or upon interaction with ICAM-1 coated surfaces. These changes in conformational state were

directly accompanied by a massive reduction of LFA-1 mobility on the cell surface. In chapter 3 it was also demonstrated that microclustering induced by co-grabbing nanoclusters with secondary antibodies or by ICAM-1 ligation strongly reduced LFA-1 mobility. The data presented in this chapter demonstrates how other mechanisms besides conformation influence LFA-1 mobility. One of these mechanisms is the organization of LFA-1 and its direct microenvironment at the nanometer scale, as will be explained below. Furthermore, comparison of imDCs with monocytes versus T cells indicates that the local membrane viscosity probed by LFA-1 is strongly cell type specific.

Like on monocytes, imDCs display different mobility profiles with immobile, slow mobile and fast mobile subpopulations. The total LFA-1 population revealed random diffusion in both mobility subpopulations. In contrast, extended LFA-1 showed anomalous (slow subpopulation) and random diffusion (fast subpopulation). These results are qualitatively similar to those obtained on monocytes, except that the diffusion constants of the total LFA-1 population on imDCs increased twofold compared to monocytes. Furthermore, the immobile subpopulation of extended LFA-1 was strongly reduced with respect to monocytes.

The alterations of percentages of mobility subpopulations on imDCs with respect to monocytes (the $L16^+$ immobile subpopulation reduced fourfold) can be explained by the overall reduced activation state of LFA-1 upon differentiation of monocytes towards imDCs [3]. In chapter 3 and 4, we proposed that the immobile nanoclusters could be related to cytoskeleton tethered LFA-1 with the extended, open headpiece conformation [193, 4, 192, 195]. Reduction of the activation state of the LFA-1 molecules or nanoclusters should reduce the immobile subpopulation, which is indeed observed here. Furthermore, at day 4 after initiation of differentiation we observed a larger L16 epitope immobile subpopulation compared to later days, suggesting a graduate decrease of the LFA-1 activation state upon cell differentiation.

Compared to monocytes, D_{slow} and D_{fast} of the overall (TS2/4 labeled) LFA-1 population doubled while D_{slow} and D_{fast} of the (L16 labeled) extended LFA-1 fraction only increased slightly. We questioned whether this increase in mobility could be assigned to a loss of nanoclustering. The approximate size of a LFA-1 nanocluster on a monocyte is 150nm [3] and the size of a single LFA-1 molecule is roughly 10nm [48]. Therefore, the size of the diffusing object decreased approximately by 15-fold. Since the LFA-1 diffusion increased by a factor two, a model showing a weak dependence between these two factors could explain our observations, as discussed below.

The mobility of objects in biological membranes has been studied in multiple theoretical and experimental studies [205, 135, 231]. Kucik et al. [205] classified the different models explaining the mobility of a diffusing object in a

membrane in three categories. First, in the diffusion barrier model diffusion of membrane proteins are restricted by microcorrals underneath the membrane, or by anchored protein-pickets [64, 68]. Second, in the transient binding model, the diffusion of membrane proteins is reduced by transient binding at a time scale beyond the resolution of conventional tracking techniques. In the third model simple viscous resistance to membrane protein motion might slow diffusion on the micro scale. The diffusion barrier and transient binding models predict a strong dependence between the diffusant size and its diffusion constant and are therefore inconsistent with our data [205, 231]. On the other hand, our data on the overall LFA-1 population is in favor of the viscous resistance model, since it is predicting a weak dependence between the size of the diffusant and its diffusion constant D, as is shown below.

According to hydrodynamic theory, the diffusion constant D of an impermeable cylinder in an infinite, continuous sheet varies as the logarithm of the radius of this cylinder [162]. For a cylinder of radius R and height h, moving in a membrane with viscosity μ and height h, with both surfaces in contact with a less viscous (aqueous) phase with viscosity μ', the translational diffusion constant D of the cylinder will be:

$$D = (K_b T/4\pi\mu h)(ln(\mu h/\mu' R) - y) \tag{5.1}$$

Where K_b is the Boltzmann constant, T is the absolute temperature and y is Euler's constant. The weak dependence between D and R in this model is consistent with the shift in diffusion constants observed between the overall LFA-1 population on monocytes and imDCs, assuming that μ is equal for both monocytes and imDCs. The diffusion constants for individual LFA-1 molecules and LFA-1 nanoclusters were calculated as a function of μ. The viscosity μ' of the aqueous surrounding medium was set to 0.01 poise, h was set to 10^{-7}cm and $K_b T = 4 \cdot 10^{-14}$erg [162]. R was set to half of the size of individual and nanoclustered LFA-1. We determined the viscosity μ which gave the maximum correlation between predicted and experimental diffusion constants of clustered and single LFA-1 molecules. For the overall LFA-1 population we found $\mu = 237$, predicting $D_{single} = 0.097\mu m^2/s$ and $D_{cluster} = 0.060\mu m^2/s$, correlating with the observed short time lag diffusion constants of the fast mobile subpopulations on imDCs and monocytes respectively. Furthermore, we found $\mu = 1194$, predicting $D_{single} = 0.024\mu m^2/s$ and $D_{cluster} = 0.016\mu m^2/s$. These diffusion constants correlate well with the short time lag diffusion constants of the slow mobile subpopulations observed for the overall LFA-1 population on imDCs and monocytes.

Our results are in line with the work of Kucik et al., where hydrodynamic modeling also correlated with observed cluster size dependent diffusion of glycoprotein aggregates on cells, if a much greater viscous resistance at the microscale was assumed ($\mu \sim 100$ poise) compared to values found for unobstructed

diffusion of protein molecules embedded in a lipid bilayer ($\mu \sim 2$ poise) [205]. They explained this so-called high "apparent viscosity" by a combination of factors, like the amount of proteins in the membrane (i.e., excluded area effect, interactions among the glycoproteins themselves) and the effect of interactions with structures exterior to the membrane (i.e., steric effects of glycosyl moieties on the external surface of the cell, or inelastic interactions with the cytoskeleton inside the cell). Furthermore, the effects at a distance of both mobile and immobile membrane proteins on a diffusing "tracer" molecule can be of strong influence on membrane viscosity (i.e., the drag exerted by immobile particles in an intervening fluid) [205].

The effect of immobile membrane proteins on a diffusing molecule or nanocluster might explain the difference in "apparent viscosity" between the slow and fast mobile LFA-1 subpopulations in our data. High resolution microscopy showed that, regardless of the LFA-1 conformational state, a fraction of LFA-1 nanoclusters resides in close proximity of GPI anchored proteins (GPI-AP), which are organized in so-called "hot spots" on the cell membrane [77]. This fraction of $\sim 25\%$ of LFA-1 might represent the slow mobile subpopulation. In order to maintain GPI-AP organization on the membrane, GPI-AP should either be actively transported towards "hot spots" or, GPI-AP inside these "hot spots" should be restricted or immobilized by cytoskeletal structures [232, 86]. In the latter case, their reduced mobility can have a strong effect on the "apparent viscosity" of LFA-1 molecules or nanoclusters in their direct vicinity, regardless of the integrin conformational state and regardless of binding. Hotspots of GPI-AP might trap LFA-1 due to their high "apparent viscosity", slowing down LFA-1 diffusion inside these nascent adhesion sites. Consequently, interaction with LFA-1 related molecules might increase. Further investigation is required to validate this hypothesis.

In order to apply hydrodynamic theory to our data, a similar membrane viscosity μ for both nanoclustered and individual LFA-1 molecules, on both resting monocytes and imDCs was assumed. Despite this crude simplification, the predicted relation between diffusant size and diffusion constants matched our experimental results for the overall, predominantly inactive LFA-1 population on resting monocytes and imDCs. The match between hydrodynamic theory and our data implies that LFA-1 diffusion constants are determined by viscous resistance rather than by transient binding to proteins. Indeed, since the majority of LFA-1 on monocytes and imDCs is in a low affinity conformation [3], little binding activity between LFA-1 and related proteins is expected. Furthermore, we observed random diffusion of LFA-1 in both slow and fast mobility subpopulations on both cell types, also indicating that relatively little binding between LFA-1 and other proteins occurred.

However, hydrodynamic theory fails to explain the difference in $L16^{+}$-LFA-1 diffusion constants observed on monocytes and imDCs (no significant difference

between the slow, $\sim$ 1.25-fold difference between the fast mobile subpopulations respectively). Our observations seem to suggest an even weaker relation between probe size and diffusion constant, compared to what has been predicted by hydrodynamic theory. In fact, all three models for membrane diffusion (diffusion barrier, transient binding and viscous resistance model) seem to fail in their prediction of the observed $L16^+$-LFA-1 diffusion constants. Therefore, our results are more consistent with the assumption that the majority of the $L16^+$-LFA-1 remained nanoclustered upon differentiation towards imDCs. Since the amount of $L16^+$-LFA-1 is strongly reduced upon differentiation, prevailed $L16^+$ nanoclusters might have remained unnoticed.

The persistence of the LFA-1 mobility subpopulations and their "apparent viscosity" upon differentiation of monocytes into imDCs, indicates that the local micro-environment of LFA-1 is conserved on these cell types. Although the spatial organization of LFA-1 is dispersed upon differentiation, our results indicate that a small minority of $L16^+$-LFA-1 remains nanoclustered. Furthermore, the type of diffusion of LFA-1 subpopulations did not seem to change upon differentiation. Therefore, it is tempting to believe that imDCs are still potentially active and might be able to switch to an active state where LFA-1 mediated adhesion is required, which is in line with recent studies on the role of LFA-1 in DCs [15, 16, 18, 227].

We also compared LFA-1 mobility on imDCs with resting T cells to investigate the role of cell type specific differences in LFA-1 mobility. Since T cells are a completely different cell type, LFA-1 mediated adhesion takes place in a different context and with different spatio-temporal characteristics compared to imDCs. On the other hand, like imDCs, resting T cells also show a reduced LFA-1 activation state with respect to monocytes [228, 30, 79] and conformation-related differences in LFA-1 mobility were expected to be minimum between both cell types. Like imDCs, our data for T cells shows a small or even absent L16 positive immobile subpopulation. Since the immobile subpopulation of extended LFA-1 can be related to the high affinity form of LFA-1 [28, 193, 4, 192, 195], we assume that the overall LFA-1 population indeed has a comparable low affinity on both cell types. Therefore we postulate that the observed differences in LFA-1 mobility between both cell types do not primarily originate from differences in the conformational state of LFA-1.

Compared to T cells, imDCs reveal a much wider distribution of diffusion constants which are shifted to two- to fourfold lower values. The observed differences between the found diffusion constants on both cell types cannot be explained by differences in valency either, since LFA-1 molecules are already distributed in single molecules over the cell membrane of imDCs and diffusion constants cannot increase further by reduction of valency. The much broader

distribution of imDCs with respect to T cells can also not be clarified by differences in valency. If LFA-1 would be more organized on the cell membrane of T cells compared to imDCs, a variety of cluster sizes would be present. This would induce a broader distribution of diffusion constants, but the opposite has been observed on resting T cells.

In all, the observed differences in LFA-1 mobility between imDCs and resting T cells can neither be explained by affinity nor by valency. Likely, the observed differences are more fundamental and originate from the viscous resistance at the micro-scale experienced by LFA-1 molecules. Thus, imDCs and monocytes have a higher "apparent viscosity" for LFA-1 compared to resting T cells. In addition, while we interpreted the LFA-1 mobility subpopulations observed on imDCs and monocytes as LFA-1 present in distinctive local micro-environments with different "apparent viscosities" (see above), the narrow distribution of LFA-1 diffusion constants suggests a more homogeneous local micro-environment and "apparent viscosity" of LFA-1 on resting T-cells.

5.5 Conclusions

We have presented a detailed study of LFA-1 mobility on imDCs and compared the results with those obtained for resting monocytes and resting T cells. Like on monocytes, imDCs also display immobile, slow mobile and fast mobile subpopulations showing predominantly random diffusion. However, in contrast to monocytes, the distribution of diffusion constants of the total, primarily inactive LFA-1 population is shifted towards larger values. According to hydrodynamic theory [162], this increased mobility correlates well with its change in spatial organization from nanocluster to monomeric [3]. Furthermore, our observations on imDCs and resting T cells show that the immobile subpopulation of active LFA-1 is strongly reduced compared to monocytes, indicating that these cell types barely express cytoskeleton tethered, open headpiece conformation LFA-1. Here we demonstrated that besides affinity, also changes in the nano-scale organization of LFA-1 influence its lateral mobility. In addition, we showed that differences in the viscous resistance at the micro-scale experienced by LFA-1 are a likely explanation for the observed differences in LFA-1 diffusion constants between imDCs and resting T cells and, between slow and fast mobility subpopulations.

Chapter 6

General Discussion and Future Prospectives

The overall objective of this research has been to investigate the lateral mobility of the integrin receptor LFA-1. By using single molecule techniques, we have been able to deepen our understanding of LFA-1 mobility and its consequences on LFA-1 affinity and avidity regulation on THP-1 monocytes (monocytes) and immature dendritic cells (imDCs). This chapter will integrate the experimental results described in this work, bring them in a broader framework of existing studies and provide directions for future research.

6.1 Observation and analysis of protein mobility of membrane biomolecules

With the development of SPT (Single Particle Tracking, [123]) and ultimately SDT (Single Dye Tracing, [136]), it is now possible to follow the mobility of individual biomolecules on the plasma membrane of living cells, thereby providing new information which is generally hidden in the ensemble-averaged signals of molecules. With these state-of-the-art techniques at hand, membrane organization and interaction between biomolecules can be probed at the single molecule level with high spatio-temporal resolution. We chose SDT to study the mobility of LFA-1 nanoclusters and single molecules on the membrane of live cells. Due to the inherently small size of the probes used for SDT, the technique does not suffer from the major drawbacks of SPT (i.e., potential crosslinking artifacts and additional hindrance) [135, 233]. Furthermore, due to the single molecule approach, a wealth of possibilities of probing the nano-environment are inherited from the single molecule field [136].

Currently, the ability of the SDT technique to analyze the nano environment of a *single* biomolecule is limited by the finite amount of photons a probe can emit before photodissociation. Consequently, a tradeoff needs to be made between localization accuracy, tracing time and frame rate. However, high demands are required for all three points if probed biomolecules are in a heterogeneous environment containing i.e., nanometric confinement zones, obstacles and binding sites with high dissociation rates. Nevertheless, in this work it has been shown that using highly stable organic fluorophores like Atto647N, transient confinement can be detected in a small subset of trajectories. To extend the spectrum of detectable transient confinement periods, the nano environment needs to be probed with higher spatio-temporal resolution and therefore fluorophores need to be developed further or alternative probes should be used. Due to their superb quantum efficiency, photo stability, relatively small sizes and commercial availability, quantum dots (QDs) are frequently being used as an alternative to fluorescent dyes [234]. However, despite reproducibility of specifications of commercially available QDs, their size, polyvalency and optical blinking properties are still limiting factors for their applicability in the field of single molecule tracking [235]. Recently, it has been demonstrated that the blinking characteristics of QDs can be overcome without compromising on QD size [236]. Furthermore, protocols are being developed for simple preparation of monovalent QDs with reduced size compared to commercially available QDs [237]. Besides QDs, fluorescent gold dots and nanodiamonds might also provide valuable alternatives for fluorophores in single molecule tracking experiments (as reviewed in Wieser et al. [233]).

Our work demonstrated that the mobility behavior of individual, heterogeneously distributed transmembrane receptor nanoclusters on living cells can

be imaged, traced and analyzed with single molecule detection sensitivity. We achieved this result by applying additional rules eliminating particle positions prone to artifacts i.e., by thresholding interparticle distance. Consequently, areas with a high probe density or a high background are excluded until sufficient bleaching took place. Our method also considered immobile nanoclusters and is therefore complementary to the proposed method of Moertelmaier et al., where labeling stoichiometry is maintained at the price of loosing the immobile fraction of probes [152]. Although our method is capable to monitor heterogeneously distributed proteins on the cell surface, it still requires sublabeling conditions.

The study of dynamic interactions between biomolecules has proven to be very powerful [70, 62] and especially in these studies undiluted labeling is often required to observe interactions between proteins of interest. With the advancement of high spatial resolution microscopy into the time domain (sptPALM, [153]), tracking of dynamic and densely distributed proteins on the cell surface comes into reach. Aside from further development of the technique itself (the excitation time is limited to at least 50ms per frame), advancement of tracking and analysis tools are also required. Recently, a computationally efficient tracking algorithm has been presented dealing with high particle density, particle motion, heterogeneity, temporary particle disappearance, and particle merging and splitting [238]. Altogether, with the advancement of single molecule tracking microscopy and tracking tools, monitoring and analysis of interactions between multiple sets of densely distributed biomolecules with heterogeneous motion comes into reach.

By combining single trajectory [169, 62] with ensemble averaging analysis [158, 178, 164], we were able to construct a robust analysis approach, capable of resolving immobile, slow and fast mobile subpopulations and their respective long term diffusion behavior. However, with the current development of probes for single molecule tracking on live cells, it is likely that the data analysis for SDT will shift to a single trajectory type [123, 132], or even a sub-trajectory type of analysis as used for SPT data [133, 134, 154, 155, 167]. Currently, trajectories obtained with sptPALM are limited by photobleaching to ≤ 100 frames, despite its ability to generate as much trajectories on a single cell as conventional SDT on 10-100 cells [153]. Therefore, the analysis approach described in this work might prove to be useful for the analysis of trajectories obtained with sptPALM. The distribution of individual trajectory diffusion constants and the characterization of long term diffusion behavior of mobility subpopulations can be applied per cell or even per cell area.

Another approach to study the nano-environment of and interactions between highly dynamic and abundant biomolecules at the single molecule level, is FCS [239]. Particularly spot variation FCS allowed the identification of

nanodomains in living cell plasma membranes [239]. Recently, the spatial resolution of FCS has been improved beyond the diffraction limit by combination with excitation through a substrate with nanometric apertures [66], NSOM [240] and STED microscopy [241], enabling indirect visualization of the membrane structure at the nano-level. Since the first two techniques use evanescent axial illumination of fluorescent probes, multichannel excitation can be achieved with practically equal excitation volumes. Therefore, NSOM-FCS and FCS with nanometric apertures are the preferred techniques to be combined with dual-color FCCS (fluorescence cross correlation spectroscopy, [242]) for the study of interactions between highly dynamic and abundant biomolecules at the cell membrane.

6.2 LFA-1 mobility on leukocytes

For the first time, LFA-1 mobility has been investigated in detail on monocytes and imDCs. We demonstrated that on these cell types, LFA-1 is primarily mobile and exhibits slow and fast mobile subsets showing Brownian motion, without interaction to the cytoskeleton and with a small fraction of LFA-1 in the extended conformation. This fraction displays a different mobility profile with immobile cytoskeleton tethered, slow hindered and fast Brownian diffusion. We propose that the subset of immobile, extended LFA-1 exhibits the high affinity (extended open headpiece) conformation and is responsible for the onset of LFA-1 mediated adhesion. In line with the work of others [3, 28, 26], we observed that initial binding is further strengthened by mass-action driven recruitment of mobile LFA-1 nanoclusters to the ligand binding site. Our result questions earlier models of cytoskeletal anchorage of the overall integrin receptor population on resting cells [34, 185, 35, 31] and support more complex models where only a subset of extended LFA-1 is bound to the cytoskeleton [79, 28]. Conformer specific mobility profiles of LFA-1 have been observed before on T cells, where it was found that tethering of LFA-1 to the cytoskeleton was dependent on the conformational state of LFA-1 [28]. Our results are in line with these observations. In addition, we observed a slow mobile subset in the total LFA-1 population of both monocytes and imDCs with a long term diffusion behavior which is distinctive .

Interestingly, slow and fast mobile subpopulations of LFA-1 on monocytes and imDCs were persistent, regardless of the epitope labeled, the lateral organization of LFA-1, disruption of the actin cytoskeleton or extracellular cation conditions. On the other hand, our results on resting T cells suggested the presence of only one mobile subpopulation, which is in line with SPT studies on lymphocytes [34, 28]. Furthermore, our results in chapter 5 indicated that slow and fast mobility subpopulations on monocytes and imDCs could be

originated from differences in the viscous resistance at the micro-scale experienced by LFA-1. Altogether, these results indicate that on monocytes and imDCs, a distinctive LFA-1 micro environment is present, reflected by the additional slow mobile subpopulation. As discussed in chapter 5, this distinctive micro-environment experienced by LFA-1 possibly originates from so-called "hotspots" of GPI-anchored proteins [77]. Their role might be to "trap" LFA-1 in their high-viscosity environment, in order to catalyze reactions between LFA-1 and cytoskeleton related proteins. These interactions might be accelerated by the proximity between LFA-1 and cytoskeleton related proteins in GPI-AP "hotspots". We only observed anomalous diffusion in the extended LFA-1 fraction of slow mobile LFA-1. This observation suggests that only extended LFA-1 in GPI-AP "hotspots" is truly interacting with cytoskeleton related proteins, while the inactive majority of LFA-1 merely experiences increased viscous drag. Trapping of transmembrane receptors in highly viscous membrane areas has been observed before in other systems [135, 231] and enhancement of reaction rates between proteins trapped in nanodomains has been modeled [243]. However, this hypothesis has not been validated for LFA-1 and needs further investigation.

To study the mechanisms behind the slow mobile fraction of LFA-1 and its anomalous or random long term diffusion, dual color experiments are required to monitor binding of and interaction between LFA-1 and related molecules. Simultaneous monitoring of LFA-1 and GPI-anchored proteins can be used to validate the relation between slow mobile LFA-1 and GPI-anchored protein 'hotspots' [77]. Furthermore, the origin of observed transient confinement of $L16^+$-LFA-1 can be investigated by screening for interaction between LFA-1 and candidate molecules. By monitoring of colocalization between LFA-1 and candidate molecules, transient binding periods as short as a few frames can be detected, which is much more sensitive compared to the transient confinement analysis described in chapter 3. Consequently, Monte Carlo simulations can be used to test if a correlation exists between the spectrum of transient binding periods and anomalous diffusion in the slow mobile $L16^+$-LFA-1 subpopulation [244]. Alternatively, conjugates between L16 and the next generation of quantum dots (non-blinking, smaller and monovalent quantum dots, [236, 237]) can be used to monitor $L16^+$-LFA-1 mobility at much higher spatio-temporal resolution.

6.3 Extracellular Ca^{2+} links integrin nanocluster conformation to mobility

We investigated the role of extracellular divalent cations on LFA-1 mobility on resting monocytes and our results indicate that reduction of extracellular Ca^{2+},

but not Mg^{2+}, induces conformational changes in LFA-1 that translate into integrin extension and transmembrane domain separation, leading to increased interactions with cytoskeletal mediators in the direct micro-environment of LFA-1. These results support different perspectives described in literature about the role of extracellular Ca^{2+} on integrin-ligand binding [210, 37, 30]: on one hand affinity is increased, while on the other hand avidity is decreased upon reduction of extracellular Ca^{2+} levels. We investigated the functional implications of these apposing effects of Ca^{2+} on cell adhesion under different shear-flow conditions. We observed that under low shear flow conditions (0.2 dyn/cm^{-2}, see fig. 4.9a), Ca^{2+} dependent avidity synergizes with Mg^{2+} dependent affinity to establish LFA-1 mediated cell binding. Under higher shear flow conditions (0.5 dyn/cm^{-2}, see fig. 4.9b) only affinity seems to play a role. Our results have direct implications for studies where integrin activation is induced by removal of Ca^{2+} because although high affinity forms are generated, this pool of molecules is not able to reach the required avidity, failing to support firm adhesion under low shear flow conditions. Moreover, we showed that the extracellular Ca^{2+} level can be used to differentially tune the balance between affinity and avidity of LFA-1 ligand binding on resting monocytes.

In future research, investigation of LFA-1 mobility can be further extended towards more physiological conditions. Integrins act as mechano-chemical signal converters, sensing forces from the extracellular matrix discharged on the intracellular cytoskeletal structures [226]. However, it remains a mystery how physical and biochemical factors are coupled, and how they are integrated to enable mechanical sensing [245]. Possibly, force-induced signalling processes regulate LFA-1 mobility on a local or global scale at the cell surface, regulating integrin redistribution. By integrating shear flow conditions in the single dye tracing experiments, the effect of shear forces on LFA-1 mobility can be directly monitored. Furthermore, inflammatory cytokines can be incorporated in ICAM-1 functionalized surfaces to study their influence on LFA-1 mobility during leukocyte arrest [35]. Ultimately, the dynamics of LFA-1 during chemotaxis and transendothelial migration can be studied by performing shear flow essays with monocytes adhering to monolayers of endothelial cells [246]. Mapping of different LFA-1 conformations on polarized lymphocytes proved to be a powerful tool in understanding the mechanisms of cell migration during chemotaxis [2, 10]. However, how different LFA-1 conformers become spatially segregated on the cell membrane has not been investigated yet and (restriction of) lateral diffusion might play an important role. In addition, forces generated by cells can be monitored along with integrin mobility by plating cells on ICAM-1 functionalized compliant substrates. Forces exposed on the matrix by migrating cells can be correlated with LFA-1 mobility, to understand how forces exposed to specific cell areas, c.q., filopodia, central area and uropod, might influence the redistribution of LFA-1 among these areas.

6.4 The relation between mobility, micro environment and spatial organization of LFA-1

Upon differentiation of monocytes into imDCs, LFA-1 membrane organization in active and inactive nanoclusters disperses and its affinity reduces [3]. We observed that along these changes, the diffusion constant of the total, primarily inactive LFA-1 population increased by twofold. According to hydrodynamic theory [162], this increased mobility correlates well with its change in spatial organization from nanocluster to monomeric. Thus, we demonstrated that besides affinity, also changes in the nano-scale organization of LFA-1 influence its lateral mobility.

A weak dependence between aggregate size and its lateral diffusion constant in the membrane has been found before on live cells [205]. However, others found a much stronger dependence between the diffusant size and its diffusion constant [247, 231]. These different results show that the relation between diffusant size and its diffusion constant are highly context dependent, c.q., their interactions with-, and binding to the micro- and nano-environment determine the observed relationship. Therefore, it is unlikely that a single model like the diffusion barrier model [64, 68] can explain the reduced diffusion constant of biomolecules on cellular membranes with respect to model membranes.

Interestingly, our observations in chapter 5 suggested that nanoclustering of the reduced fraction of extended LFA-1 is conserved on imDCs. Furthermore, our results indicated that the micro-environment of LFA-1 is also conserved upon differentiation of monocytes into imDCs. These findings imply that LFA-1 is still potentially active on imDCs, which is in line with recent findings about the role of LFA-1 on imDCs [15, 16, 18, 227]. We suggest further investigation into the spatio-temporal characteristics of $L16^{+}$-LFA-1 on imDCs under different biophysical and biochemical stimulating conditions (e.g., force and respectively stimulation by CCL21).

Finally, the mobility of LFA-1 was compared between imDCs and resting T cells. LFA-1 diffusion constants on imDCs were two- to fourfold reduced compared to resting T cells and the distribution of diffusion constants was much broader on imDCs. The observed differences in mobility between both cell types was neither explained by affinity nor by valency. Likely, the observed differences originated from the viscous resistance at the micro-scale experienced by LFA-1 molecules at different locations on the cell membrane, on different cell types. These results illustrate the spatio-temporal heterogeneity of LFA-1 adhesion regulation at the cell membrane, which is tailored to its cell type and extracellular environment.

Bibliography

[1] Delves, P., S. Martin, D. Burton, and I. Roitt, 2006. Roitt's essential immunology. Blackwell Publishing Ltd.

[2] Smith, A., P. Stanley, K. Jones, L. Svensson, A. McDowall, and N. Hogg, 2007. The role of the integrin lfa-1 in t-lymphocyte migration. *Immunological Reviews* 218:135–146.

[3] Cambi, A., B. Joosten, M. Koopman, F. de Lange, I. Beeren, R. Torensma, J. A. Fransen, M. Garcia-Parajo, F. N. van Leeuwen, and C. G. Figdor, 2006. Organization of the integrin LFA-1 in nanoclusters regulates its activity. *Mol. Biol. Cell* 17:4270–4281.

[4] Luo, B. H., C. V. Carman, and T. A. Springer, 2007. Structural basis of integrin regulation and signaling. *Annu. Rev. Immunol.* 25:619–647.

[5] Kong, F., A. J. Garca, A. P. Mould, M. J. Humphries, and C. Zhu, 2009. Demonstration of catch bonds between an integrin and its ligand. *J. Cell Biol.* 185:1275–1284.

[6] Hynes, R. O., 2002. Integrins: bidirectional, allosteric signaling machines. *Cell* 110:673–687.

[7] Harris, E. S., T. M. McIntyre, S. M. Prescott, and G. A. Zimmerman, 2000. The leukocyte integrins. *J. Biol. Chem.* 275:23409–23412.

[8] Springer, T. A., 1990. Adhesion receptors of the immune system. *Nature* 346:425–434.

[9] Shamri, R., V. Grabovsky, J.-M. Gauguet, S. Feigelson, E. Manevich, W. Kolanus, M. K. Robinson, D. E. Staunton, U. H. von Andrian, and R. Alon, 2005. Lymphocyte arrest requires instantaneous induction of an extended LFA-1 conformation mediated by endothelium-bound chemokines. *Nat. Immunol.* 6:497–506.

[10] Shulman, Z., V. Shinder, E. Klein, V. Grabovsky, O. Yeger, E. Geron, A. Montresor, M. Bolomini-Vittori, S. W. Feigelson, T. Kirchhausen, C. Laudanna, G. Shakhar, and R. Alon, 2009. Lymphocyte crawling and transendothelial migration require chemokine triggering of high-affinity LFA-1 integrin. *Immunity* 30:384–396.

[11] Salas, A., M. Shimaoka, A. N. Kogan, C. Harwood, U. H. von Andrian, and T. A. Springer, 2004. Rolling adhesion through an extended conformation of integrin alpha(l)beta(2) and relation to alpha i and beta i-like domain interaction. *Immunity* 20:393–406.

[12] Imhof, B., and M. Aurrand-Lions, 2004. Adhesion mechanisms regulating the migration of monocytes. *Nat. Rev. Immunol.* 4:432–444.

[13] Carman, C. V., C. D. Jun, A. Salas, and T. A. Springer, 2003. Endothelial cells proactively form microvilli-like membrane projections upon intercellular adhesion molecule i engagement of leukocyte lfa-1. *J. Immunol.* 171:6135–6144.

[14] Banchereau, J., and R. M. Steinman, 1998. Dendritic cells and the control of immunity. *Nature* 392:245–252.

[15] van Gisbergen, K. P., L. C. Paessens, T. B. Geijtenbeek, and Y. van Kooyk, 2005. Molecular mechanisms that set the stage for DC-T cell engagement. *Immunol. Lett.* 97:199–208.

[16] Segura, E., C. Gurin, N. Hogg, S. Amigorena, and C. Thry, 2007. CD8+ dendritic cells use LFA-1 to capture MHC-peptide complexes from exosomes in vivo. *J. Immunol.* 179:1489–1496.

[17] Johnson, L. A., S. Clasper, A. P. Holt, P. F. Lalor, D. Baban, and D. G. Jackson, 2006. An inflammation-induced mechanism for leukocyte transmigration across lymphatic vessel endothelium. *J. Exp. Med.* 203:2763–2777.

[18] Quast, T., B. Tappertzhofen, C. Schild, J. Grell, N. Czeloth, R. Foerster, R. Alon, L. Fraemohs, K. Dreck, C. Weber, T. Laemmermann, M. Sixt, and W. Kolanus, 2009. Cytohesin-1 controls the activation of RhoA and modulates integrin-dependent adhesion and migration of dendritic cells. *Blood* 113:5801–5810.

[19] Bromley, S. K., W. R. Burack, K. G. Johnson, K. Somersalo, T. N. Sims, C. Sumen, M. M. Davis, A. S. Shaw, P. M. Allen, and M. L. Dustin, 2001. The immunological synapse. *Annu. Rev. Immunol.* 19:375–396.

[20] Rossetti, G., M. Collinge, J. R. Bender, R. Molteni, and R. Pardi, 2002. Integrin-dependent regulation of gene expression in leukocytes. *Immunol. Rev.* 186:189–207.

[21] Hogg, N., and P. A. Bates, 2000. Genetic analysis of integrin function in man: LAD-1 and other syndromes. *Matrix Biol.* 19:211–222.

[22] Shimaoka, M., T. Xiao, J. H. Liu, Y. T. Yang, Y. C. Dong, C. D. Jun, A. McCormack, R. G. Zhang, A. Joachimiak, J. Takagi, J. H. Wang, and T. A. Springer, 2003. Structures of the alpha l i domain and its complex with icam-1 reveal a shape-shifting pathway for integrin regulation. *Cell* 112:99–111.

[23] van Kooyk, Y., P. van de Wiel-van Kemenade, P. Weder, T. W. Kuijpers, and C. G. Figdor, 1989. Enhancement of LFA-1-mediated cell adhesion by triggering through CD2 or CD3 on T lymphocytes. *Nature* 342:811–813.

[24] van Kooyk, Y., P. Weder, F. Hogervorst, A. J. Verhoeven, G. van Seventer, A. A. te Velde, J. Borst, G. D. Keizer, and C. G. Figdor, 1991. Activation of LFA-1 through a Ca2(+)-dependent epitope stimulates lymphocyte adhesion. *J. Cell Biol.* 112:345–354.

[25] Kim, M., C. V. Carman, and T. A. Springer, 2003. Bidirectional transmembrane signaling by cytoplasmic domain separation in integrins. *Science* 301:1720–1725.

[26] Kim, M., C. V. Carman, W. Yang, A. Salas, and T. A. Springer, 2004. The primacy of affinity over clustering in regulation of adhesiveness of the integrin alpha(l)beta 2. *J. Cell Biol.* 167:1241–1253.

[27] Stewart, M. P., A. McDowall, and N. Hogg, 1998. Lfa-1-mediated adhesion is regulated by cytoskeletal restraint and by a ca2+-dependent protease, calpain. *J. Cell Biol.* 140:699–707.

[28] Cairo, C. W., R. Mirchev, and D. E. Golan, 2006. Cytoskeletal regulation couples lfa-1 conformational changes to receptor lateral mobility and clustering. *Immunity* 25:297–308.

[29] Kucik, D. F., 2002. Rearrangement of integrins in avidity regulation by leukocytes. *Immunologic Research* 26:199–206.

[30] van Kooyk, Y., P. Weder, K. Heije, and C. G. Figdor, 1994. Extracellular Ca2+ modulates leukocyte function-associated antigen-1 cell surface distribution on T lymphocytes and consequently affects cell adhesion. *J. Cell Biol.* 124:1061–1070.

[31] van Kooyk, Y., and C. G. Figdor, 2000. Avidity regulation of integrins: the driving force in leukocyte adhesion. *Curr. Opin. Cell Biol.* 12:542–547.

[32] Bell, G. I., 1978. Models for the specific adhesion of cells to cells. *Science* 200:618–627.

[33] Chao, N. M., S. H. Young, and M. M. Poo, 1981. Localization of cell-membrane components by surface-diffusion into a trap. *Biophys. J.* 36:139–153.

[34] Kucik, D. F., M. L. Dustin, J. M. Miller, and E. J. Brown, 1996. Adhesion-activating phorbol ester increases the mobility of leukocyte integrin lfa-1 in cultured lymphocytes. *J. Clin. Invest.* 97:2139–2144.

[35] Constantin, G., M. Majeed, C. Giagulli, L. Piccio, J. Y. Kim, E. C. Butcher, and C. Laudanna, 2000. Chemokines trigger immediate beta 2 integrin affinity and mobility changes: Differential regulation and roles in lymphocyte arrest under flow. *Immunity* 13:759–769.

[36] Leitinger, B., and N. Hogg, 2002. The involvement of lipid rafts in the regulation of integrin function. *J. Cell Sci.* 115:963–972.

[37] Chen, J., A. Salas, and T. A. Springer, 2003. Bistable regulation of integrin adhesiveness by a bipolar metal ion cluster. *Nat. Struct. Biol.* 10:995–1001.

[38] Chen, J., W. Yang, M. Kim, C. V. Carman, and T. A. Springer, 2006. Regulation of outside-in signaling and affinity by the beta2 I domain of integrin alphaLbeta2. *Proc. Natl. Acad. Sci. U.S.A.* 103:13062–13067.

[39] Xie, C., M. Shimaoka, T. Xiao, P. Schwab, L. B. Klickstein, and T. A. Springer, 2004. The integrin alpha-subunit leg extends at a ca2+-dependent epitope in the thigh/genu interface upon activation. *Proc. Natl. Acad. Sci. U.S.A.* 101:15422–15427.

[40] Sampath, R., P. J. Gallagher, and F. M. Pavalko, 1998. Cytoskeletal interactions with the leukocyte integrin beta 2 cytoplasmic tailactivation-dependent regulation of associations with talin and alpha-actinin. *J. Biol. Chem.* 273:33588–33594.

[41] Luo, B. H., C. V. Carman, J. Takagi, and T. A. Springer, 2005. Disrupting integrin transmembrane domain heterodimerization increases ligand binding affinity, not valency or clustering. *Proc. Natl. Acad. Sci. U.S.A.* 102:3679–3684.

[42] Dransfield, I., C. Cabanas, A. Craig, and N. Hogg, 1992. Divalent cation regulation of the function of the leukocyte integrin LFA-1. *J. Cell Biol.* 116:219–226.

[43] Carreno, R., D. Li, M. Sen, I. Nira, T. Yamakawa, Q. Ma, and G. B. Legge, 2008. A mechanism for antibody-mediated outside-in activation of lfa-1. *J. Biol. Chem.* 283:10642–10648.

[44] McDowall, A., B. Leitinger, P. Stanley, P. A. Bates, A. M. Randi, and N. Hogg, 1998. The i domain of integrin leukocyte function-associated antigen-1 is involved in a conformational change leading to high affinity binding to ligand intercellular adhesion molecule 1 (icam-1). *J. Biol. Chem.* 273:27396–27403.

[45] Woska, J. R., D. T. Shih, V. R. Taqueti, N. Hogg, T. A. Kelly, and T. K. Kishimoto, 2001. A small-molecule antagonist of lfa-1 blocks a conformational change important for lfa-1 function. *J. Leukocyte Biol.* 70:329–334.

[46] Xiong, J.-P., T. Stehle, B. Diefenbach, R. Zhang, R. Dunker, D. L. Scott, A. Joachimiak, S. L. Goodman, and M. A. Arnaout, 2001. Crystal Structure of the Extracellular Segment of Integrin alpha Vbeta 3. *Science* 294:339–345.

[47] Shi, M., K. Sundramurthy, B. Liu, S.-M. Tan, S. K. A. Law, and J. Lescar, 2005. The Crystal Structure of the Plexin-Semaphorin-Integrin Domain/Hybrid Domain/I-EGF1 Segment from the Human Integrin 2 Subunit at 1.8- Resolution. *J. Biol. Chem.* 280:30586–30593.

[48] Takagi, J., B. M. Petre, T. Walz, and T. A. Springer, 2002. Global conformational rearrangements in integrin extracellular domains in outside-in and inside-out signaling. *Cell* 110:599–511.

[49] Huth, J. R., E. T. Olejniczak, R. Mendoza, H. Liang, E. A. S. Harris, M. L. Lupher, A. E. Wilson, S. W. Fesik, and D. E. Staunton, 2000. NMR and mutagenesis evidence for an I domain allosteric site that regulates lymphocyte function-associated antigen 1 ligand binding. *Proc. Natl. Acad. Sci. U.S.A.* 97:5231–5236.

[50] Dransfield, I., and N. Hogg, 1989. Regulated expression of Mg2+ binding epitope on leukocyte integrin alpha subunits. *EMBO J.* 8:3759–3765.

[51] Luo, B. H., and T. A. Springer, 2006. Integrin structures and conformational signaling. *Curr. Opin. Cell Biol.* 18:579–586.

[52] Bergelson, J. M., and M. E. Hemler, 1995. Integrin-ligand binding. Do integrins use a 'MIDAS touch' to grasp an Asp? *Curr. Biol.* 5:615–617.

[53] Singer, S. J., and G. L. Nicolson, 1972. The fluid mosaic model of the structure of cell membranes. *Science* 175:720–731.

[54] Edidin, M., 2003. Timeline - lipids on the frontier: a century of cell-membrane bilayers. *Nat. Rev. Mol. Cell Biol.* 4:414–418.

[55] Jacobson, K., E. Sheets, and R. Simson, 1995. Revisiting the fluid mosaic model of membranes. *Science* 268:1441–1442.

[56] Kusumi, A., C. Nakada, K. Ritchie, K. Murase, K. Suzuki, H. Murakoshi, R. S. Kasai, J. Kondo, and T. Fujiwara, 2005. Paradigm shift of the plasma membrane concept from the two-dimensional continuum fluid to the partitioned fluid: High-speed single-molecule tracking of membrane molecules. *Annu. Rev. Biophys. Biomol. Str.* 34:351–U54.

[57] Sheets, E. D., G. M. Lee, R. Simson, and K. Jacobson, 1997. Transient confinement of a glycosylphosphatidylinositol-anchored protein in the plasma membrane. *Biochemistry* 36:12449–12458.

[58] Simons, K., and E. Ikonen, 1997. Functional rafts in cell membranes. *Nature* 387:569–572.

[59] Thomas, C. M., and E. J. Smart, 2008. Caveolae structure and function. *J. Cell. Mol. Med.* 12:796–809.

[60] Yanez-Mo, M., O. Barreiro, M. Gordon-Alonso, M. Sala-Valdes, and F. Sanchez-Madrid, 2009. Tetraspanin-enriched microdomains: a functional unit in cell plasma membranes. *Trends Cell Biol.* 19:434–446.

[61] Couchman, J. R., 2003. Syndecans: Proteoglycan regulators of cell-surface microdomains? *Nat. Rev. Mol. Cell Biol.* 4:926–937.

[62] Douglass, A. D., and R. D. Vale, 2005. Single-molecule microscopy reveals plasma membrane microdomains created by protein-protein networks that exclude or trap signaling molecules in t cells. *Cell* 121:937–950.

[63] van Zanten, T. S., A. Cambi, and M. F. Garcia-Parajo, 2010. A nanometer scale optical view on the compartmentalization of cell membranes. *Biochim. Biophys. Acta* 1798:777–787.

[64] Sako, Y., and A. Kusumi, 1994. Compartmentalized structure of the plasma membrane for receptor movements as revealed by a nanometer-level motion analysis. *J. Cell Biol.* 125:1251–1264.

[65] Lenne, P. F., L. Wawrezinieck, F. Conchonaud, O. Wurtz, A. Boned, X. J. Guo, H. Rigneault, H. T. He, and D. Marguet, 2006. Dynamic molecular confinement in the plasma membrane by microdomains and the cytoskeleton meshwork. *EMBO J.* 25:3245–3256.

[66] Wenger, J., F. Conchonaud, J. Dintinger, L. Wawrezinieck, T. W. Ebbesen, H. Rigneault, D. Marguet, and P. F. Lenne, 2007. Diffusion analysis within single nanometric apertures reveals the ultrafine cell membrane organization. *Biophys. J.* 92:913–919.

[67] Dietrich, C., B. Yang, T. Fujiwara, A. Kusumi, and K. Jacobson, 2002. Relationship of lipid rafts to transient confinement zones detected by single particle tracking. *Biophys. J.* 82:274–284.

[68] Fujiwara, T., K. Ritchie, H. Murakoshi, K. Jacobson, and A. Kusumi, 2002. Phospholipids undergo hop diffusion in compartmentalized cell membrane. *J. Cell Biol.* 157:1071–1082.

[69] Lommerse, P. H. M., B. E. Snaar-Jagaiska, H. P. Spaink, and T. Schmidt, 2005. Single-molecule diffusion measurements of H-Ras at the plasma membrane of live cells reveal microdomain localization upon activation. *J. Cell Sci.* 118:1799–1809.

[70] Suzuki, K. G. N., T. K. Fujiwara, F. Sanematsu, R. Iino, M. Edidin, and A. Kusumi, 2007. Gpi-anchored receptor clusters transiently recruit lyn and g alpha for temporary cluster immobilization and lyn activation: single-molecule tracking study 1. *J. Cell Biol.* 177:717–730.

[71] Saxton, M. J., 1995. Single-partickle tranking: effects of corrals. *Biophys. J.* 69:389–398.

[72] Saxton, M. J., and K. Jacobson, 1997. Single-particle tracking: Applications to membrane dynamics. *Annu. Rev. Biophys. Biomol. Str.* 26:373–399.

[73] Saxton, M. J., 2007. A biological interpretation of transient anomalous subdiffusion. I. Qualitative model. *Biophys. J.* 92:1178–1191.

[74] Nicolau, D. V., J. F. Hancock, and K. Burrage, 2007. Sources of anomalous diffusion on cell membranes: a Monte Carlo study. *Biophys. J.* 92:1975–1987.

[75] Schuss, Z., A. Singer, and D. Holcman, 2007. The narrow escape problem for diffusion in cellular microdomains. *Proc. Natl. Acad. Sci. U.S.A.* 104:16098–16103.

[76] Jin, S., and A. S. Verkman, 2007. Single particle tracking of complex diffusion in membranes: Simulation and detection of barrier, raft, and interaction phenomena. *J. Phys. Chem. B* 111:3625–3632.

[77] van Zanten, T. S., A. Cambi, M. Koopman, B. Joosten, C. G. Figdor, and M. F. Garcia-Parajo, 2009. Hotspots of GPI-anchored proteins and integrin nanoclusters function as nucleation sites for cell adhesion. *Proc. Natl. Acad. Sci. U.S.A.* 106:18557–18562.

[78] Hynes, R. O., 1987. Integrins - a family of cell-surface receptors. *Cell* 48:549–554.

[79] Dustin, M. L., T. G. Bivona, and M. R. Philips, 2004. Membranes as messengers in t cell adhesion signaling. *Nat. Immunol.* 5:363–372.

[80] Edidin, M., 2001. Shrinking patches and slippery rafts: scales of domains in the plasma membrane. *Trends Cell Biol.* 11:492–496.

[81] Gaus, K., S. Le Lay, N. Balasubramanian, and M. A. Schwartz, 2006. Integrin-mediated adhesion regulates membrane order. *J. Cell Biol.* 174:725–734.

[82] Krauss, K., and P. Altevogt, 1999. Integrin leukocyte function-associated antigen-1-mediated cell binding can be activated by clustering of membrane rafts. *J. Biol. Chem.* 274:36921–36927.

[83] Marwali, M. R., J. Rey-Ladino, L. Dreolini, D. Shaw, and F. Takei, 2003. Membrane cholesterol regulates lfa-1 function and lipid raft heterogeneity. *Blood* 102:215–222.

[84] Li, N., A. Mak, D. Richards, C. Naber, B. Keller, L. Li, and A. Shaw, 2003. Monocyte lipid rafts contain proteins implicated in vesicular trafficking and phagosome formation. *Proteomics* 3:536–548.

[85] Fabbri, M., S. Di Meglio, M. Gagliani, E. Consonni, R. Molteni, J. Bender, C. Tacchetti, and R. Pardi, 2005. Dynamic partitioning into lipid rafts controls the endo-exocytic cycle of the alpha l/beta(2) integrin, lfa-1, during leukocyte chemotaxis. *Mol. Biol. Cell* 16:5793–5803.

[86] Chichili, G. R., and W. Rodgers, 2007. Clustering of membrane raft proteins by the actin cytoskeleton. *J. Biol. Chem.* 282:36682–91.

[87] Mitchell, J. S., W. S. Brown, D. G. Woodside, P. Vanderslice, and B. W. McIntyre, 2009. Clustering t-cell gm1 lipid rafts increases cellular resistance to shear on fibronectin through changes in integrin affinity and cytoskeletal dynamics. *Immunol. Cell Biol.* 87:324–336.

[88] Delaguillaumie, A., J. Harriague, S. Kohanna, G. Bismuth, E. Rubinstein, M. Seigneuret, and H. Conjeaud, 2004. Tetraspanin CD82 controls the association of cholesterol-dependent microdomains with the actin cytoskeleton in T lymphocytes: relevance to co-stimulation. *J. Cell Sci.* 117:5269–82.

[89] Silverstein, A. M., 2004. Labeled antigens and antibodies: the evolution of magic markers and magic bullets. *Nat. Immunol.* 5:1211–1217.

[90] Hulett, H. R., W. A. Bonner, J. Barrett, and L. A. Herzenberg, 1969. Cell sorting: automated separation of mammalian cells as a function of intracellular fluorescence. *Science* 166:747–749.

[91] Kendrew, J. C., G. Bodo, H. M. Dintzis, R. G. Parrish, H. Wyckoff, and D. C. Phillips, 1958. A three-dimensional model of the myoglobin molecule obtained by x-ray analysis. *Nature* 181:662–666.

[92] Hamill, O. P., A. Marty, E. Neher, B. Sakmann, and F. J. Sigworth, 1981. Improved patch-clamp techniques for high-resolution current recording from cells and cell-free membrane patches. *Pflug. Arch. Eur. J. Phys.* 391:85–100.

[93] Xie, X. S., and R. C. Dunn, 1994. Probing single-molecule dynamics. *Science* 265:361–364.

[94] Nie, S. M., D. T. Chiu, and R. N. Zare, 1994. Probing individual molecules with confocal fluorescence microscopy. *Science* 266:1018–1021.

[95] Xie, X. S., and J. K. Trautman, 1998. Optical studies of single molecules at room temperature. *Annu. Rev. Phys. Chem.* 49:441–480.

[96] Schmidt, T., G. J. Schutz, W. Baumgardner, H. J. Gruber, and H. Schindler, 1995. Characterization of photophysics and mobility of single molecules in a fluid lipid-membrane. *J. Phys. Chem.* 99:17662–17668.

[97] Betzig, E., and R. J. Chichester, 1993. Single molecules observed by near-field scanning optical microscopy. *Science* 262:1422–1425.

[98] Schutz, G. J., H. Schindler, and T. Schmidt, 1997. Imaging single-molecule dichroism. *Opt. Lett.* 22:651–653.

[99] Ha, T., T. Enderle, D. F. Ogletree, D. S. Chemla, P. R. Selvin, and S. Weiss, 1996. Probing the interaction between two single molecules: Fluorescence resonance energy transfer between a single donor and a single acceptor. *Proc. Natl. Acad. Sci. U.S.A.* 93:6264–6268.

[100] Schutz, G. J., W. Trabesinger, and T. Schmidt, 1998. Direct observation of ligand colocalization on individual receptor molecules. *Biophys. J.* 74:2223–2226.

[101] de Bakker, B. I., F. de Lange, A. Cambi, J. P. Korterik, E. M. van Dijk, N. F. van Hulst, C. G. Figdor, and M. F. Garcia-Parajo, 2007. Nanoscale organization of the pathogen receptor DC-SIGN mapped by single-molecule high-resolution fluorescence microscopy. *Chemphyschem* 8:1473–1480.

[102] Schmidt, T., G. J. Schutz, H. J. Gruber, and H. Schindler, 1996. Local stoichiometries determined by counting individual molecules. *Anal. Chem.* 68:4397–4401.

[103] Piestert, O., H. Barsch, V. Buschmann, T. Heinlein, J. P. Knemeyer, K. D. Weston, and M. Sauer, 2003. A single-molecule sensitive dna hairpin system based on intramolecular electron transfer. *Nano Lett.* 3:979–982.

[104] Funatsu, T., Y. Harada, M. Tokunaga, K. Saito, and T. Yanagida, 1995. Imaging of single fluorescent molecules and individual ATP turnovers by single myosin molecules in aqueous solution. *Nature* 374:555–559.

[105] Yildiz, A., J. N. Forkey, S. A. McKinney, T. Ha, Y. E. Goldman, and P. R. Selvin, 2003. Myosin v walks hand-over-hand: Single fluorophore imaging with 1.5-nm localization. *Science* 300:2061–2065.

[106] Thompson, R. E., D. R. Larson, and W. W. Webb, 2002. Precise nanometer localization analysis for individual fluorescent probes. *Biophys. J.* 82:2775–2783.

[107] Koopman, M., A. Cambi, B. I. de Bakker, B. Joosten, C. G. Figdor, N. F. van Hulst, and M. F. Garcia-Parajo, 2004. Near-field scanning optical microscopy in liquid for high resolution single molecule detection on dendritic cells. *FEBS Lett.* 573:6–10.

[108] Taminiau, T. H., R. J. Moerland, F. B. Segerink, L. Kuipers, and N. F. van Hulst, 2007. lambda/4 resonance of an optical monopole antenna probed by single molecule fluorescence. *Nano Lett.* 7:28–33.

[109] Moerner, W. E., 2007. New directions in single-molecule imaging and analysis. *Proc. Natl. Acad. Sci. U.S.A.* 104:12596–12602.

[110] Hell, S. W., and J. Wichmann, 1994. Breaking the diffraction resolution limit by stimulated-emission - stimulated-emission-depletion fluorescence microscopy. *Opt. Lett.* 19:780–782.

[111] Betzig, E., 1995. Proposed method for molecular optical imaging. *Opt. Lett.* 20:237–239.

[112] Betzig, E., G. H. Patterson, R. Sougrat, O. W. Lindwasser, S. Olenych, J. S. Bonifacino, M. W. Davidson, J. Lippincott-Schwartz, and H. F. Hess, 2006. Imaging intracellular fluorescent proteins at nanometer resolution. *Science* 313:1642–1645.

[113] Hess, S. T., T. P. K. Girirajan, and M. D. Mason, 2006. Ultra-high resolution imaging by fluorescence photoactivation localization microscopy. *Biophys. J.* 91:4258–4272.

[114] Rust, M. J., M. Bates, and X. W. Zhuang, 2006. Sub-diffraction-limit imaging by stochastic optical reconstruction microscopy (storm). *Nat. Methods* 3:793–795.

[115] Bates, M., B. Huang, G. T. Dempsey, and X. W. Zhuang, 2007. Multicolor super-resolution imaging with photo-switchable fluorescent probes. *Science* 317:1749–1753.

[116] Lukyanov, K. A., D. M. Chudakov, S. Lukyanov, and V. V. Verkhusha, 2005. Photoactivatable fluorescent proteins. *Nat. Rev. Mol. Cell Biol.* 6:885–891.

[117] Schermelleh, L., R. Heintzmann, and H. Leonhardt, 2010. A guide to super-resolution fluorescence microscopy. *J. Cell Biol.* 190:165–175.

[118] Axelrod, D., P. Ravdin, D. E. Koppel, J. Schlessinger, W. W. Webb, E. L. Elson, and T. R. Podleski, 1976. Lateral motion of fluorescently labeled acetylcholine receptors in membranes of developing muscle fibers. *Proc. Natl. Acad. Sci. U.S.A.* 73:4594–4598.

[119] Anderson, C. M., G. N. Georgiou, I. E. Morrison, G. V. Stevenson, and R. J. Cherry, 1992. Tracking of cell surface receptors by fluorescence digital imaging microscopy using a charge-coupled device camera. Low-density lipoprotein and influenza virus receptor mobility at 4 degrees C. *J. Cell Sci.* 101 (Pt 2):415–425.

[120] Ghosh, R. N., and W. W. Webb, 1994. Automated detection and tracking of individual and clustered cell surface low density lipoprotein receptor molecules. *Biophys. J.* 66:1301–1318.

[121] Haustein, E., and P. Schwille, 2007. Fluorescence correlation spectroscopy: Novel variations of an established technique. *Annu. Rev. Biophys. Biomol. Str.* 36:151–169.

[122] Barak, L. S., and W. W. Webb, 1982. Diffusion of low density lipoprotein-receptor complex on human fibroblasts. *J. Cell Biol.* 95:846–852.

[123] Kusumi, A., Y. Sako, and M. Yamamoto, 1993. Confined lateral diffusion of membrane receptors as studied by single particle tracking (nanovid microscopy). effects of calcium-induced differentiation in cultured epithelial cells. *Biophys. J.* 65:2021–2040.

[124] Smith, P. R., I. E. G. Morrison, K. M. Wilson, N. Fernandez, and R. J. Cherry, 1999. Anomalous diffusion of major histocompatibility complex class i molecules on hela cells determined by single particle tracking. *Biophys. J.* 76:3331–3344.

[125] Pinaud, F., X. Michalet, G. Iyer, E. Margeat, H. P. Moore, and S. Weiss, 2009. Dynamic partitioning of a glycosyl-phosphatidylinositol-anchored protein in glycosphingolipid-rich microdomains imaged by single-quantum dot tracking. *Traffic* 10:691–712.

[126] Andrews, N. L., K. A. Lidke, J. R. Pfeiffer, A. R. Burns, B. S. Wilson, J. M. Oliver, and D. S. Lidke, 2008. Actin restricts FcepsilonRI diffusion and facilitates antigen-induced receptor immobilization. *Nat. Cell Biol.* 10:955–963.

[127] Boyer, D., P. Tamarat, A. Maali, B. Lounis, and M. Orrit, 2002. Photothermal imaging of nanometer-sized metal particles among scatterers. *Science* 297:1160–1163.

[128] Peters, I. M., B. G. de Grooth, J. M. Schins, C. G. Figdor, and J. Greve, 1998. Three dimensional single-particle tracking with nanometer resolution. *Rev. Sci. Instrum.* 69:2762–2766.

[129] Enderlein, J., 2000. Tracking of fluorescent molecules diffusing within membranes. *Appl. Phys. B - Lasers And Optics* 71:773–777.

[130] Levi, V., Q. Q. Ruan, and E. Gratton, 2005. 3-d particle tracking in a two-photon microscope: Application to the study of molecular dynamics in cells. *Biophys. J.* 88:2919–2928.

[131] Feder, T. J., I. BrustMascher, J. P. Slattery, B. Baird, and W. W. Webb, 1996. Constrained diffusion or immobile fraction on cell surfaces: A new interpretation. *Biophys. J.* 70:2767–2773.

[132] Raupach, C., D. P. Zitterbart, C. T. Mierke, C. Metzner, F. A. Muller, and B. Fabry, 2007. Stress fluctuations and motion of cytoskeletal-bound markers. *Phys. Rev. E* 76:011918.

[133] Simson, R., E. D. Sheets, and K. Jacobson, 1995. Detection of temporary lateral confinement of membrane proteins using single-particle tracking analysis. *Biophys. J.* 69:989–993.

[134] Tomishige, M., Y. Sako, and A. Kusumi, 1998. Regulation mechanism of the lateral diffusion of band 3 in erythrocyte membranes by the membrane skeleton. *J. Cell Biol.* 142:989–1000.

[135] Choquet, D., and A. Triller, 2003. The role of receptor diffusion in the organization of the postsynaptic membrane. *Nat. Rev. Neurosci.* 4:251–265.

[136] Schutz, G. J., M. Sonnleitner, and H. Schindler, 2001. Ultrasensitive microscopy of the plasma membrane of living cells. *J. Fluoresc.* 11:177–185.

[137] Harms, G. S., L. Cognet, P. H. M. Lommerse, G. A. Blab, and T. Schmidt, 2001. Autofluorescent proteins in single-molecule research: Applications to live cell imaging microscopy. *Biophys. J.* 80:2396–2408.

[138] Cognet, L., G. S. Harms, G. A. Blab, P. H. M. Lommerse, and T. Schmidt, 2000. Simultaneous dual-color and dual-polarization imaging of single molecules. *Appl. Phys. Lett.* 77:4052–4054.

[139] Koyama-Honda, I., K. Ritchie, T. Fujiwara, R. Iino, H. Murakoshi, R. S. Kasai, and A. Kusumi, 2005. Fluorescence imaging for monitoring the colocalization of two single molecules in living cells. *Biophys. J.* 88:2126–2136.

[140] Morrison, I. E. G., I. Karakikes, R. E. Barber, N. Fernandez, and R. J. Cherry, 2003. Detecting and quantifying colocalization of cell surface molecules by single particle fluorescence imaging. *Biophys. J.* 85:4110–4121.

[141] Blab, G. A. Ph.D. thesis.

[142] Miesenbock, G., D. A. De Angelis, and J. E. Rothman, 1998. Visualizing secretion and synaptic transmission with ph-sensitive green fluorescent proteins. *Nature* 394:192–195.

[143] Miyawaki, A., J. Llopis, R. Heim, J. M. McCaffery, J. A. Adams, M. Ikura, and R. Y. Tsien, 1997. Fluorescent indicators for ca2+ based on green fluorescent proteins and calmodulin. *Nature* 388:882–887.

[144] Kubitscheck, U., O. Kuckmann, T. Kues, and R. Peters, 2000. Imaging and tracking of single gfp molecules in solution. *Biophys. J.* 78:2170–2179.

[145] Gruenwald, D., and U. Kubitscheck, 2005. Intracellular transport of single molecules analyzed by high-speed video microscopy. *Biophys. J.* 88:526A–526A.

[146] Holtzer, L., T. Meckel, and T. Schmidt, 2007. Nanometric three-dimensional tracking of individual quantum dots in cells. *Appl. Phys. Lett.* 90:053902.

[147] Schmidt, T., G. J. Schutz, W. Baumgartner, H. J. Gruber, and H. Schindler, 1996. Imaging of single molecule diffusion. *Proc. Natl. Acad. Sci. U.S.A.* 93:2926–2929.

[148] Bobroff, N., 1986. Position measurement with a resolution and noise-limited instrument. *Rev. Sci. Instrum.* 57:1152–1157.

[149] Rasnik, I., S. A. McKinney, and T. Ha, 2006. Nonblinking and longlasting single-molecule fluorescence imaging. *Nat. Methods* 3:891–893.

[150] Wieser, S., M. Moertelmaier, E. Fuertbauer, H. Stockinger, and G. J. Schutz, 2007. (un)confined diffusion of cd59 in the plasma membrane determined by high-resolution single molecule microscopy. *Biophys. J.* 92:3719–3728.

[151] Harms, G. S., L. Cognet, P. H. M. Lommerse, G. A. Blab, H. Kahr, R. Gamsjager, H. P. Spaink, N. M. Soldatov, C. Romanin, and T. Schmidt, 2001. Single-molecule imaging of l-type ca2+ channels in live cells. *Biophys. J.* 81:2639–2646.

[152] Moertelmaier, M., M. Brameshuber, M. Linimeier, G. J. Schutz, and H. Stockinger, 2005. Thinning out clusters while conserving stoichiometry of labeling. *Appl. Phys. Lett.* 87:263903.

[153] Manley, S., J. M. Gillette, G. H. Patterson, H. Shroff, H. F. Hess, E. Betzig, and J. Lippincott-Schwartz, 2008. High-density mapping of single-molecule trajectories with photoactivated localization microscopy. *Nat. Methods* 5:155–157.

[154] Ritchie, K., X. Y. Shan, J. Kondo, K. Iwasawa, T. Fujiwara, and A. Kusumi, 2005. Detection of non-brownian diffusion in the cell membrane in single molecule tracking. *Biophys. J.* 88:2266–2277.

[155] Meilhac, N., L. Le Guyader, L. Salome, and N. Destainville, 2006. Detection of confinement and jumps in single-molecule membrane trajectories. *Phys. Rev. E* 73:011915.

[156] Giepmans, B. N. G., S. R. Adams, M. H. Ellisman, and R. Y. Tsien, 2006. Review - the fluorescent toolbox for assessing protein location and function. *Science* 312:217–224.

[157] Shaner, N. C., G. H. Patterson, and M. W. Davidson, 2007. Advances in fluorescent protein technology. *J. Cell Sci.* 120:4247–4260.

[158] Schutz, G. J., H. Schindler, and T. Schmidt, 1997. Single-molecule microscopy on model membranes reveals anomalous diffusion. *Biophys. J.* 73:1073–1080.

[159] Cheezum, M. K., W. F. Walker, and W. H. Guilford, 2001. Quantitative comparison of algorithms for tracking single fluorescent particles. *Biophys. J.* 81:2378–2388.

[160] Bonneau, S., M. Dahan, and L. Cohen, 2005. Single quantum dot tracking based on perceptual grouping using minimal paths in a spatiotemporal volume. *IEEE Trans Image Process.* 14:1384–1395.

[161] Yoon, J. W., A. Bruckbauer, W. J. Fitzgerald, and D. Klenerman, 2008. Bayesian inference for improved single molecule fluorescence tracking. *Biophys. J.* 94:4932–4947.

[162] Saffman, P. G., and M. Delbrck, 1975. Brownian motion in biological membranes. *Proc. Natl. Acad. Sci. U.S.A.* 72:3111–3113.

[163] Qian, H., M. Sheetz, and E. Elson, 1991. Single particle tracking. analysis of diffusion and flow in two- dimensional systems. *Biophys. J.* 60:910–921.

[164] Semrau, S., and T. Schmidt, 2007. Particle image correlation spectroscopy (PICS): retrieving nanometer-scale correlations from high-density single-molecule position data. *Biophys. J.* 92:613–621.

[165] Kues, T., A. Dickmanns, R. Lhrmann, R. Peters, and U. Kubitscheck, 2001. High intranuclear mobility and dynamic clustering of the splicing factor u1 snrnp observed by single particle tracking. *Proc. Natl. Acad. Sci. U.S.A.* 98:12021–6.

[166] Vrljic, M., S. Y. Nishimura, S. Brasselet, W. E. Moerner, and H. M. McConnell, 2002. Translational diffusion of individual class ii mhc membrane proteins in cells. *Biophys. J.* 83:2681–2692.

[167] Das, R., C. W. Cairo, and D. Coombs, 2009. A hidden Markov model for single particle tracks quantifies dynamic interactions between LFA-1 and the actin cytoskeleton. *PLoS Comput. Biol.* 5:e1000556.

[168] Mortensen, K. I., L. S. Churchman, J. A. Spudich, and H. Flyvbjerg, 2010. Optimized localization analysis for single-molecule tracking and super-resolution microscopy. *Nat. Methods* 7:377–381.

[169] Treanor, B., D. Depoil, A. Gonzalez-Granja, P. Barral, M. Weber, O. Dushek, A. Bruckbauer, and F. D. Batista, 2010. The membrane skeleton controls diffusion dynamics and signaling through the b cell receptor. *Immunity* 32:187 – 199.

[170] Paige, M. F., E. J. Bjerneld, and W. E. Moerner, 2001. A comparison of through-the-objective total internal reflection microscopy and epifluorescence microscopy for single-molecule fluorescence imaging. *Single Mol.* 2:191–201.

[171] Crocker, J. C., and D. G. Grier, 1996. Methods of digital video microscopy for colloidal studies. *J. Colloid Interface Sci.* 179:298–310.

[172] Saxton, M. J., 1997. Single-particle tracking: The distribution of diffusion coefficients. *Biophys. J.* 72:1744–1753.

[173] Chernick, M. R., 1999. Bootstrap Methods, A practitioner's guide. Wiley.

[174] Press, W. H., S. A. Teukolsky, W. T. Vetterling, and B. P. Flannery, 2007. Numerical Recipes 3rd Edition: The Art of Scientific Computing. Cambridge University Press, 3rd edition.

[175] Savin, T., and P. S. Doyle, 2005. Static and dynamic errors in particle tracking microrheology. *Biophys. J.* 88:623–638.

[176] Peters, I. M., Y. van Kooyk, S. J. van Vliet, B. G. de Grooth, C. G. Figdor, and J. Greve, 1999. 3d single-particle tracking and optical trap measurements on adhesion proteins. *Cytometry* 36:189–194.

[177] Schutz, G. J., G. Kada, V. P. Pastushenko, and H. Schindler, 2000. Properties of lipid microdomains in a muscle cell membrane visualized by single molecule microscopy. *EMBO J.* 19:892–901.

[178] Lommerse, P. H. M., G. A. Blab, L. Cognet, G. S. Harms, B. E. Snaar-Jagalska, H. P. Spaink, and T. Schmidt, 2004. Single-molecule imaging of the h-ras membrane-anchor reveals domains in the cytoplasmic lealet of the cell membrane. *Biophys. J.* 86:609–616.

[179] Marlin, S. D., and T. A. Springer, 1987. Purified intercellular-adhesion molecule-1 (icam-1) is a ligand for lymphocyte function-associated antigen-1 (lfa-1). *Cell* 51:813–819.

[180] Bargatze, R. F., and E. C. Butcher, 1993. Rapid G protein-regulated activation event involved in lymphocyte binding to high endothelial venules. *J. Exp. Med.* 178:367–372.

[181] van Kooyk, Y., S. J. van Vliet, and C. G. Figdor, 1999. The actin cytoskeleton regulates lfa-1 ligand binding through avidity rather than affinity changes. *J. Biol. Chem.* 274:26869–26877.

[182] Carman, C. V., and T. A. Springer, 2003. Integrin avidity regulation: are changes in affinity and conformation underemphasized? *Curr. Opin. Cell Biol.* 15:547–556.

[183] Jin, T. Q., and J. X. Li, 2002. Dynamitin controls beta(2) integrin avidity by modulating cytoskeletal constraint on integrin molecules. *J. Biol. Chem.* 277:32963–32969.

[184] Zhou, X. M., J. X. Li, and D. F. Kucik, 2001. The microtubule cytoskeleton participates in control of beta(2) integrin avidity. *J. Biol. Chem.* 276:44762–44769.

[185] Lub, M., Y. vanKooyk, S. J. vanVliet, and C. G. Figdor, 1997. Dual role of the actin cytoskeleton in regulating cell adhesion mediated by the integrin lymphocyte function-associated molecule-1. *Mol. Biol. Cell* 8:341–351.

[186] Altankov, G., F. Grinnell, and T. Groth, 1996. Studies on the biocompatibility of materials: Fibroblast reorganization of substratum-bound fibronectin on surfaces varying in wettability. *J. Biomed. Mater. Res.* 30:385–391.

[187] Zamir, E., M. Katz, Y. Posen, N. Erez, K. M. Yamada, B. Z. Katz, S. Lin, D. C. Lin, A. Bershadsky, Z. Kam, and B. Geiger, 2000. Dynamics and segregation of cell-matrix adhesions in cultured fibroblasts. *Nat. Cell Biol.* 2:191–196.

[188] Katz, B. Z., E. Zamir, A. Bershadsky, Z. Kam, K. M. Yamada, and B. Geiger, 2000. Physical state of the extracellular matrix regulates the structure and molecular composition of cell-matrix adhesions. *Mol. Biol. Cell* 11:1047–1060.

[189] Hategan, A., K. Sengupta, S. Kahn, E. Sackmann, and D. E. Discher, 2004. Topographical pattern dynamics in passive adhesion of cell membranes. *Biophys. J.* 87:3547–3560.

[190] Takagi, J., and T. A. Springer, 2002. Integrin activation and structural rearrangement. *Immunol. Rev.* 186:141–163.

[191] Kolanus, W., W. Nagel, B. Schiller, L. Zeitlmann, S. Godar, H. Stockinger, and B. Seed, 1996. Alpha L beta 2 integrin/LFA-1 binding to ICAM-1 induced by cytohesin-1, a cytoplasmic regulatory molecule. *Cell* 86:233–242.

[192] Calderwood, D. A., 2004. Integrin activation. *J. Cell Sci.* 117:657–666.

[193] Wegener, K. L., A. W. Partridge, J. Han, A. R. Pickford, R. C. Liddington, M. H. Ginsberg, and I. D. Campbell, 2007. Structural basis of integrin activation by talin. *Cell* 128:171–182.

[194] Diez-Ahedo, R., D. Normanno, O. Esteban, G. J. Bakker, C. G. Figdor, A. Cambi, and M. F. Garcia-Parajo, 2009. Dynamic re-organization of individual adhesion nanoclusters in living cells by ligand-patterned surfaces. *Small* 5:1258–1263.

[195] Smith, A., Y. Carrasco, P. Stanley, N. Kieffer, F. Batista, and N. Hogg, 2005. A talin-dependent lfa-1 focal zone is formed by rapidly migrating t lymphocytes. *J. Cell Biol.* 170:141–151.

[196] Porter, J., M. Bracke, A. Smith, D. Davies, and N. Hogg, 2002. Signaling through integrin lfa-1 leads to filamentous actin polymerization and remodeling, resulting in enhanced t cell adhesion. *J. Immunol.* 168:6330–6335.

[197] Giagulli, C., E. Scarpini, L. Ottoboni, S. Narumiya, E. Butcher, G. Constantin, and C. Laudanna, 2004. RhoA and zeta PKC control distinct modalities of LFA-1 activation by chemokines: Critical role of LFA-1 affinity triggering in lymphocyte in vivo homing. *Immunity* 20:25–35.

[198] Gaborski, T., A. J. Clark, R. Waugh, and J. McGrath, 2008. Membrane mobility of beta2 integrins and rolling associated adhesion molecules in resting neutrophils. *Biophys. J.* 95:4934–47.

[199] Cairo, C., and D. Golan, 2007. T cell adhesion mechanisms revealed by receptor lateral mobility. *Biopolymers* 89:409–419.

[200] VanCompernolle, S. E., S. Levy, and S. C. Todd, 2001. Anti-cd81 activates lfa-1 on t cells and promotes t cellb cell collaboration. *Eur. J. Immunol.* 31:823–831.

[201] Shibagaki, N., K.-i. Hanada, H. Yamashita, S. Shimada, and H. Hamada, 1999. Overexpression of cd82 on human t cells enhances lfa-1 / icam-1-mediated cell-cell adhesion: functional association between cd82 and lfa-1 in t cell activation. *Eur. J. Immunol.* 29:4081–4091.

[202] Hemler, M. E., 1998. Integrin associated proteins. *Curr. Opin. Cell Biol.* 10:578–585.

[203] Berditchevski, F., 2001. Complexes of tetraspanins with integrins: more than meets the eye. *J. Cell Sci.* 114:4143–4151.

[204] Shamri, R., V. Grabovsky, S. W. Feigelson, O. Dwir, Y. V. Kooyk, and R. Alon, 2002. Chemokine stimulation of lymphocyte alpha 4 integrin avidity but not of leukocyte function-associated antigen-1 avidity to endothelial ligands under shear flow requires cholesterol membrane rafts. *J. Biol. Chem.* 277:40027–35.

[205] Kucik, D. F., E. L. Elson, and M. P. Sheetz, 1999. Weak dependence of mobility of membrane protein aggregates on aggregate size supports a viscous model of retardation of diffusion. *Biophys. J.* 76:314–322.

[206] Saxton, M. J., 1996. Anomalous diffusion due to binding: A monte carlo study. *Biophys. J.* 70:1250–1262.

[207] Kusumi, A., I. Koyama-Honda, and K. Suzuki, 2004. Molecular dynamics and interactions for creation of stimulation-induced stabilized rafts from small unstable steady-state rafts. *Traffic* 5:213–230.

[208] Vitte, J., A. Pierres, A. Benoliel, and P. Bongrand, 2004. Direct quantification of the modulation of interaction between cell- or surface-bound lfa-1 and icam-1. *J. Leukocyte Biol.* 76:594–602.

[209] Salas, A., M. Shimaoka, S. Chen, C. Carman, and T. Springer, 2002. Transition from rolling to firm adhesion is regulated by the conformation of the I domain of the integrin lymphocyte function-associated antigen-1. *J. Biol. Chem.* 277:50255–50262.

[210] Sigal, A., D. A. Bleijs, V. Grabovsky, S. J. van Vliet, O. Dwir, C. G. Figdor, Y. van Kooyk, and R. Alon, 2000. The lfa-1 integrin supports rolling adhesions on icam-1 under physiological sheer flow in a permissive cellular environment. *J. Immunol.* 165:442–452.

[211] Pasvolsky, R., V. Grabovsky, C. Giagulli, Z. Shulman, R. Shamri, S. W. Feigelson, C. Laudanna, and R. Alon, 2008. RhoA is involved in LFA-1 extension triggered by CXCL12 but not in a novel outside-in LFA-1 activation facilitated by CXCL9'. *J. Immunol.* 180:2815–2823.

[212] Lub, M., Y. van Kooyk, and C. G. Figdor, 1995. Ins and outs of LFA-1. *Immunol. Today* 16:479–483.

[213] Dustin, M. L., 1990. Two-way signalling through the LFA-1 lymphocyte adhesion receptor. *Bioessays* 12:421–427.

[214] Tadokoro, S., S. J. Shattil, K. Eto, V. Tai, R. C. Liddington, J. M. de Pereda, M. H. Ginsberg, and D. A. Calderwood, 2003. Talin Binding to Integrin beta Tails: A Final Common Step in Integrin Activation. *Science* 302:103–106.

[215] Moser, M., K. R. Legate, R. Zent, and R. Fassler, 2009. The Tail of Integrins, Talin, and Kindlins. *Science* 324:895–899.

[216] Weber, K. S., C. Weber, G. Ostermann, H. Dierks, W. Nagel, and W. Kolanus, 2001. Cytohesin-1 is a dynamic regulator of distinct lfa-1 functions in leukocyte arrest and transmigration triggered by chemokines. *Curr. Biol.* 11:1969 – 1974.

[217] Calderwood, D. A., S. J. Shattil, and M. H. Ginsberg, 2000. Integrins and actin filaments: reciprocal regulation of cell adhesion and signaling. *J. Biol. Chem.* 275:22607–22610.

[218] Larsson, L., and S. Ohman, 1978. Serum ionized calcium and corrected total calcium in borderline hyperparathyroidism. *Clin. Chem.* 24:1962–1965.

[219] Grzesiak, J. J., and M. D. Pierschbacher, 1995. Shifts in the concentrations of magnesium and calcium in early porcine and rat wound fluids activate the cell migratory response. *J. Clin. Invest.* 95:227–233.

[220] Grzesiak, J. J., and M. D. Pierschbacher, 1995. Changes in the concentrations of extracellular Mg++ and Ca++ down-regulate E-cadherin and up-regulate alpha 2 beta 1 integrin function, activating keratinocyte migration on type I collagen. *J. Invest. Dermatol.* 104:768–774.

[221] Lange, T. S., J. Kirchberg, A. K. Bielinsky, A. Leuker, I. Bank, T. Ruzicka, and K. Scharffetter-Kochanek, 1995. Divalent cations (Mg2+, Ca2+) differentially influence the beta 1 integrin-mediated migration of human fibroblasts and keratinocytes to different extracellular matrix proteins. *Exp. Dermatol.* 4:130–137.

[222] Yoshinaga, I. G., S. K. Dekker, M. C. Mihm, and H. R. Byers, 1994. Differential effect of magnesium and calcium on integrin-mediated melanoma cell migration on type IV collagen and fibronectin. *Melanoma Res.* 4:371–378.

[223] Grzesiak, J. J., and M. Bouvet, 2008. Divalent cations modulate the integrin-mediated malignant phenotype in pancreatic cancer cells. *Cancer Sci.* 99:1553–1563.

[224] Thamilselvan, V., M. Fomby, M. Walsh, and M. D. Basson, 2003. Divalent cations modulate human colon cancer cell adhesion. *J. Surg. Res.* 110:255–265.

[225] van der Voort van Zyp, J., W. C. Conway, V. Thamilselvan, L. Polin, and M. D. Basson, 2005. Divalent cations influence colon cancer cell adhesion in a murine transplantable tumor model. *Am. J. Surg.* 190:701–707.

[226] Alon, R., and M. L. Dustin, 2007. Force as a facilitator of integrin conformational changes during leukocyte arrest on blood vessels and antigen-presenting cells. *Immunity* 26:17–27.

[227] Eich, C., J. de Vries, P. Linssen, A. de Boer, J. Boezeman, C. Figdor, and A. Cambi. The lymphoid chemokine ccl21 reactivates lfa-1 on human dendritic cells.

[228] Evans, R., I. Patzak, L. Svensson, K. De Filippo, K. Jones, A. McDowall, and N. Hogg, 2009. Integrins in immunity. *J. Cell Sci.* 122:215–225.

[229] Cambi, A., K. Gijzen, J. M. de Vries, R. Torensma, B. Joosten, G. J. Adema, M. G. Netea, B. J. Kullberg, L. Romani, and C. G. Figdor, 2003. The C-type lectin DC-SIGN (CD209) is an antigen-uptake receptor for Candida albicans on dendritic cells. *Eur. J. Immunol.* 33:532–538.

[230] Geijtenbeek, T. B., R. Torensma, S. J. van Vliet, G. C. van Duijnhoven, G. J. Adema, Y. van Kooyk, and C. G. Figdor, 2000. Identification of DC-SIGN, a novel dendritic cell-specific ICAM-3 receptor that supports primary immune responses. *Cell* 100:575–585.

[231] Ritchie, K., and J. Spector, 2007. Single molecule studies of molecular diffusion in cellular membranes: determining membrane structure. *Biopolymers* 87:95–101.

[232] Goswami, D., K. Gowrishankar, S. Bilgrami, S. Ghosh, R. Raghupathy, R. Chadda, R. Vishwakarma, M. Rao, and S. Mayor, 2008. Nanoclusters of GPI-anchored proteins are formed by cortical actin-driven activity. *Cell* 135:1085–1097.

[233] Wieser, S., and G. J. Schutz, 2008. Tracking single molecules in the live cell plasma membrane-Do's and Don't's. *Methods* 46:131–140.

[234] Resch-Genger, U., M. Grabolle, S. Cavaliere-Jaricot, R. Nitschke, and T. Nann, 2008. Quantum dots versus organic dyes as fluorescent labels. *Nat. Methods* 5:763–775.

[235] Pinaud, F., S. Clarke, A. Sittner, and M. Dahan, 2010. Probing cellular events, one quantum dot at a time. *Nat. Methods* 7:275–285.

[236] Wang, X., X. Ren, K. Kahen, M. A. Hahn, M. Rajeswaran, S. Maccagnano-Zacher, J. Silcox, G. E. Cragg, A. L. Efros, and T. D. Krauss, 2009. Non-blinking semiconductor nanocrystals. *Nature* 459:686–689.

[237] Clarke, S., F. Pinaud, O. Beutel, C. You, J. Piehler, and M. Dahan, 2010. Covalent monofunctionalization of peptide-coated quantum dots for single-molecule assays. *Nano Lett.* 10:2147–2154.

[238] Jaqaman, K., D. Loerke, M. Mettlen, H. Kuwata, S. Grinstein, S. L. Schmid, and G. Danuser, 2008. Robust single-particle tracking in live-cell time-lapse sequences. *Nat. Methods* 5:695–702.

[239] He, H. T., and D. Marguet, 2011. Detecting Nanodomains in Living Cell Membrane by Fluorescence Correlation Spectroscopy. *Annu Rev Phys Chem* 62.

[240] Manzo, C., T. S. van Zanten, and M. F. Garcia-Parajo, 2011. Nanoscale fluorescence correlation spectroscopy on intact living cell membranes with NSOM probes. *Biophys. J.* 100:8–10.

[241] Eggeling, C., C. Ringemann, R. Medda, G. Schwarzmann, K. Sandhoff, S. Polyakova, V. N. Belov, B. Hein, C. von Middendorff, A. Schonle, and S. W. Hell, 2009. Direct observation of the nanoscale dynamics of membrane lipids in a living cell. *Nature* 457:1159–1162.

[242] Bacia, K., I. V. Majoul, and P. Schwille, 2002. Probing the endocytic pathway in live cells using dual-color fluorescence cross-correlation analysis. *Biophys. J.* 83:1184–1193.

[243] Nicolau, D. V., K. Burrage, R. G. Parton, and J. F. Hancock, 2006. Identifying optimal lipid raft characteristics required to promote nanoscale protein-protein interactions on the plasma membrane. *Mol. Cell. Biol.* 26:313–323.

[244] Wieser, S., M. Axmann, and G. J. Schutz, 2008. Versatile analysis of single-molecule tracking data by comprehensive testing against Monte Carlo simulations. *Biophys. J.* 95:5988–6001.

[245] Vogel, V., and M. P. Sheetz, 2009. Cell fate regulation by coupling mechanical cycles to biochemical signaling pathways. *Curr. Opin. Cell Biol.* 21:38–46.

[246] Kukreti, S., K. Konstantopoulos, C. W. Smith, and L. V. McIntire, 1997. Molecular Mechanisms of Monocyte Adhesion to Interleukin-1beta -Stimulated Endothelial Cells Under Physiologic Flow Conditions. *Blood* 89:4104–4111.

[247] Thoumine, O., E. Saint-Michel, C. Dequidt, J. Falk, R. Rudge, T. Galli, C. Faivre-Sarrailh, and D. Choquet, 2005. Weak Effect of Membrane Diffusion on the Rate of Receptor Accumulation at Adhesive Contacts. *Biophys. J.* 89:L40–42.

Summary

Leukocytes have the ability to rapidly switch their adhesion in response to the cell's physiological environment. How these cells modulate their adhesiveness during the different stages of their life cycle, has been a central question for decades in immunology. Adhesion regulation has its origin at the molecular scale, where processes are dynamic, heterogenous and tightly orchestrated. To unravel these unanswered questions it is therefore of utter importance to probe biological processes in a time-dependent manner on a molecular scale. With the development of Single Particle Tracking and ultimately Single Dye Tracing, it is now possible to follow the mobility of individual biomolecules on the plasma membrane of living cells. Observation of mobility of individual biomolecules does not only provide information about the local micro-environment of the probed biomolecules, but it also gives complementary insight into the processes at work at the nanolevel. The aim of this research has been to investigate the lateral mobility of one of the most important receptors involved in cell adhesion in the immune system: the integrin receptor LFA-1 (lymphocyte function-associated antigen 1; $\alpha_L\beta_2$; CD11a/CD18). By using single molecule techniques we have been able to deepen our understanding of LFA-1 mobility and its consequences for LFA-1 affinity and avidity regulation on THP-1 monocytes and immature dendritic cells (imDCs).

In **Chapter 1**, we briefly introduce the integrin receptor LFA-1 and its ligand binding capacity regulation. LFA-1 plays a crucial role in leukocyte arrest and migration through the vasculature and in binding to antigen presenting cells. Therefore, its function needs to be highly dynamic and versatile. Cells have the ability to rapidly adapt LFA-1 mediated adhesion strategies by modulation of the molecules conformation and its spatial organization on the cell membrane. Leukocyte adhesion is tightly regulated at the nanometric scale and therefore high-resolution microscopy techniques play an important role in the investigation of the spatial distribution of LFA-1 and its interacting molecules. Therefore, single molecule detection sensitive microscopy techniques specially tailored to visualize membrane biomolecule organization and dynamics at high spatial and/or temporal resolution have been reviewed. In addition, the reconstruction and analysis of biomolecule trajectories on the cell membrane is addressed.

In order to investigate the lateral mobility of LFA-1 on monocytes and imDCs, we developed a toolbox to image, trace and analyze the mobility behavior of heterogeneously distributed individual transmembrane receptor nanoclusters and single molecules on living cells. In **Chapter 2**, the implementation of a combined EPI-TIR (Total Internal Reflection) fluorescence microscope has been described and its single molecule localization accuracies have been determined. Furthermore, colloidal particle tracking algorithms have been successfully modified and implemented for semi-automatic tracing of individual LFA-1 nanoclusters that have a heterogeneous packing density and a wide range of mobility behavior. To inquire on the wide range of mobility behavior within a single dataset, we developed an analysis method where single trajectory analysis and ensemble analysis techniques were combined. The potential of the developed tracking and analysis tools was demonstrated by analysis of trajectories of mAb L16 labeled LFA-1 nanoclusters on resting (THP-1) monocytes.

On resting blood derived monocytes LFA-1 is distributed in ligand independent pro-active (extended LFA-1 conformations) and inactive (bent LFA-1 conformation) nanoclusters on the cell membrane. However, the mobility characteristics of these pro-active and inactive nanoclusters and how cluster dynamics, affinity and valency interplay to regulate monocyte adhesion are yet unknown. In **Chapter 3**, we applied the SDT (single dye tracing) and analysis approach described in chapter 2 to map the mobility of individual LFA-1 nanoclusters on resting and ligated monocytes. We demonstrated that on resting monocytes, LFA-1 is primarily mobile, without interaction to the cytoskeleton and with a small subset of nanoclusters in the extended conformation. This subset displays a different mobility profile with immobile cytoskeleton tethered, slow hindered and fast Brownian diffusion. Our result questions earlier models of cytoskeletal anchorage of the overall integrin receptor population on resting cells and supports more complex models where only a subset of extended LFA-1 is bound to the cytoskeleton. Furthermore, when cells were brought into contact with ligated surfaces, extended LFA-1 was recruited to the binding site. Remarkably, the diffusion profile of extended LFA-1 was also altered at the unligated dorsal cell side, suggesting triggering of inside-out signalling pathways regulating overall LFA-1 affinity and consequently mobility.

Despite extensive study of the integrin structure and inside-out signalling processes, the role of extracellular cations in LFA-1 mediated leukocyte adhesion remains controversial. On one hand, mutagenesis experiments showed that removal of Ca^{2+} augments the high affinity form of the integrin and combined with Mg^{2+} synergize to promote firm adhesion. On the other hand, Ca^{2+} ions seem to induce microclustering of LFA-1 on various types of T lymphocytes, a necessary step for avidity-based regulation. In **Chapter 4**, we inquired on the dual role of Ca^{2+} on LFA-1 mediated adhesion of monocytic cells by mapping mobility of individual LFA-1 nanoclusters under different extracellular

cation conditions. We found that under low (0.04mM) Ca^{2+} conditions nanocluster mobility is strongly reduced with respect to high (0.4mM) Ca^{2+}/Mg^{2+} conditions: the immobile, cytoskeleton tethered subpopulation of the overall LFA-1 population increased 8-fold. Consistent with the effect of low Ca^{2+} on the conformation of LFA-1, we observed that the mobility of the total LFA-1 population gradually changed as a function of Ca^{2+} reduction and became essentially the same as to the one displayed by active LFA-1 at low Ca^{2+} levels. On the other hand, the absence of extracellular Mg^{2+} did not have any major effects on LFA-1 mobility. Altogether, our results indicate that reduction of extracellular Ca^{2+}, but not Mg^{2+}, induces conformational changes in LFA-1 that translate into integrin extension and transmembrane domain separation, leading to increased interactions with cytoskeletal mediators in the direct microenvironment of LFA-1. With shear flow assay experiments we observed that under low shear flow conditions (0.2 dyn/cm^{-2}), Ca^{2+} dependent avidity synergizes with Mg^{2+} dependent affinity to establish LFA-1 mediated cell binding. Under higher shear flow conditions (0.5 dyn/cm^{-2}) only affinity seems to play a role. Our results have direct implications for studies where integrin activation is induced by removal of Ca^{2+} because although high affinity forms are generated, this pool of molecules is not able to reach the required avidity, failing to support firm adhesion under low shear flow conditions. Moreover, we showed that extracellular Ca^{2+} levels can be used to differentially tune the balance between affinity and avidity of LFA-1 ligand binding on resting monocytes.

Upon differentiation of monocytes into imDCs, LFA-1 membrane organization in active and inactive nanoclusters disperses and its affinity reduces. In **Chapter 5**, we addressed the fundamental question of how these changes in organization and conformational state relate to mobility. We made a detailed study of LFA-1 mobility on imDCs and compared the results with those obtained for resting monocytes and resting T cells. Like on monocytes, imDCs also display immobile, slow mobile and fast mobile subpopulations showing predominantly random diffusion. However, in contrast to monocytes, the diffusion constant of the total, primarily inactive LFA-1 population is twofold larger. According to hydrodynamic theory, this increased mobility correlates well with its change in spatial organization from nanocluster to monomeric. Here we demonstrated that besides affinity, also changes in the nano-scale organization of LFA-1 influence its lateral mobility. In addition, we showed that differences in the viscous resistance at the micro-scale experienced by LFA-1 are a likely explanation for the observed differences in LFA-1 diffusion constants between imDCs and resting T cells and, between slow and fast mobility subpopulations.

Finally, in **Chapter 6** the results described in this work are brought in a broader perspective of existing studies and directions for future research are given.

Samenvatting

Witte bloedcellen kunnen hun adhesie-eigenschappen snel omschakelen als reactie op de fysiologische context waarin ze zich bevinden. Hoe deze cellen hun adhesie moduleren gedurende de verschillende stadia van hun leven, is al decennia lang een belangrijke vraag binnen de Immunologie. De oorsprong van adhesie regulatie is te vinden op de moleculaire schaal. Op dit niveau zijn deze processen dynamisch, heterogeen en nauw samenhangend. Om de vraag in kwestie te beantwoorden, is het daarom van groot belang om de biologische processen dynamisch en op moleculaire schaal in kaart te brengen. Door de ontwikkeling van single particle tracking en single dye tracing, is het mogelijk geworden om de beweging van individuele moleculen op het plasma membraan van levende cellen te volgen. Hiermee kan niet alleen de omgeving van getraceerde biomoleculen in kaart gebracht worden, de techniek verschaft ook complementair inzicht in de processen welke op de nanometer-schaal plaats vinden. Het doel van dit onderzoek was om de laterale mobiliteit van een van de belangrijkste adhesie receptoren binnen het immuun systeem te bestuderen: de integrin receptor LFA-1 (lymphocyte function-associated antigen 1; $\alpha_L\beta_2$; CD11a/CD18). Door op moleculaire schaal door te dringen, hebben we onze kennis van LFA-1 mobiliteit vergroot. Ten gevolge hiervan hebben we meer inzicht gekregen in de consequenties van LFA-1 mobiliteit voor LFA-1 affiniteit en aviditeit regulatie op monocyten en immature dendritische cellen (imDCs).

In **Hoofdstuk 1** wordt een beknopte introductie gegeven van de integrin receptor LFA-1, waarna de verschillende regulatie-mechanismen van LFA-1 gerelateerde bindings capaciteit aan de orde komen. LFA-1 speelt een cruciale rol gedurende de arrest, de migratie door de vaatwand en gedurende het binden van leukocyten aan antigeen presenterende cellen. Hierdoor moet LFA-1 zeer dynamisch en veelzijdig kunnen functioneren. Leukocyten hebben de mogelijkheid om LFA-1 gerelateerde adhesie snel aan te passen door verandering van de conformatie van de LFA-1 moleculen en door aanpassing van hun spatiale organisatie op het celmembraan. De adhesie is nauwgezet gereguleerd op de nanometer schaal; hierdoor spelen hoge-resolutie microscopie technieken een belangrijke rol in het onderzoek naar de spatiale organisatie van LFA-1 en gerelateerde moleculen. Daarom worden single-molecule detectie gevoelige microscopie technieken, welke speciaal geschikt zijn voor de visualisatie van

de organisatie en dynamica van biomoleculen op het celmembraan, uitvoerig besproken. Bovendien wordt er nader ingegaan op de reconstructie en analyse van biomolecuul trajecten op het celmembraan.

Om de laterale mobiliteit van LFA-1 op monocyten en imDCs te kunnen onderzoeken, hebben we een gereedschap set ontwikkeld waarmee heterogeen gedistribueerde individuele transmembraan receptoren en nanoclusters op levende cellen in de tijd afgebeeld, gevolgd en geanalyseerd kunnen worden. In **Hoofdstuk 2** wordt de implementatie en karakterisering van een gecombineerde EPI-TIR (Total Internal Reflection) fluorescentie microscoop besproken. Verder wordt er besproken hoe colloidal particle tracking algoritmes succesvol aangepast en geïmplementeerd zijn voor het semi-automatisch volgen van individuele LFA-1 nanoclusters, welke heterogeen verspreid zijn over- en een verscheidenheid aan mobiliteit vertonen op het celmembraan. Om de verschillende vormen van mobiliteit welke aanwezig zijn in een enkele dataset te kunnen onderscheiden en karakteriseren, hebben we een analyse methode ontwikkeld welke zowel individuele als ensembles van trajecten in beschouwing neemt. De potentie van de ontwikkelde tracking en analyse gereedschappen wordt gedemonstreerd aan de hand van analyse van gereconstrueerde trajecten van mAb L16 gelabelde LFA-1 nanoclusters op rustende (THP-1) monocyten.

Op het celmembraan van rustende, uit het bloed gextraheerde monocyten is LFA-1 gedistribueerd in ligand onafhankelijke pro-actieve (gestrekte LFA-1 conformatie) en inactieve (gebogen LFA-1 conformatie) nanoclusters. Echter, de mobiliteit van deze nanoclusters en hoe cluster dynamica, affiniteit en aviditeit interacteren om monocyt adhesie te reguleren, zijn tot op heden onbekend. In **Hoofdstuk 3** hebben we single dye tracing en analyse methoden uit hoofdstuk 2 toegepast om de mobiliteit van individuele LFA-1 nanoclusters op rustende en geligeerde monocyten te bestuderen. Onze resultaten tonen aan dat LFA-1 nanoclusters voornamelijk mobiel zijn op rustende monocyten, zonder interactie met het cytoskelet en met een kleine subset van LFA-1 met de gestrekte conformatie. Deze subset van nanoclusters vertoont een ander mobiliteitsprofiel, met immobiel cytoskelet gebonden, langzame gehinderde en snelle Brownian diffusie. Onze resultaten trekken voorgaande modellen in twijfel, waarbij op rustende cellen het merendeel van de integrin receptor populatie immobiel en cytoskelet gebonden is. Daarentegen zijn onze resultaten in overeenstemming met meer complexe modellen waarbij slechts een subset van LFA-1 met de gestrekte conformatie aan het cytoskelet gebonden is. Bovendien, wanneer cellen in contact gebracht werden met geligeerde oppervlakten, dan werd pro-actief LFA-1 gerecruteerd aan het geligeerde contactoppervlak. Opmerkelijk genoeg veranderde het mobiliteitsprofiel van het overgebleven LFA-1 met gestrekte conformatie ook aan de ongeligeerde, dorsale kant van de cellen. Deze waarneming suggereert dat ligering van LFA-1 binnen-naar-buiten signaal processen triggert, welke de balans tussen de verschillende LFA-1 conformaties moduleert

en daarmee de mobiliteitsprofielen verandert.

Ondanks uitgebreid onderzoek naar de structuur van integrin receptor moleculen en aan hen gerelateerde binnen-naar-buiten signaal processen, blijft de rol van extracellulaire kationen in LFA-1 gerelateerde leukocyte adhesie controversieel. Aan de ene kant laten mutagenesis studies zien dat verwijdering van Ca^{2+} de hoge affiniteit conformatie van LFA-1 versterkt, wat in combinatie met Mg^{2+} een sterke adhesie promoot. Aan de andere kant, op verschillende typen T cellen lijkt extracellulair Ca^{2+} microclustering van LFA-1 te induceren, een noodzakelijke stap voor aviditeit gebaseerde adhesie regulatie. In **Hoofdstuk 4** hebben we de dubbele rol van Ca^{2+} in LFA-1 gerelateerde adhesie van monocyten geëxploreerd, door middel van het in kaart brengen van de mobiliteit van individuele LFA-1 nanoclusters onder verschillende extracellulaire cation condities. Onze resultaten laten zien dat de mobiliteit van nanoclusters sterk gereduceerd is onder lage (0.04mM) Ca^{2+} condities ten opzichte van hoge (0.4mM) Ca^{2+}/Mg^{2+} condities: de immobiele, cytoskelet gerelateerde subpopulatie van de totale LFA-1 fractie nam met een factor 8 toe. Consistent met het effect van Ca^{2+} op de conformaties van LFA-1, zagen we een geleidelijke verschuiving van de mobiliteit van de totale LFA-1 populatie ten gevolge van Ca^{2+} reductie, naar de mobiliteit geobserveerd voor de actieve fractie. Echter, de afwezigheid van Mg^{2+} had geen grote gevolgen voor de mobiliteit van LFA-1. Kortom, onze resultaten geven de indicatie dat reductie van Ca^{2+}, maar niet Mg^{2+}, globale veranderingen in de LFA-1 moleculen teweeg brengt welke leiden tot een toename van interactie met cytoskelet gerelateerde eiwitten in de directe micro-omgeving van LFA-1. We observeerden met behulp van shear flow assay experimenten dat onder lage shear flow condities (0.2 dyn/cm^{-2}), Ca^{2+} gerelateerde aviditeit en Mg^{2+} gerelateerde affiniteit beide bijdragen aan LFA-1 gerelateerde cel binding. Echter, onder hogere shear flow condities (0.5 dyn/cm^{-2}) lijkt alleen affiniteit een rol te spelen. Onze resultaten hebben directe implicaties voor studies waarbij integrin activatie genduceerd wordt met behulp van verwijdering van Ca^{2+}. Ondanks dat de aantallen LFA-1 moleculen met een hoge affiniteit zullen toenemen, zijn deze niet in staat om de gewenste aviditeit te bereiken, waardoor ze niet bijdragen aan een toename van LFA-1 gerelateerde adhesie onder lage shear flow condities. Bovendien hebben we laten zien dat extracellulair Ca^{2+} gebruikt kan worden om de balans tussen affiniteit en aviditeit te 'tunen' gedurende LFA-1 ligand binding.

Gedurende differentiatie van monocyten in imDCs verliezen cellen hun LFA-1 membraan organisatie in actieve en inactieve nanoclusters en neemt de algehele LFA-1 affiniteit af. In **Hoofdstuk 5** beantwoorden we de fundamentele vraag, hoe deze veranderingen in LFA-1 organisatie en conformatie gerelateerd zijn aan de laterale mobiliteit. We hebben LFA-1 mobiliteit op imDCs in detail in kaart gebracht en de resultaten vergeleken met die van rustende monocyten en rustende T lymfocyten. Gelijk aan monocyten, is LFA-1 diffusie op het

membraan van imDCs voornamelijk Brownian en op te delen in immobiele, langzame en snelle subpopulaties. Echter, in contrast met monocyten is de diffusie constante van de totale, voornamelijk inactieve LFA-1 populatie een factor-2 groter. Met behulp van hydrodynamische theorie laten we zien dat dit verschil goed correleert met de verschillen in spatiale organisatie van LFA-1 tussen monocyten en imDCs. Naast affiniteit, hebben dus ook veranderingen op de nanoschaal in de organisatie van LFA-1 op het celmembraan invloed op de mobiliteit van LFA-1. Daarnaast laten we zien dat de verschillen in de viskeuze weerstand welke LFA-1 moleculen op de micro-schaal ondervinden, een goede verklaring vormen voor de verschillende LFA-1 diffusie constanten waargenomen op imDCs versus rustende T cellen en, langzame versus snelle LFA-1 subpopulaties.

Tenslotte worden in **Hoofdstuk 6** de resultaten van dit werk in het bredere perspectief van bestaande studies geplaatst en worden er suggesties voor toekomstig onderzoek gegeven.

Acknowledgement / Dankwoord

Promoveren, aio-schap, het is een lange interessante reis binnen een nog langere interessante reis. Een reis van geluk en van pijn, liefde en eenzaamheid, leren en frustratie, schoonheid en chaos, hoop en twijfel, tijd en druk, ontdekkingen en speculaties, bergen en llobregats, afstand en dichtbij, geven en verlies. Nu ik terug kijk, besef ik dat jullie me heel veel hebben gegeven. Heel veel geduld, een nieuwe 'familie', de warme familie van vreemdelingen in een vreemd land, de talen Spaans en biologie, de kans om schaamteloos met behulp van belastinggeld te ervaren hoe diep ik in de diepte der fundamentele wetenschappen kan springen.

Op dit kruispunt kijk ik terug en besef ik des te meer dat het eigenlijk heel lang geduurd heeft. Niet alleen in tijd, nee, er is ook heel veel gebeurd in deze jaren: samenwonen, emigreren, opnieuw Nederlander zijn, trouwen, we hebben Barbara gekregen! Ik ben heel dankbaar dat ik heb mogen promoveren en dat ik de kans en de tijd heb gekregen om dit project tot hier te brengen. Daarom wil ik iedereen bedanken. Laat ik bij het begin beginnen!

Emmy, we hebben dit samen allemaal meegemaakt, De Walstraat, Spanje, trouwen en nu Barbara. Ik ben je heel dankbaar dat je me de ruimte hebt gegeven. Op veel gebieden ben je meer wetenschapper dan ik. Vooral wanneer je je met zo veel enthousiasme en vanzelfsprekendheid in je droom en bewustzijn onderzoek stort. Je twijfelt dan vaak over de betekenis en het nut van nieuwe vindingen, maar dat zet jou juist aan om nog hardnekkiger te onderzoeken. Gea en Luud, jullie zijn er altijd in voor en tegenspoed. Met liefde, advies of gewoon in gedachten. Ook hebben jullie me eigenwijsheid, nieuwsgierigheid, creativiteit en reislustigheid gegeven. Edwin, jij bent er, ondanks je tegenspoed, voor anderen. In gedachten, door het sturen van gedichten of zelfs fysiek in het rumoerige Barcelona! Opa Jan, fysiek ben je er niet meer, maar van jou heb ik de neiging om altijd alle dingen uit elkaar te frutselen. Het spreekt voor zich dat dit in de wetenschap een positieve eigenschap is, waar ik nog dagelijks profijt van heb. Ook interesse in biologie, onderwijzen en (te) uitvoerig uitweiden over onderwerpen heb je indirect op me overgedragen. Oma Bakker, van jou leerde ik dat als je wilt je op geestkracht verder kan komen, ook als je ego in het 'nu' z'n spoor bijster is. Jeroen, je leerde me solderen en schakelingen maken, en je leerde me om niet bang te zijn om te proberen een groot en complex

apparaat te repareren. Van immuuncellen is waarschijnlijk naar verhouding evenveel bekend als wat jij en ik wisten van televisies toen we die repareerden. Toch lukte ons dat soms.

Maria, ik wil je heel erg bedanken voor alles wat je me hebt geleerd, en vooral voor al je geduld en de kans welke je me gegeven hebt om me in de fundamentele wetenschap te storten. Voor ons beiden geldt, de aanhouder wint! Ik denk dat de relatie tussen een aio en zijn begeleider in het algemeen een even grote uitdaging is als de research vraag in kwestie, we hebben allebei onze onvolkomenheden. Maar daar leren we van. Door de ervaringen die ik als aio binnen jouw lab en in Twente heb opgedaan, ben ik goed terecht gekomen in Nijmegen, waar ik biologen help hun vragen te beantwoorden met behulp van multiphoton microscopie en waar ik ook nog een stukje eigen onderzoek kan doen. Alessandra, co-promotor, in 2006 heb ik je de stuipen op het lijf gejaagd met vele optimalisaties van experimenten, maar uiteindelijk viel het kwartje: in de biologie ben je blij als de helft van je experimenten slaagt. Je zei ook: "Gert-Jan, er is light aan the eind van de tunnel, maar de tunnel is nog heel, heel, lang." Nu is plotseling het eind van de tunnel in zicht en ik ben dankbaar voor je adviezen en geduld. Ik denk dat het een mooi werk is geworden en ik hoop dat we ook het laatste hoofdstuk in een artikel kunnen smeden.

In Barcelona I should have learned two languages, Spanish and Catalan. Despite the frustrating combination of two languages and the noise in the comedora, I felt a warm welcome in the group of scientists and students of who most of them grew up in the neighborhood of Parc Cientific Barcelona. I won't forget the practical jokes, the walking to the comedora, grabar las palabras, people singing cumple años during the weekly colloquium, the Catalan coffee guy who gave a discount if you ordered in Catalan, futbol, the calcotada and the mountain trips... Thanks to Xavi, Miriam, Nacho, Michi, Isa, Joanjo, Ramona, Richi, Javier, Javi, Maruxa, David, Matteu, Santi, Marta, Johan, Errachid and all the others. After some time our lab was growing and soon we had our BioNanoPhotonics group. Together with the other foreigners, we were like a kind of a family, with long experiments and family and friends far away from Barcelona. Thomas, Ruth, un embrazo forte, espero todos esta bien con finalizar el thesis en Pais Basque. Thomas, ik hoop dat we binnenkort weer met een biertje erbij over LFA-1 kunnen nerden. Matthias, Rosa, Michael, Marta, Davide, Olga, Jesús, Sabina, Martin and Ruth, we had a good time, thanks! Also Pere, Isabel, thanks for helping me out during the first months in Barcelona. Lars, we had good rides in the mountains of Barcelona. I hope you are doing fine, if you are again in the vicinity of Elst don't hesitate to drop by. Juliane, the three of us had great walks in mountains. Greetings to Martin too!

Graag wil ik mijn paranimfen en vrienden Jan-Rutger en Paulus bedanken.

Jullie weten hoe het is om promovendus te zijn. Jan-Rutger, voor mij ben je een voorbeeld hoe je je door zo'n drukke periode hebt geslagen. Promoveren, kinderen, trouwen en rf-allergie en dan toch relax blijven. Ook vrienden en familie, Wim en Joke, Claartje, Rudy en Nieneke, Louise, Jos en Eva, Jan en Gerda, oma, Lennard, Rob, Joost, Jurgen, Moes, Henk en Els, Mark, Shira, Erik, Joop bedankt voor de aanmoedigingen en het geduld.

In Twente begon ik te promoveren en na Barcelona kwam ik in Nijmegen terug. Dit is een moeilijk stuk van het dankwoord om te schrijven, het is nog langer geleden dan de tijd in Barcelona. Ik hoop dat je me het vergeeft als ik je vergeten ben te noemen. Niek, bedankt dat je m'n promotor wilde zijn en bedankt voor de hulp bij de praktische zaken rond het promotie proces. Frans, bedankt voor alle hulp en het stoom afblazen tijdens de sportieve pauzes. Jeroen, bedankt voor het buiten-de-box denken, je hebt menig aio-hoofdbrekens opgelost. Martijn van Raaij, bedankt voor het gebruiken van je latex stylefiles, zie hier het strakke resultaat. Ook Karin, Nancy, Herman, Jacob, Gabriel, Robert, Erik, Marjolein en Sytse bedankt voor de goede werksfeer. Hans, Carl, Suzan, Agnieszka, Frank de Lange en Frank van Leeuwen, Ben en Joost, bedankt voor jullie meedenken over het onderzoek, via SMART en op bezoek. Speciaal wil ik Christina Eich bedanken voor het brainstormen over en uitvoeren van de shear flow experimenten welke in dit werk beschreven staan.

Also I would like to thank my current colleagues of the Cell Dynamics group, especially prof. Peter Friedl for his patience and understanding. And Bettina, seeing your great first in vivo tumor-CTL movie helped me through some dark days of tough writing.

Ook wil ik de medewerkers van stichting FOM bedanken. Ik voelde me door FOM altijd heel hartelijk gesteund. Door hen is de emigratie naar Barcelona goed verlopen. Harry Linders, bedankt voor je ondersteuning in de moeilijke periode toen ik net uit Barcelona terug kwam.

Rick van Rein, je hebt me enthousiast gemaakt om aio te worden. Bedankt voor het attenderen op deze interessante reis!

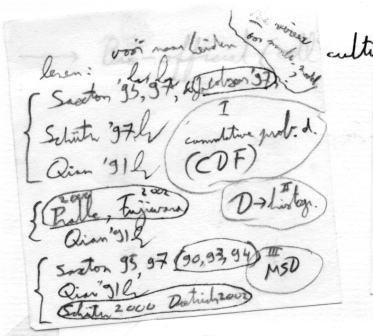

jgustavsson@pcb.ub.es

'tarden' = take time
'callado' = stil
cartera = wallet
disfruten = genieten

Cancer Cells are no friends. august 2006

Before you send them to hell, they should die slowly.
First you make them dizzy,
In the centrifuge.
Then, it is food, that you refuge.
Normally, they talk around.
But you should glue them, nail them to the ground.

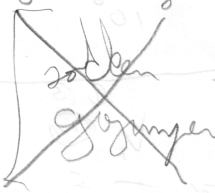

10 nov.

And when they think they're done,
Use ~~poison~~ slow poison, before they're gone

9 34487156

When they start to desintegrate,
That's when you start to refridgerate.
02994 5599
Is this hate?
Or just their fate?

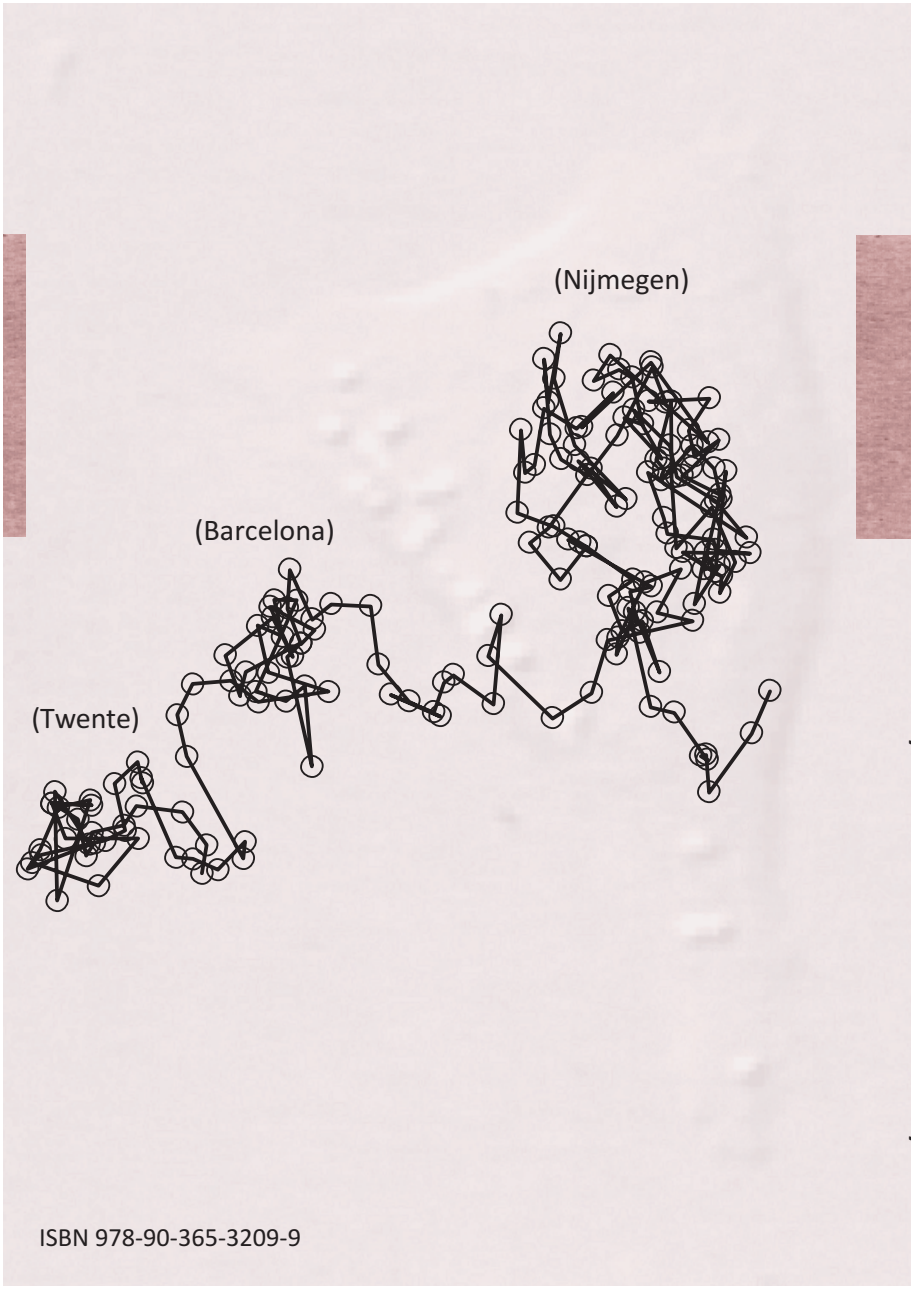

ISBN 978-90-365-3209-9